

Alexander Smirnov

AMB SYSTEM FOR HIGH-SPEED MOTORS USING AUTOMATIC COMMISSIONING

Thesis for the degree of Doctor of Science (Technology) to be presented with due permission for public examination and criticism in the Auditorium 1383 at Lappeenranta University of Technology, Lappeenranta, Finland, on the 18th of December, 2012, at 14:00.

Acta Universitatis
Lappeenrantaensis 508

Supervisor	Professor Olli Pyrhönen Department of Electrical Engineering LUT Institute of Energy Technology (LUT Energy) Faculty of Technology Lappeenranta University of Technology Finland
Reviewers	Professor Jerzy T. Sawicki Department of Mechanical Engineering Cleveland State University Cleveland, USA Professor Ilmar F. Santos Department of Mechanical Engineering Technical University of Denmark Lyngby, Denmark
Opponents	Professor Jerzy T. Sawicki Department of Mechanical Engineering Cleveland State University Cleveland, USA Professor Ilmar F. Santos Department of Mechanical Engineering Technical University of Denmark Lyngby, Denmark

ISBN 978-952-265-362-8
ISBN 978-952-265-363-5 (PDF)
ISSN 1456-4491

Lappeenrannan teknillinen yliopisto
Yliopistopaino 2012

Abstract

Alexander Smirnov

AMB system for high-speed motors using automatic commissioning

Acta Universitatis Lappeenrantaensis 508

Dissertation, Lappeenranta University of Technology
139 p.

Lappeenranta 2012

ISBN 978-952-265-362-8, ISBN 978-952-265-363-5 (PDF)

ISSN 1456-4491

The general trend towards increasing efficiency and energy density drives the industry to high-speed technologies. Active Magnetic Bearings (AMBs) are one of the technologies that allow contactless support of a rotating body. Theoretically, there are no limitations on the rotational speed. The absence of friction, low maintenance cost, micrometer precision, and programmable stiffness have made AMBs a viable choice for high-demanding applications. Along with the advances in power electronics, such as significantly improved reliability and cost, AMB systems have gained a wide adoption in the industry.

The AMB system is a complex, open-loop unstable system with multiple inputs and outputs. For normal operation, such a system requires a feedback control. To meet the high demands for performance and robustness, model-based control techniques should be applied. These techniques require an accurate plant model description and uncertainty estimations. The advanced control methods require more effort at the commissioning stage.

In this work, a methodology is developed for an automatic commissioning of a sub-critical, rigid gas blower machine. The commissioning process includes open-loop

tuning of separate parts such as sensors and actuators. The next step is to apply a system identification procedure to obtain a model for the controller synthesis. Finally, a robust model-based controller is synthesized and experimentally evaluated in the full operating range of the system.

The commissioning procedure is developed by applying only the system components available and a priori knowledge without any additional hardware. Thus, the work provides an intelligent system with a self-diagnostics feature and an automatic commissioning.

Keywords: active magnetic bearings, modeling, robust control, automatic commissioning, identification, gray-box identification, bumpless switch, linear parameter varying system

UDC 621.822:621.316.7:51.001.57

Acknowledgments

The research documented in this thesis was carried out at Lappeenranta University of Technology (LUT) during the years 2008–2012. The research work started as an individual study and continued later as a part of the SaLUT project funded by the Finnish Funding Agency for Technology and Innovation (TEKES). The partner in the research project was Saimaa University of Applied Sciences.

First of all, I would like to express my gratitude to my supervisors Professor Olli Pyrhönen, and Dr. Tuomo Lindh for the scientific guidance and an opportunity to be your student. Especially I wish to express my thanks to Dr. Rafal Jastrzebski for the countless discussions, valuable advice, and support in my scientific doubts. I would also like to thank Dr. Riku Pöllänen who acted as my supervisor at the beginning of the research.

I would express my thanks to Dr. Katja Hynynen for the valuable discussions and her cheerful mood when answering all my questions. I want to thank Professor Jussi Sopenen for his contribution and help with the laboratory setup. I wish to thank Pekko Jaatinen for many hours of frustration and excitement in the laboratory. I would like to thank all the coworkers at LUT for creating an inspiring and productive environment.

Special thanks are due to Dr. Hanna Niemelä for improving the language of my work by converting my messy wording into an intelligible story. I appreciate your contribution and support in the writing process.

I wish to thank the preliminary examiners of this doctoral thesis, Professor Jerzy T. Sawicki from Cleveland State University and Professor Ilmar F. Santos from the Technical University of Denmark for examining the manuscript and giving valuable comments. Your contribution has significantly improved the work.

It is impossible to name all the people who participated in the lengthy preparation of this work and left their mark on these pages. Dear friends, I am the happiest person to have so many of you. I want to express my gratitude for all the discussions at coffee breaks, for all the joy of traveling and spending evenings together, for all the countless minutes on the phone with those who are far away. Thus, my deepest thanks go to all

of you for your encouragement and belief in me.

My special thanks go to my parents for their love and support, and to my grandparents who saw and encouraged the best in me.

Last but not least, I express my deepest gratitude to my dearest Liudmila for you love and patience during the preparation of this work.

Lappeenranta, December 2nd, 2012

Alexander Smirnov

Contents

Abstract	3
Acknowledgments	5
Glossary	9
1 Introduction	15
1.1 Motivation and background	15
1.2 Objective and scope of the thesis	17
1.3 Active magnetic bearings	18
1.3.1 Operational principle	18
1.3.2 Commissioning	20
1.4 Outline of the thesis	22
1.5 Scientific contributions and publications	22
2 Active Magnetic Bearing System	25
2.1 Plant description	26
2.2 Actuator model	26
2.3 Power amplifier	30
2.4 Rotordynamics	32
2.4.1 Rigid rotor	34
2.4.2 Flexible rotor	35
2.4.3 Rotors of the test rig	37
2.5 Overall Plant Model	38
2.6 Axial Magnetic Bearings	42
2.7 Conclusions	43
3 Commissioning of Active Magnetic Bearings	45
3.1 Overview	45
3.2 Sensor tuning	46
3.3 Actuator tuning	55
3.3.1 Cable assignment as a factorial analysis problem	56
3.3.2 Cable assignment and misalignment	61
3.4 Conclusions	65
4 System Identification	67

4.1	Parametric identification of a linear model	68
4.1.1	Parametric frequency domain identification	69
4.2	Conclusions	78
5	Control of an AMB System	81
5.1	Model-based control approaches	82
5.1.1	Generalization of the control problem	83
5.1.2	Uncertainty description	83
5.1.3	Inclusion of an uncertainty set	85
5.1.4	Weighting inputs and outputs	86
5.1.5	Weight selection	90
5.2	Bumpless switching	91
5.3	LPV control	93
5.3.1	LPV model of the AMB system	96
5.3.2	LPV controller implementation	96
5.4	Controller synthesis	97
5.4.1	AMB system from a control point of view	97
5.4.2	Synthesis procedure	99
5.4.3	Controller evaluation	100
5.5	Conclusions	108
6	Conclusions	111
6.1	Summary	111
6.2	Suggestions for future work	113
	References	115
	Appendices	121
	A Geometric center	123
	B Factorial design experiments	125
	C Identification	129
	D Details of the prototype platform	133
	D.1 Magnetic bearing dimensions	133
	D.2 Parameters of the rotor	135
	D.3 Sensors and control electronics	136
	E Control system models	137

List of Symbols and Abbreviations

Acronyms

AMB	Active Magnetic Bearing
DC	direct current
DFT	discrete Fourier transformation
DOF	degree-of-freedom
DSP	digital signal processor
EMA	experimental modal analysis
FEM	finite element method
FPGA	field programmable gate array
FRF	frequency response function
IGBT	insulated gate bipolar transistor
LFT	Linear Fractional Transformation
LMI	linear matrix inequality
LPV	linear parameter varying
LQG	linear quadratic Gaussian
LQR	linear quadratic regulator
LSE	least square estimator
LTI	linear time invariant
MIMO	multi-input multi-output

MLE	maximum likelihood estimator
PID	proportional integral derivative
PMSM	permanent magnet synchronous machine
PWM	pulse width modulation
RHP	right-half plane
SISO	single-input single-output

Greek letters

β_x	Rotor angle around x axis
β_y	Rotor angle around y axis
χ	Force acting angle of an electromagnet
δ	Normalized structured uncertainty
γ_{cn}	Condition number a linear system
Ω	Rotational speed
Φ^m	Reduced mode shape function matrix in modal coordinates
Φ	Magnetic flux
Φ_{io}	Matrix of relations between inputs and outputs in the factorial analysis
σ	Singular value of a linear system
θ	Vector of unknown parameters in the identification routine

Roman letters

A	State matrix in state-space representation
A_{air}	Cross section of the air
A_{Fe}	Cross section of the iron
B	Flux density
\mathbf{B}_{Eu}	Euclidean ball

B	Input matrix in state-space representation
C	Output matrix in state-space representation
c	Eddy current coefficient for the magnetic path approximation
D	Feedthrough matrix in state-space representation
D_{fl}	Electric displacement field
D_{M}	Damping matrix of the mechanical model
D^{m}	Modal damping matrix
F	Force vector
G	Transfer function of the linear plant model
G_{M}	Gyroscopic matrix of the mechanical model
g_0	Nominal air gap between a rotor and a pole of an electromagnet
g_{a}	Air gap between a rotor and an auxiliary bearing
G^{m}	Modal gyroscopic matrix
H_{air}	Magnetic field strength in air
H_{Fe}	Magnetic field strength in iron
H_{n}	Vector of inputs in the fractional analysis
I	Identity matrix
i_{b}	Bias current
i_{c}	Control current
i_{m}	Measured current
I_{p}	Polar moment of inertia
i_{ref}	Reference current
I_{x}	Transversal moment of inertia about x axis
I_{y}	Transversal moment of inertia about y axis
I_{z}	Rotational moment of inertia about z axis ($I_{\text{z}} = I_{\text{p}}$)

\mathbf{K}	Stiffness matrix
\mathbf{K}_{fb}	Feedback controller
\mathbf{K}_{ff}	Feed-forward controller
k_i	Current stiffness
\mathbf{K}_k	Vector of the controller state multipliers
\mathbf{K}^m	Modal stiffness matrix
\mathbf{K}_s	Controller for the shaped plant in the Glover–McFarlane control problem
k_u	Velocity induced voltage coefficient
k_x	Position stiffness
l_{air}	Length of the air gap
\mathbf{M}	Mass matrix
\mathbf{M}^m	Modal mass matrix
\mathbf{N}	Shape function matrix
N	Number of coil turns
\mathbf{O}	Transfer function of the observer
\mathbf{P}	Transfer function of the generalized plant model for the controller synthesis problem
\mathbf{P}_{Eu}	Polyhedron
π	ratio of the circumference of a circle to the diameter
\mathbf{q}	Generalized displacement vector in the mechanical model
\mathcal{R}_{ax}	Resistance of the axial coil
\mathbf{r}	Reference signal for the control system
R^0	The static reluctance coefficient
s	Laplace variable

\mathbf{S}_a	Nodal location matrix of the actuator in the mechanical model
Σ	Matrix of singular values from the singular value factorization
\mathbf{S}_s	Nodal location matrix of the sensor in the mechanical model
Θ	Vector of unknown parameters in the fractional analysis
\mathbf{T}_{ref}	Reference transfer function that describes the desired dynamics of the closed-loop plant
\mathbf{u}	Control signals provided by the control system
U_{DC}	Voltage of the direct current link
\mathbf{V}_n	Vector of noise in the fractional analysis
\mathbf{w}	Vector of the exogenous inputs for the generalized plant model
w_{bw}	Bandwidth of an actuator
W_{ce}	Magnetic coenergy
W_e	Magnetic energy
\mathbf{x}	State vector of the linear plant model
\mathbf{x}_c	Vector of coordinates for the inscribed circle center
\mathbf{y}	Vector of measured signals from the plant
\mathbf{z}	Vector of the exogenous outputs for the generalized plant model
$\mathbf{0}$	Zero matrix
\mathbf{Z}_n	Vector of outputs in the fractional analysis

Subscripts

A	A-end of the system with bearing A
a	Actuator part of the linear plant model
B	B-end of the system with bearing B

r	Rotor part of the linear plant model
s, A	Sensor at the A-end of the system with bearing A
s, B	Sensor at the B-end of the system with bearing B

Superscripts

$\hat{}$	Estimated value
m	Modal coordinate system in the mechanical model

Chapter 1

Introduction

The chapter provides basic background for the technology addressed in this doctoral thesis. The benefits and drawbacks of the technology are outlined. The motivation for the work is presented and previous progress on the topic is reviewed. Finally, the outline of the work is given and the main scientific contributions are identified.

1.1 Motivation and background

The overall trend towards increasing power demands as stated by the report of British Petroleum (2012) poses great challenges for engineers. The solution is not only in increasing the production of energy but, naturally, in better efficiency. On one side, efficient consumption imposes restrictions, while on the other side, boundaries are set by efficient production. To push the latter boundaries further, it is required to apply high-speed technologies.

Along with benefits new challenges emerge. With high-speed technology in rotating machinery the wear of components and increased maintenance become a major problem. The weakest part from that point is conventional ball bearings. Such bearings cannot withstand the load at high rotational speeds. Thus, there are several alternatives such as fluid film bearings, air foil bearings, and magnetic bearings.

Fluid film bearings support the shaft on a thin layer of liquid. The liquid is pressurized either by a pump or by the shaft itself. That way, the problem with the wear of

components is solved. However, the maintenance problem remains unsolved as the oil that is usually used as a liquid has to be replaced on a regular basis. In addition, an oil leakage may cause contamination of the surrounding environment, which is also a significant limitation on many applications.

Air foil bearings are based on the same principles as fluid film bearings, but instead of liquid, some gas is used. Bearings of this kind are considered 'clean' bearings as there is no contamination. The problem with maintenance is alleviated, yet significant wear of components still takes place during the start-up. Bearings of this type work only at high speeds. The other limitation is their relatively low capacity.

Another approach is magnetic bearings that use magnetic force to levitate the rotor. In particular, one type of magnetic bearings, AMBs, has got a wide spread over the last decades. The term 'active' means that the magnetic field is produced and constantly changed according to a specific law, which is required to overcome Earnshaw's theorem.

AMBs allow to overcome the above-mentioned limitations. The capacity characteristic is good enough to be implemented in large turbomachinery. As the rotor is levitated without any friction, the wear of components is almost absent, and the speed is limited by the strength of the materials. No lubrication is needed and the system can operate in a vacuum or a hazardous environment. The stiffness value can be adapted according to the specific operating point. The constantly growing list of AMBs applications includes:

- Generators and compressors of a megawatt range; typically, natural gas compressor stations and turbines for power generation.
- Machine tools and drilling applications, where high precision with a high rotational speed is required.
- Artificial heart pumps where any risk of contamination must be eliminated.
- Energy storages, such as flywheels, with high requirements for efficiency.

Along with the above-mentioned advantages, AMBs have certain drawbacks. For the industry, the main one is the high initial investment cost. From the design point of view, AMBs require relatively more additional space. The capacity per surface area is smaller compared with fluid film bearings. What is more, additional space is needed for the backup bearings. Finally, the failure of a single component causes the failure of the whole system.

An AMB rotor system is a complex technology that requires a control law to operate. The control law itself requires a good approximation of the model to work sufficiently well. The stricter the requirements for the system are, the more complex control approach is used. The more complex the approach is, the more accurate model is needed. With modern robust techniques, in addition to the model itself, the uncertainty

should be estimated. This kind of a problem is solved with modeling techniques in the initial stage.

The rotor dynamics is modeled with the finite element method (FEM). It provides accurate results for the rigid modes and estimates for the flexible ones. These results are verified and updated by an experimental modal analysis (EMA). After the assembly, the system identification techniques help to tune the parameters of the system.

Actually, the identification, tuning, and diagnostics of the system are possible with the system itself. The feedback control requires the position of the rotor as a measured signal. To keep the rotor in the desired position, there is a set of actuators that provide forces. In addition, there is a computational unit that calculates the control signals. Thus, the system can tune itself in an intelligent way.

An intelligent operation of the system helps to alleviate many problems and is a subject of further, extended research.

1.2 Objective and scope of the thesis

In this thesis, an AMB system is considered as a mechatronics object with a sophisticated structure. The system includes actuators, sensors, and a powerful computation unit. A combination of knowledge from multiple disciplines is required to maintain the system. This tends to be a problem as the systems of this kind are more complex at the commissioning stage. To find and accurately diagnose a problem, skilled personnel is required. The problem becomes more significant at the commissioning stage when the system is installed far from the production point, and the selection of available tools is limited.

The natural complexity of the system can be beneficial if intelligence is added to the components. The combination of sensors and actuators with processing power allows self-diagnostics. Thus, in this work, the target is to develop a set of procedures to reduce the time and facilitate the process of commissioning the system in the field.

The idea of automation in the design and commissioning of an AMB system has matured with the technology and increasing adoption in the industry (Swann, 2009). As a first step, the problem of modeling and building a controller was solved (Lösch, 2002). The author proposed an iterative method for the identification and controller design, thus avoiding the deadlock when the identification routines need a levitated system and the controller needs a good model. The topic was investigated by Sawicki and Maslen (2008), who discussed the further options of automatic controller tuning. As AMBs are widely adopted in the industry, discussions about the full commissioning procedure arose (Walter et al., 2010). In the publication, the authors provide steps to be applied during the commissioning and discuss the required hardware and skills of the personnel.

As the idea is to add intelligence to the system, the methods are limited only to the system itself. The developed procedures should only deal with the inputs and outputs provided by an AMB. Thus, an effort was directed towards techniques that do not require any external tools and use only the elements available. To provide the results, the developed methodology relies on a priori knowledge. The information is available from the manufacturer and obtained during the manufacturing process, and thus, it is not a limiting factor. This way, detailed knowledge of the system properties and intelligent use of available components allow to significantly reduce the effort required for the commissioning.

Practical limitations set in the doctoral thesis:

- methods are verified with the system available in the laboratory
- rotor is considered to be subcritical
- radial bearings are heteropolar bearings with four electromagnets each
- axial bearings are presented by two electromagnets
- each electromagnet is powered by a separate power amplifier

1.3 Active magnetic bearings

1.3.1 Operational principle

Active magnetic bearings are based on the force provided by the magnetic field on a ferromagnetic body. To provide the force, current-controlled electromagnets are used. One such an electromagnet provides only attractive force. To provide force in both directions, a pair of electromagnets is applied.

A ferromagnetic body placed between two electromagnets is not stable and tends to deviate to one or another side. To keep the body in the center position, a special control law is applied. It provides signals, reducing the current in one electromagnet and increasing the current in the other, thereby overcoming the displacement from the center point. To estimate the current position of the body, a sensor is used in the corresponding direction. The scheme in Fig. 1.1 describes the above mentioned principles.

In Fig. 1.1, an AMB system for the radial bearing is demonstrated. The description and signal paths are given for the x plane. The signals for other directions are propagating in a similar way. The control current (i_c) provided by the controller for a specific direction is biased with a bias current (i_b) to linearize the force–current relation. After

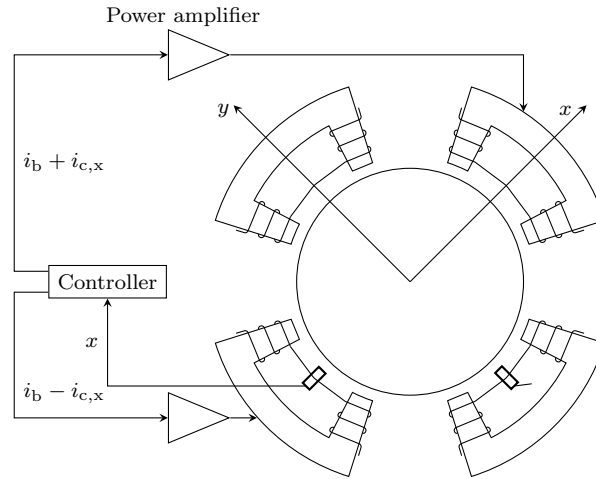


Figure 1.1. Operating principle of an AMB system. The measured displacement of the rotor x is provided to the controller. The controller, based on previous measurements, calculates the control current i_c . The current is biased with i_b and provided for the power amplifiers that feed the electromagnets.

that, the final current signal is supplied to the power amplifier, and then, to the coil of an electromagnet.

A typical AMB supported rotor is demonstrated in Fig. 1.2. There are two radial bearings at the opposite ends of the rotor. There is one axial bearing in an arbitrarily chosen position along the rotor. With the most common four-electromagnet arrangement of radial bearings and two electromagnets for the axial bearing, the system results in ten electromagnets and five position sensors (Schweitzer and Maslen, 2009). In addition to magnetic bearings, the safety bearings are installed. They should protect the system at emergency stops when power is lost and also hold the rotor after a drop down.

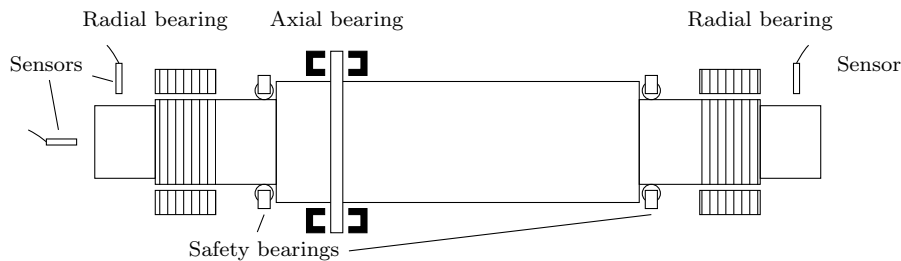


Figure 1.2. Arrangement of an AMB rotor system. A typical system includes two radial bearings and an axial one with sensors in the necessary directions. The system is completed with safety bearings that provide protection in emergency cases.

1.3.2 Commissioning

The research in the field of commissioning is stimulated by the increased adoption of AMBs in industry (Swann, 2009). As it was demonstrated above, an AMB system is a complicated one with different components. The system itself is a sophisticated product resulting from the multidisciplinary fusion of several sciences, including for instance rotor dynamics, electrical engineering, and control theory.

The effort in commissioning was concentrated on the specific problems typical of high-speed systems. Among these, a key problem is an unbalanced response that appears as a disturbance synchronous to the rotor speed. The AMB system provides a unique opportunity to overcome this problem in different ways as it is demonstrated by Jastrzebski (2007). The problem becomes more complicated when an access to the system is limited and requires accurate validation of the unbalance response (Maslen et al., 2012). The next step is automation of the unbalance rejection procedure, which is claimed to be possible without previous balancing carried out by the manufacturer. According to work (Kodochigov et al., 2012)

Based on preliminary results, it is possible to balance the flexible vertical rotor . . . without balancing the rotor in factory conditions.

The other element of the commissioning process is fault detection. The fault detection not only helps to find the problems but also to prevent them based on the continuous estimation of the system state. With the model-based approach, different components of the system are monitored and validated (Beckerle et al., 2012a,b). The fault detection techniques help to analyze and detect problems such as the rotor crack Sawicki et al. (2011).

The procedure of tuning a controller is also an important part of the commissioning process. In Jeon et al. (2002), the authors tune the controller with the results of the identification procedure. Other authors use neural networks with on-line training to achieve performance specifications (Chen and Lin, 2012). Another option is to apply a genetic algorithm to tune the controller Jastrzebski et al. (2010). A general outline for the automatic controller tuning is given by the above-mentioned authors (Sawicki and Maslen, 2008).

The general process of commissioning an AMB system is presented in Fig. 1.3. This description includes the necessary steps to run the system at the nominal speed. The described steps can be carried out by the system itself without external tools. Usually, the list is extended by the steps that can be performed only with additional tools (Walter et al., 2010). Such procedures, however, are out of the scope of this work.

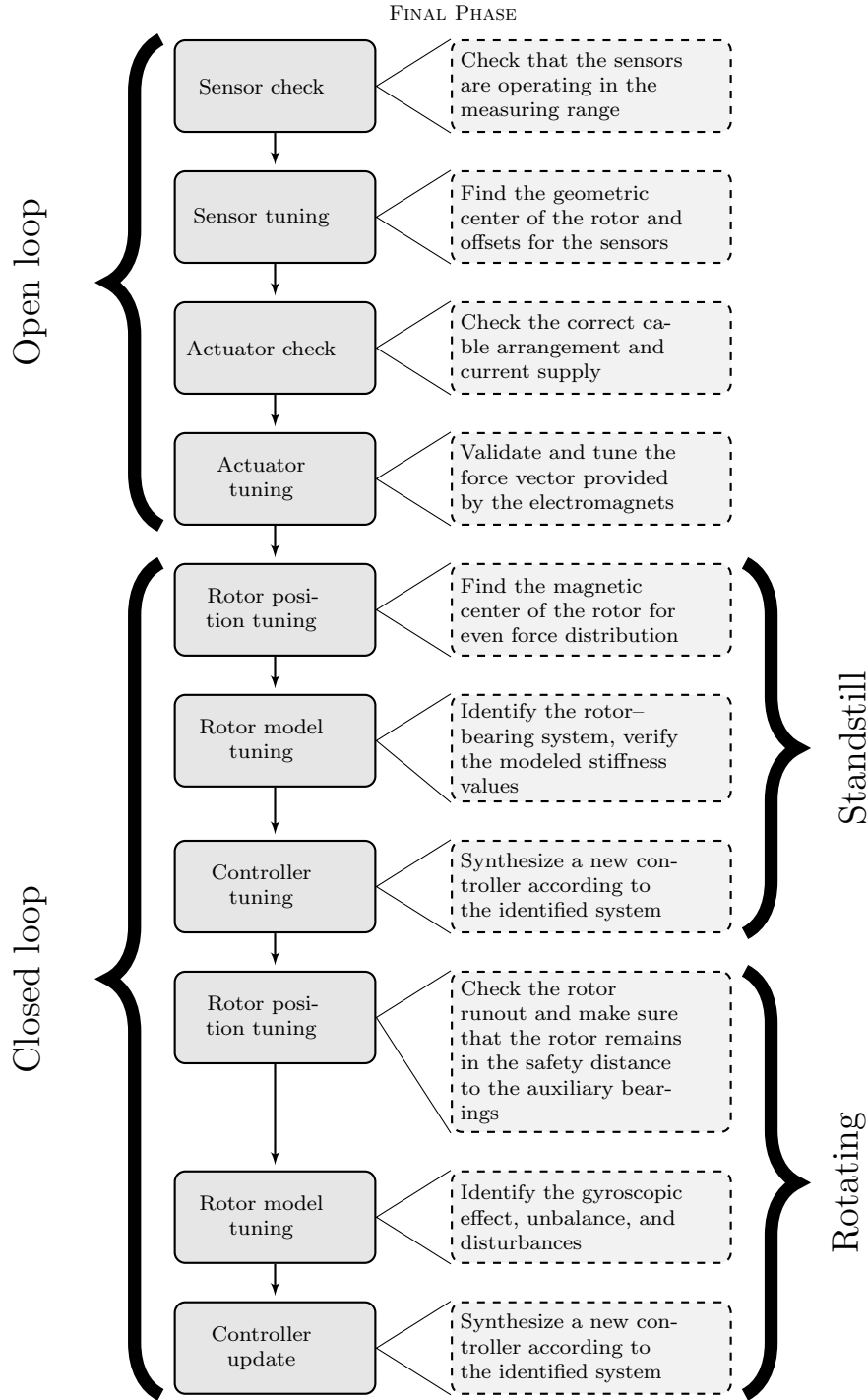


Figure 1.3. Commissioning diagram. The diagram describes the steps and parts of an AMB rotor system that are verified during the commissioning procedure. Only steps that can be carried out without external hardware are included.

1.4 Outline of the thesis

The thesis is presented in six chapters following the commissioning steps of the system, starting from the modeling of the system and finalizing by the controller synthesis for a wide operating range. The obtained experimental results are not collected separately but provided in the appropriate chapters after the theoretical background. This provides a direct link between the suggested methods and the results of their implementation. The work is organized as follows:

Chapter 1 provides the general background and motivation for the work. The main targets are outlined and the objectives of the thesis are presented.

Chapter 2 the process of modeling an AMB system is presented. Based on the physical laws, each component is discussed. The description is narrowed with the idea of specifying the system available in the laboratory. Thus, the discussion is mostly limited to the specific design solutions with a brief mention of other alternatives.

Chapter 3 states the general problem of commissioning and divides it into individual steps. The necessary steps are presented in the form of a general list. In the chapter, the discussion is devoted to the solution of initial problems. These include sensor and actuator tuning. The process is presented in a mathematical framework, and a solution is obtained.

Chapter 4 covers the final specification of the system parameters. It is done by identification techniques. The applicability of such techniques is discussed, and a set of parameters required for identification are chosen. The discussion based on the experimental results demonstrates the difference between a modeled system and an identified one. As a result, a model suitable for the controller synthesis is obtained.

Chapter 5 presents the theoretical background on the modern control approaches. The AMB system is also presented in the form of a linear parameter varying (LPV) system. Techniques that allow switching between controllers are discussed. The AMB system is discussed from a control point of view with its limitations and constraints. Design objectives and their formulation in a loop-shaping approach are discussed. Finally, the obtained controllers are evaluated and theoretical results compared with the experimental ones.

Chapter 6 concludes the obtained results, summarizes the work, and provides suggestions for the future research.

1.5 Scientific contributions and publications

The doctoral thesis provides the following scientific contributions:

- Commissioning steps are presented in the form of mathematical optimization problems that can be solved by modern computational tools.
- The commissioning process for a subcritical rotor with a known bearing structure is formulated.
- Automatic commissioning procedure of the AMB system without additional sensors and external hardware is introduced and described.
- The AMB system with respect to the rotational speed as an uncertainty is analyzed. Based on the experimental results, the expression of uncertainty in the parametric form is shown to be conservative compared with the coprime form.
- Robust and linear-parameter-varying controllers are synthesized, implemented, and experimentally evaluated for the subcritical system based on the identification procedure.

The results described in the work were presented in part in the following conference papers:

1. Smirnov, A. and Jastrzebski, R.P. (2009), “Differential evolution approach for tuning an \mathcal{H}_∞ controller in AMB systems,” in *Proceedings of the 35th Annual Conference of IEEE Industrial Electronics (IECON 2009)*, Porto, Portugal, pp. 350–360.
2. Smirnov, A., Tolsa, K., and Jastrzebski, R.P. (2010), “Implementation of a bumpless switch in axial magnetic bearings,” in *Proceedings of International Symposium on Industrial Embedded Systems (SIES 2010)*, Trento, Italy, pp. 63–68.
3. Smirnov, A., Jastrzebski, R.P., and Hynynen, K.M. (2010), “Gain-Scheduled and Linear Parameter-Varying Approaches in Control of Active Magnetic Bearings,” in *Proceedings of the Twelfth International Symposium on Magnetic Bearings (ISMB12)*, Wuhan, China, pp. 350–360.

In the first work, the first author implemented a genetic algorithm that tunes the controller according to the performance specifications and verified the obtained controllers.

In the second paper, the implementation of a bumpless switch algorithm with a digital signal processor (DSP) and a real-time system was provided. The first author is also responsible for producing all the experimental results.

In the last work, an LPV algorithm was applied to an AMB system and the theoretical possibility of controlling the system were investigated. The first author also produced all the simulation results presented in the paper.

The other results related to the topic of the thesis, including a background analysis and alternative methodologies are presented in the following papers:

1. Jastrzebski, R.P., Hynynen, K.M., and Smirnov, A. (2009), “Case study comparison of linear \mathcal{H}_∞ loop-shaping design and signal-based \mathcal{H}_∞ control,” in *Proceedings of the XXII International Symposium on Information, Communication and Automation Technologies (ICAT 2009)*, Sarajevo, Bosnia Herzegovina, pp. 1–8.
2. Hynynen, K.M., Jastrzebski, R.P., and Smirnov, A. (2010), “Experimental Analysis of Frequency Response Function Estimation Methods for Active Magnetic Bearing Rotor System,” in *Proceedings of the Twelfth International Symposium on Magnetic Bearings (ISMB12)*, Wuhan, China, pp. 40–46.
3. Jastrzebski, R.P., Hynynen, K.M., and Smirnov, A. (2010), “Uncertainty Set, Design and Performance Evaluation of Centralized Controllers for AMB System,” in *Proceedings of the Twelfth International Symposium on Magnetic Bearings (ISMB12)*, Wuhan, China, pp. 47–57.
4. Jastrzebski, R.P., Hynynen, K.M., and Smirnov, A. (2010), “H-infinity control of active magnetic suspension,” *Mechanical Systems and Signal Processing*, vol. 24, no 4, pp.995–1006.
5. Jastrzebski, R.P., Smirnov, A., Pyrhonen, O., and Pilat, A. (2011), “Discussion on Robust Control Applied to Active Magnetic Bearings Rotor System,” in *Robust Control / Book 3*, InTech - Open Access Publisher.
6. Jastrzebski, R.P., Hynynen, K.M., Smirnov, A., and Pyrhonen, O. (2012). “Influence of the drive and dc link generated disturbances on an AMB control system,” *Electrical Review*, vol 1, no a, pp.247–253.
7. Jastrzebski, R.P., Smirnov, A., Lin, Z., Allaire, P., and Pyrhonen, O. (2012), “Extended Kalman Filter Applied to an AMB System with Strong Magnetic Saturation,” in *Proceedings of the Thirteenth International Symposium on Magnetic Bearings (ISMB13)*, Washington DC, USA.

Chapter 2

Active Magnetic Bearing System

As a well-defined linear model is required for the controller synthesis, in this chapter, the system is divided into different components. Each component is examined, and an appropriate model is chosen. The main objective is to find a linear representation of the system that accurately describes the target setup available in the laboratory. Thus, the discussion is narrowed to particular design solutions of the prototype. The models are based on physical laws and linearized around the operating point.

AMBs represent a complex system. For successful operation, knowledge of different disciplines is required, the most important of these being mechanical, electrical, computer, and control engineering. The main function of an AMB is to support a rotating rotor. Thus, to describe the behavior of the moving rotor, knowledge and tools of mechanical engineering are required. The rotor is supported by an electromagnetic field. To describe this part of the system, electrical engineering is a requisite. Electrical engineering also plays a key role in sensor technology, as contactless sensors are mostly based on electromagnetic physical effects. As it was stated in the introduction, an active system is operated by electromagnets, which can provide only attractive force. According to Earnshaw's theorem, such a system cannot reach a stable equilibrium. Consequently, the stability problem is solved by control engineering. In the modern world, it is difficult to imagine any advanced system without the use of a computer. All the above-mentioned fields apply computer engineering to improve, simulate, and test their solutions. Therefore, this discipline is ubiquitous nowadays.

Complex interdisciplinary systems of this kind are called mechatronics systems. The interaction of the different fields is illustrated in Fig. 2.1.

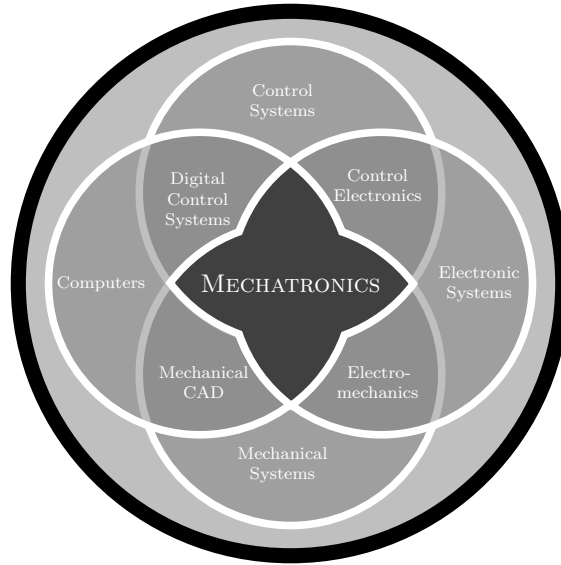


Figure 2.1. Mechatronics and its relations to different disciplines. Combination of electronic, mechanical, and control systems with an addition of computer modeling resulting in a multidisciplinary field of engineering – mechatronics.

2.1 Plant description

To provide an accurate model of the plant, it is necessary to describe each component. These components include the rotor, the actuator, and sensors. Each of them introduces specific dynamics into the system. The dynamics, depending on its effects on the control system, can be neglected or included in the linear model. From the control point of view, a valid linear model is the key target as it is used to synthesize the controllers. The basic requirement for a linear model is that it should be as simple as possible yet including the main features.

2.2 Actuator model

An actuator is the most crucial part that allows to achieve levitation. The magnetic actuator is best presented as a U-shaped electromagnet, Fig. 2.3. According to Maxwell's equation

$$\nabla \times \mathbf{H} = \mathbf{J} + \frac{\partial \mathbf{D}_{fl}}{\partial t}, \quad (2.1)$$

the currents and the changing electric fields produce the magnetic fields. In Eq. (2.1), the magnetic field strength is denoted by \mathbf{H} , \mathbf{J} is the current density, and \mathbf{D}_{fl} is the electric displacement field. Thus, according to Ampère's law, the current i in the coil

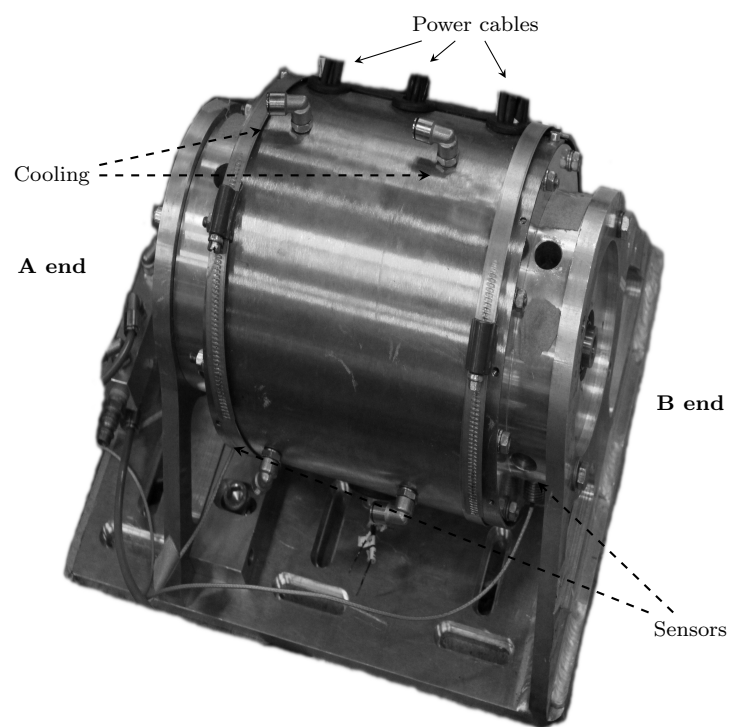


Figure 2.2. Photo of the prototype. In this illustration, an outer frame of the 3.5 kW gas blower machine is demonstrated. The inputs and outputs are indicated together with the definition of the rotor ends.

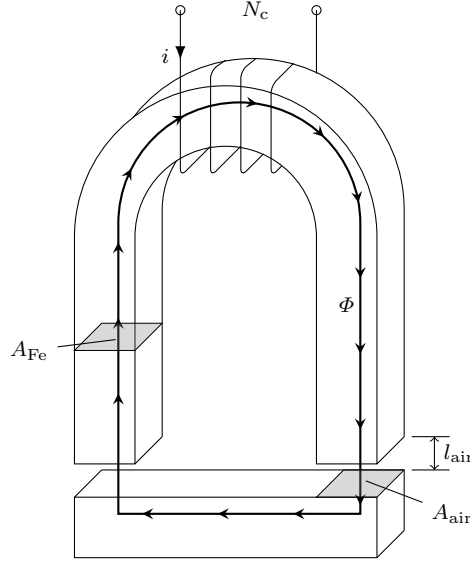


Figure 2.3. Magnetic circuit of an electromagnet. The figure demonstrates the typical distribution and path of the magnetic flux (Φ) in a horseshoe electromagnet. The flux is induced by the current (i) supplied to the winding with a specific number of turns (N). The distribution depends on the iron cross-section (A_{Fe}), the air gap cross-section (A_{air}), and the air gap length (l_{air}).

generates a magnetic field H

$$\oint H dl = Ni, \quad (2.2)$$

where N is the number of coil turns and l is the length of the magnetic path. There are two types of materials for the flux path, iron and air. Assuming that there is no flux leakage and the cross sections of iron (A_{Fe}) and air (A_{air}) are equal, the flux Φ is constant and the flux density B is equal for both media, Eq. (2.2) can be presented in the form

$$l_{Fe}H_{Fe} + 2l_{air}H_{air} = Ni, \quad (2.3)$$

where l_{Fe} , l_{air} are the magnetic paths in the iron and in the air, and H_{Fe} and H_{air} are the magnetic field strengths in the iron and in the air, respectively. Expressing the magnetic field strength by the flux density, the following equation is obtained

$$l_{Fe} \frac{B}{\mu_0 \mu_{Fe}} + 2l_{air} \frac{B}{\mu_0} = Ni. \quad (2.4)$$

As the relative permeability μ_{Fe} of iron is significantly greater than one, $\mu_{Fe} \gg 1$, the first term in Eq. (2.4) can be neglected. Under this assumption, the flux density in the air gap is

$$B = \mu_0 \frac{Ni}{2l_{air}}. \quad (2.5)$$

The magnetic energy W_e stored in the air gap is equal to the coenergy W_{ce} under an assumption of a linear magnetic circuit. As it was assumed above that there is no leakage, the field can be considered homogeneous and thus, the coenergy is expressed as

$$W_{ce} = \int_V \int_0^H \mathbf{B} d\mathbf{H} dV = \frac{1}{2\mu_0} \int_V B^2 dV = \frac{1}{2\mu_0} B^2 A_{\text{air}} l_{\text{air}}, \quad (2.6)$$

where V is the volume where the energy is stored; in the case of an air gap, it is defined as $V = 2A_{\text{air}}l_{\text{air}}$. The length of the air gap is denoted l_{air} . The magnetic force is a partial derivative of energy with respect to the air gap

$$f = \frac{\partial W_{ce}}{\partial l_{\text{air}}} = \frac{B^2 A_{\text{air}} \cos \chi}{\mu_0}, \quad (2.7)$$

where χ is the angle of force direction, which is equal to half of the angle between the poles of the electromagnet. By substituting the flux density from Eq. (2.5), the force is written as

$$f = \frac{\mu_0 N^2 i^2 A_{\text{air}} \cos \chi}{4l_{\text{air}}^2}. \quad (2.8)$$

One electromagnet provides only attractive force, and thus, a pair of them is required to move the body along one axis (the subscripts x and y denote the desired axis) in both directions. The resulting force of similar electromagnets placed opposite to each other is expressed as

$$f_x = f_{x,1} - f_{x,2} = \frac{\mu_0 N^2 A_{\text{air}} \cos \chi}{4} \left(\frac{i_{x,1}^2}{(g_0 - x)^2} - \frac{i_{x,2}^2}{(g_0 + x)^2} \right), \quad (2.9)$$

where g_0 is the nominal air gap between a rotor and a pole.

The force written in Eq. (2.9) is nonlinear with respect to the movement of the rotor x and the supplied current i_x . To linearize the system, it is assumed that the motion takes place around the operating point with small deviations from it, and thus, $x \sim 0$. To linearize the system with respect to current, a bias current is applied. The bias current i_b is usually chosen to be not more than half of the maximum coil current $i_b \leq 0.5i_{\text{max}}$. The currents applied to the pair of electromagnets are thus calculated as

$$i_1 = \begin{cases} i_{\text{bias}} + i_c & \text{if } i_c \geq -i_{\text{bias}}, \\ 0 & \text{if } i_c < -i_{\text{bias}}, \end{cases} \quad (2.10)$$

$$i_2 = \begin{cases} i_{\text{bias}} - i_c & \text{if } i_c \leq i_{\text{bias}}, \\ 0 & \text{if } i_c > i_{\text{bias}}. \end{cases} \quad (2.11)$$

The final linearized equation for coupled electromagnets has the form

$$f_x = k_i i_{x,c} + k_x x, \quad (2.12)$$

where k_i and k_x are the current and position stiffnesses in the region of the operating point

$$k_i = \left. \frac{\partial f}{\partial i_c} \right|_{x=0, i_c=0} = \frac{\mu_0 N^2 i_{\text{bias}} A_{\text{air}} \cos \chi}{g_0^2}, \quad (2.13)$$

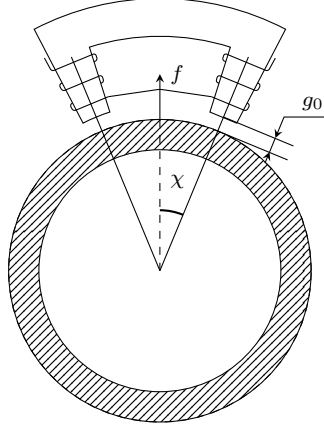


Figure 2.4. Force acting on the rotor from one electromagnet. The figure demonstrates the arrangement of an electromagnet and a rotor with a lamination for radial bearings. The force vector (f) is defined based on the angle (χ) between the poles of the electromagnet.

$$k_x = \left. \frac{\partial f}{\partial x} \right|_{x=0, i_c=0} = \frac{\mu_0 N^2 i_{\text{bias}}^2 A_{\text{air}} \cos \chi}{g_0^3}. \quad (2.14)$$

The obtained model Eq. (2.12) keeps its linearity in a relatively large region and suffices for most of applications, as demonstrated by Schweitzer and Maslen (2009). In the case of extreme conditions and specific applications, the model is not accurate enough. The main limitation is the flux saturation, which limits the maximum force. In addition, the flux leakage and eddy currents affect the dynamics of the system. (Sun and Yu, 2002; Schweitzer and Maslen, 2009)

2.3 Power amplifier

The electromagnet must be supplied with current. The current may be only positive or negative as both produce an attractive force, as can be seen from Eq. (2.8). The main requirement is a fast slew rate in order to be able to follow the rotor movement with the control signal. As a result of the recent progress in the semiconductor and power electronics industries, the switched power amplifier is a robust and reliable solution.

In this work, a semi-passive H-bridge as a switching amplifier is used. The implementation of other amplifiers is possible, but the scheme provides bipolar coil excitation and only unipolar current (Schweitzer and Maslen, 2009). The direction of the current does not change the force vector, and thus, only one direction suffices. The ability to increase or decrease the current fast is essential for the control. Hence, the bridge satisfies all the requirements with the simple schematics.

The schematic of the H-bridge power amplifier circuit is presented in Fig. 2.5. The

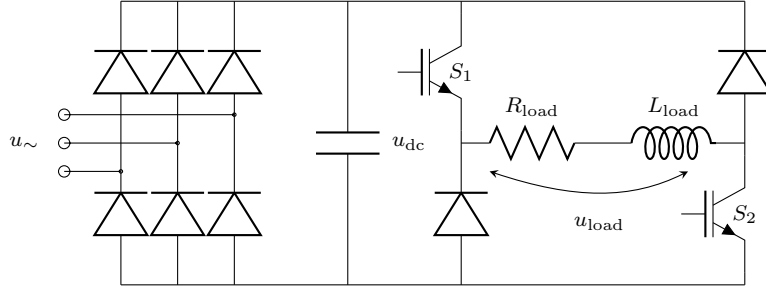


Figure 2.5. Switching power amplifier circuit. The circuit rectifies the three-phase voltage. Switches S_1 and S_2 allow to apply positive, negative, or zero voltage to the load. As the current direction does not have an impact on providing the magnetic force, the scheme is simplified to allow current flow in one direction only.

supplied AC voltage is rectified by a diode bridge and smoothed by a capacitor. Based on the reference i_{ref} and the actual current i_{m} , the switches S_1 and S_2 are opened or closed providing positive, negative, or zero voltage across the load. In the case of an AMB system, the load is a coil of an electromagnet, which can be approximated by an inductance L_{load} and a resistance R_{load} .

As it was mentioned above, the switching scheme requires an inner control loop to stabilize the output current. A simple proportional integral derivative (PID) type controller can achieve the desired performance. A schematic of the current supply is presented in Fig. 2.6. The current is measured in the coil by an external current sensor. The control scheme based on the reference current and the implemented controller calculates the control signal. The control signal with a pulse width modulation (PWM) scheme opens or closes the switches in the power circuit.

A custom electronics in the prototype is implemented with insulated gate bipolar transistors (IGBTs) to achieve up to 10 A current with 120 V. For two radial bearings with four electromagnets, a total of eight power amplifiers are required. Additional

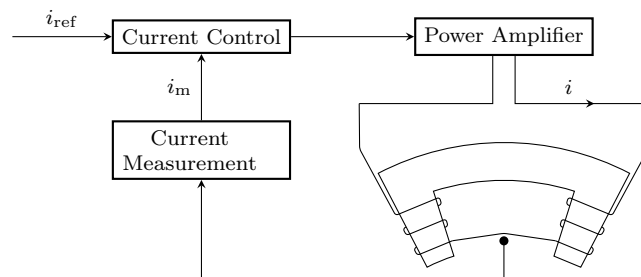


Figure 2.6. Current control scheme. The reference current (i_{ref}) is provided by the position controller. The inner current controller follows the reference based on the measured current (i_{m}) in the coil of an AMB system.

two amplifiers are required for the axial bearing, resulting thus in ten amplifiers. The amount of power electronics varies with the number of poles and the winding scheme. Thus, the smallest possible number of poles for the radial case is three. In that case, three amplifiers are necessary for each radial bearing.

To obtain a transfer function that approximates the actuator behavior, the voltage over load should be written as

$$u = \frac{d\psi}{dt} + Ri = \frac{\partial\psi}{\partial i} \frac{di}{dt} + \frac{\partial\psi}{\partial x} \frac{dx}{dt} + Ri = L \frac{di}{dt} + k_u \frac{dx}{dt} + Ri, \quad (2.15)$$

where R and L are the resistance and inductance of a coil, and k_u is the coefficient of the velocity-induced voltage. The rotor position is constantly changing around the operating point, thereby causing changes in the air gap. These changes affect the inductance L and induce additional voltage with respect to the direction of the movement. As these deviations from the center point are relatively small, the inductance is usually assumed constant and the induced voltage is neglected. Under these assumptions and an assumption that the coil resistance R is small, the following transfer function is obtained

$$G_{cc} = \frac{i_m}{i_{ref}} \approx \frac{G_P}{sL + G_P}, \quad (2.16)$$

where G_P is the proportional gain of the PID current controller and s is a Laplace variable. In the particular implementation of the PID controller, only the proportional gain is used, while differential and integrative parts are omitted. Another model is based on the bandwidth w_{bw} approximation of an actuator, written as

$$G_{cc} \approx \frac{w_{bw}}{s + w_{bw}}. \quad (2.17)$$

This is particularly useful when a third-party ready-made solution is used as a power amplifier. With the current measurements available, the bandwidth can be estimated experimentally or by the following equation (Jastrzebski, 2007):

$$w_{bw} = \frac{\ln(9)u_{dc}}{Li_{max}}. \quad (2.18)$$

In addition to the current control scheme presented above, there are voltage and flux control approaches. The voltage control requires more sophisticated techniques compared with the simple PID solution. The flux control requires flux sensors that are less robust and more expensive than current sensors. In addition, flux sensors should be mounted directly on the surface of an electromagnet thereby reducing the useful area. However, the force reduction less than 3% was demonstrated with modern Hall sensors (Kjølhed and Santos, 2007).

2.4 Rotordynamics

An essential part of the system is the rotor. A field of science known as rotordynamics provides a theoretical description of rotating bodies. An example of the rotor with an

impeller used in the experimental setup is presented in Fig. 2.7. It can be seen that the rotor has many parts made of different materials and having a complex geometry. This section provides a description of a rotor as a dynamic system.

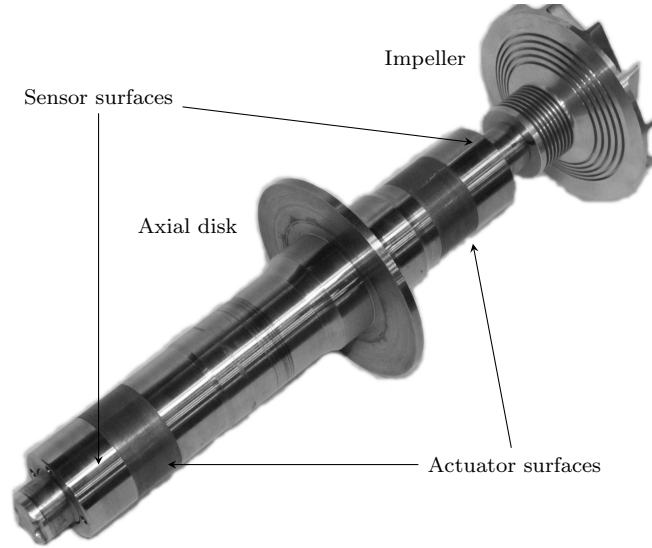


Figure 2.7. Photo of the second rotor with an impeller.

In the examined system, two types of rotors are applied. The first one uses a titanium tube to hold the permanent magnet. The second rotor is an optimized variant of the first one. The optimization is performed from the manufacturing point of view. The number of parts is reduced and rare materials are replaced by more common ones. Thus, the magnet in the second rotor is held by an ordinary steel tube. In this work, these rotors are referred to as the first and second one.

For the decoupled control system, a simple dynamics of the rotor as a point mass object can be considered. This approach is adopted in the axial bearing, but it is also used in the radial case for PID controllers. Thus, combining Eq. (2.12) with Newton's second law, the following model is obtained for one direction

$$ma = k_i i_{x,c} + k_x x, \quad (2.19)$$

where m is the rotor mass and a is the acceleration of the rotor. The acceleration is a second derivative of displacement with respect to time $\ddot{x} = a$. By applying several algebraic operations, the following state-space model is obtained

$$\begin{aligned} \begin{bmatrix} \dot{x} \\ \ddot{x} \end{bmatrix} &= \begin{bmatrix} 0 & 1 \\ \frac{k_x}{m} & 0 \end{bmatrix} \begin{bmatrix} x \\ \dot{x} \end{bmatrix} + \begin{bmatrix} 0 \\ \frac{k_i}{m} \end{bmatrix} i, \\ y &= [1 \quad 0] \begin{bmatrix} x \\ \dot{x} \end{bmatrix}. \end{aligned} \quad (2.20)$$

Although the model described in Eq. (2.20) is sufficient for some applications, in order to achieve a higher accuracy, more robustness, and a better performance, a more detailed model is required. It can be obtained from the same actuator equations and Newton's second law but including a coupling between the different inputs and outputs of the system. These coupled models can be structured to the rigid and flexible models. Flexibility can be neglected, and a rigid model is applied to the subcritical systems. These systems operate below the frequency of the first bending mode of the rotor and can be assumed rigid and the difference can be introduced as uncertainty (Lu et al., 2008). Supercritical systems operate above the first flexible mode, and therefore, it is crucial to include flexibility in the model.

In general, the rotor model can be presented as follows:

$$\mathbf{M}\ddot{\mathbf{q}}(t) + (\mathbf{D}_M + \Omega\mathbf{G}_M)\dot{\mathbf{q}}(t) + \mathbf{K}\mathbf{q}(t) = \mathbf{F}(t), \quad (2.21)$$

where \mathbf{M} is the mass matrix, \mathbf{D}_M is the damping matrix, Ω is the rotor rotational speed, \mathbf{G}_M is the gyroscopic matrix, \mathbf{K} is the stiffness matrix, \mathbf{F} is the force vector, and \mathbf{q} is the generalized displacement vector.

2.4.1 Rigid rotor

A rigid rotor and two radial magnetic bearings are considered. The model describes the motion of a rotor with respect to the center of mass with the state vector $\mathbf{q} = [x \ y \ \beta_x \ \beta_y]^T$. The displacement along a particular axis is denoted by x and y , β_y is rotation around the y axis, and β_x is rotation around the x axis. That way, a four-degrees-of-freedom (DOFs) system is presented. The fifth DOF with motion along the z axis is not coupled with the others, and it is treated separately with axial bearings. The sixth DOF (rotation around the z axis) is included in the equations indirectly as a multiplier for the gyroscopic matrix. The positions of the sensors and the actuators are not collocated, and thus, some additional transformations are required to shift them to the center of mass. As a result, the equation for the center of mass is written as

$$\mathbf{M}\ddot{\mathbf{q}} + \Omega\mathbf{G}_M\dot{\mathbf{q}} = \mathbf{F}. \quad (2.22)$$

The matrices are constructed as follows

$$\mathbf{M} = \begin{bmatrix} m & 0 & 0 & 0 \\ 0 & m & 0 & 0 \\ 0 & 0 & I_y & 0 \\ 0 & 0 & 0 & I_x \end{bmatrix}, \quad \mathbf{G}_M = \begin{bmatrix} 0 & 0 & 0 & 0 \\ 0 & 0 & 0 & 0 \\ 0 & 0 & 0 & I_z \\ 0 & 0 & -I_z & 0 \end{bmatrix}, \quad \mathbf{F} = \begin{bmatrix} f_x \\ f_y \\ \theta_x \\ \theta_y \end{bmatrix}, \quad (2.23)$$

where I_x and I_y are the transversal moments of inertia about the x and y axes, respectively, I_z is the rotational moment of inertia about the z axis, f_x and f_y are the forces acting in the x and y directions, respectively, and θ_x and θ_y denote the moments applied to the same axis. These coordinates are demonstrated in Fig. 2.8.

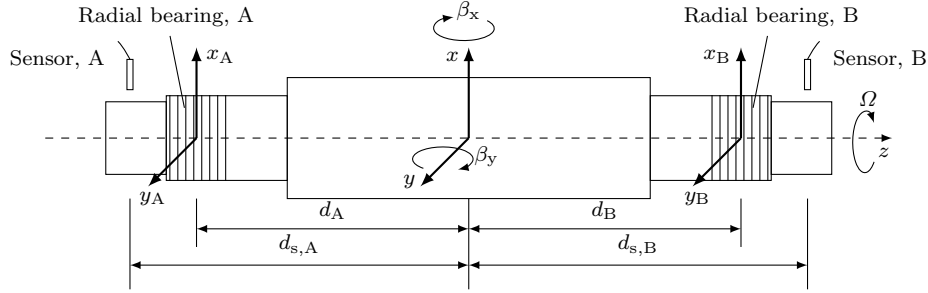


Figure 2.8. Different coordinate systems of a rotor.

The same equation can be written in bearing coordinates

$$\mathbf{M}_b \ddot{\mathbf{q}}_b + \Omega \mathbf{G}_b \dot{\mathbf{q}}_b = \mathbf{K}_x \mathbf{q}_b + \mathbf{K}_i \mathbf{i}_c, \quad (2.24)$$

where the subscript b denotes the bearing coordinates $\mathbf{q}_b = [x_A \ y_A \ x_B \ y_B]$, x_A , and y_A denote the displacement along the x and y axes in bearing A, and with the subscript B in bearing B, respectively, and the control current vector $\mathbf{i}_c = [i_{c,x,A} \ i_{c,y,A} \ i_{c,x,B} \ i_{c,y,B}]$ denotes the current of electromagnets at bearings A and B and in the x and y directions, respectively. The transformation from center coordinates to bearing coordinates is made as

$$\mathbf{q}_b = \mathbf{T}_1 \mathbf{q}, \quad (2.25)$$

$$\mathbf{G}_b = \mathbf{T}_2^T \mathbf{G}_M \mathbf{T}_2, \quad (2.26)$$

$$\mathbf{T}_2 = \mathbf{T}_1^{-1} \quad (2.27)$$

$$\mathbf{q}_s = \mathbf{T}_s \mathbf{q}, \quad (2.28)$$

where the subscript s denotes the sensor coordinate system. The transformation matrices themselves are written as follows

$$\mathbf{T}_1 = \begin{bmatrix} 1 & 0 & 1 & 0 \\ 0 & 1 & 0 & 1 \\ 0 & -d_A & 0 & d_B \\ -d_A & 0 & d_B & 0 \end{bmatrix}, \quad \mathbf{T}_s = \begin{bmatrix} 1 & 0 & 1 & 0 \\ 0 & 1 & 0 & 1 \\ 0 & -d_{s,A} & 0 & d_{s,B} \\ -d_{s,A} & 0 & d_{s,B} & 0 \end{bmatrix}, \quad (2.29)$$

where d is the distance from the center of mass to the sensor or the actuator and the corresponding bearing.

2.4.2 Flexible rotor

It was mentioned above that all rotors are flexible, and it depends on the application, the geometry of the rotor, and the operating speed whether it is necessary to include the flexible modes in the model. To model the flexibility, the rotor is divided into a finite set of similar elements. This approach is known as FEM modeling. The rotors

are usually axisymmetric in the xy plane, and thus, the elements are presented by a cylinder. The behavior of each cylinder is described as a behavior of a Timoshenko beam. The approach takes into account the rotational inertia that is evidently required for rotational machines. Another benefit is the implementation of shear deformation, which is particularly useful for short but very thick rotors. Thus, each element is described by

$$\mathbf{M}_i \ddot{\mathbf{q}}_i + (\mathbf{D}_i + \Omega \mathbf{G}_i) \dot{\mathbf{q}}_i + \mathbf{K}_i \mathbf{q}_i = \mathbf{F}_i, \quad (2.30)$$

the matrices are defined by an analogy to the ones in Eq. (2.21). The mass matrix is denoted \mathbf{M}_i , \mathbf{D}_i is the damping matrix, \mathbf{G}_i is the gyroscopic matrix, \mathbf{K}_i is the stiffness matrix, \mathbf{F}_i is the vector of external forces, and the vector $\mathbf{q}_i = [x_i \ y_i \ \beta_{x,i} \ \beta_{y,i}]^T$ is the vector of states. The subscript i denotes the number of the element $i = 1, 2, \dots, k$. The structure of the matrices corresponds to the one described in Eq. (2.23), but now it describes the i^{th} beam.

The final shape of the rotor is described by a shape function matrix \mathbf{N}

$$\mathbf{q}_i^g = \mathbf{N}(s) \mathbf{q}_i, \quad (2.31)$$

where s is the local longitudinal coordinate for each node, and the superscript g denotes the global coordinate system. The equation of motion for the rotor is written as

$$\mathbf{M}^g \ddot{\mathbf{q}}^g + (\mathbf{D}^g + \Omega \mathbf{G}^g) \dot{\mathbf{q}}^g + \mathbf{K} \mathbf{q}^g = \mathbf{F}^g, \quad (2.32)$$

where $\mathbf{q}^g = [\mathbf{q}_1^g \ \mathbf{q}_2^g \ \dots \ \mathbf{q}_p^g]^T$ denotes the global displacement vector. The model obtained in Eq. (2.32) has a great number of state variables; it is the number of elements used for modeling the rotor multiplied by the number of degrees of freedom. Most of the information is excessive as only the few first flexible modes suffice for control purposes. Thus, model reduction techniques are used to include only the required information. Truncating the high-frequency modes and applying modal coordinate transformation to Eq. (2.32), the physical model is converted to the modal one.

The modal transformation produces the rigid body motion eigenvectors $\phi_1^m, \phi_2^m, \phi_3^m, \phi_4^m$ that correspond to two translational motions and two rotational motions. To these modes M , the flexible modes ϕ_5, \dots, ϕ_M^m are added. The final reduced mode shape function matrix is written as

$$\Phi^m = \begin{bmatrix} | & | & | & | \\ \phi_1^m & \phi_2^m & \dots & \phi_M^m \\ | & | & | & | \end{bmatrix}, \quad (2.33)$$

where the superscript m denotes the modal coordinate system.

The frequencies of the eigenmodes are obtained by solving the generalized eigenvalue equation

$$[\mathbf{K}^g - \omega_k^2 \mathbf{M}^g] \phi_k^g = 0, \quad (2.34)$$

where ω_k is the k^{th} eigenfrequency. The equation is solved under an assumption that the rotational speed Ω is zero and the damping is also zero. For the control purposes, to have a better numerical stability, the mass matrix is scaled $\mathbf{M}^m = (\Phi^m)^T \mathbf{M} \Phi^m = \mathbf{I}$.

The equation of motion for the rotor in modal coordinates is written as

$$\mathbf{M}^m \ddot{\mathbf{q}}^m + (\mathbf{D}^m + \Omega \mathbf{G}^m) \dot{\mathbf{q}}^m + \mathbf{K} \mathbf{q}^m = \mathbf{F}^m, \quad (2.35)$$

where the coordinate transformation is carried out as follows

$$\mathbf{q}^g = \Phi^m \mathbf{q}^m. \quad (2.36)$$

In Eq. (2.35), the rotor is rotating at a constant speed and matrices \mathbf{M}^m , \mathbf{K}^m , \mathbf{D}^m are the diagonal mass, stiffness, and damping matrices. The matrix \mathbf{G}^m is a skew symmetric gyroscopic matrix. These matrices are obtained by modal transformation as follows

$$\begin{aligned} \mathbf{M}^m &= (\Phi^m)^T \mathbf{M} \Phi^m, & \mathbf{K}^m &= (\Phi^m)^T \mathbf{K} \Phi^m, \\ \mathbf{G}^m &= (\Phi^m)^T \mathbf{G} \Phi^m, & \mathbf{D}^m &= (\Phi^m)^T \mathbf{D}_M \Phi^m, \\ \mathbf{F}^m &= (\Phi^m)^T \mathbf{F} \Phi^m. \end{aligned} \quad (2.37)$$

A dynamic model of the flexible rotor that describes the motion in radial magnetic bearings is obtained. An arbitrary number of flexible modes can be included based on the desired operating speed and accuracy of the model. The model covers the motion in five degrees; the displacement along the x and y axes, and the rotation around the x , y , and z axes. Such a model is sufficient for implementing the control of radial AMBs.

2.4.3 Rotors of the test rig

The test rig is composed of one stator and two rotors. Each rotor is tested separately and with an impeller attached to one end. This results in four different variants of the system. The FEM results are summed up in Table 2.1. FEM models used for the evaluation of the system are shown in Figs. 2.9–2.12. The dashed and solid arrows indicate the positions of the sensors and the actuators, respectively. The applied FEM does not provide damping for the flexible modes, and thus, it should be obtained either by EMA or by identification. The EMA is usually performed before assembling

Table 2.1. FEM results for different rotors.

Rotors	Mass, [kg]	Number of nodes	1st flexible frequency, [Hz]	2nd flexible frequency, [Hz]
Rotor 1	2.506	25	1951	5710
Rotor 1 + impeller	2.684	26	1391	2659
Rotor 2	2.621	27	2436	5774
Rotor 2 + impeller	2.799	28	1285	2576

the system in the stator. It also provides the frequencies of the flexible modes, and it is used to fine-tune the FEM model to the measured data. Tuning of the models is necessary as the rotors consist of several parts, and the connections between these parts are difficult to model. Additionally, it is not straightforward to get the stiffness for the lamination used in radial bearings. All these challenges produce a difference between the FEM model and the actual rotor. (Mushi et al., 2012)

Along with the frequencies and damping of the flexible modes, the shapes of the modes play a crucial role in the AMB system. The shape function that crosses the zero point in the position of an actuator or a sensor is uncontrollable or insensible, respectively. The shape function with the positions of sensors and actuators are demonstrated in Fig. 2.13.

2.5 Overall Plant Model

Combining the equation of motion for the flexible rotor with the equation of the linearized forces provided by electromagnets, we can obtain the following model of the system

$$\mathbf{M}^m \ddot{\mathbf{q}}^m + (\mathbf{D}^m + \Omega \mathbf{G}^m) \dot{\mathbf{q}}^m + (\mathbf{K}^m + \mathbf{K}_x^m) \mathbf{q}^m = \mathbf{K}_i^m \mathbf{i}_c, \quad (2.38)$$

where the current \mathbf{K}_i^m and position \mathbf{K}_x^m stiffnesses are translated into the center of mass. They are obtained similarly as in (2.37) and have the following form

$$\begin{aligned} \mathbf{K}_i^m &= (\boldsymbol{\Phi}^m)^T \mathbf{S}_a \mathbf{K}_i \boldsymbol{\Phi}^m, \\ \mathbf{K}_x^m &= (\boldsymbol{\Phi}^m)^T \mathbf{S}_a (-\mathbf{K}_x) \boldsymbol{\Phi}^m. \end{aligned} \quad (2.39)$$

The positions of the sensors and the actuators are included into the matrices \mathbf{S}_s and \mathbf{S}_a , respectively. These matrices define the nodes related to the sensors and the actuators in the FEM model of the rotor.

The state-space form of Eq. (2.38) is written as

$$\begin{aligned} \dot{\mathbf{x}}_r &= \mathbf{A}_r \mathbf{x}_r + \mathbf{B}_r \mathbf{u} \\ \mathbf{y}_r &= \mathbf{C}_r \mathbf{x}_r + \mathbf{D}_r \mathbf{u}. \end{aligned} \quad (2.40)$$

The matrices \mathbf{A}_r , \mathbf{B}_r , \mathbf{C}_r , and \mathbf{D}_r are calculated as

$$\begin{aligned} \mathbf{A}_r &= \begin{bmatrix} \mathbf{0} & \mathbf{I} \\ -(\mathbf{M}^m)^{-1}(\mathbf{K}^m + \mathbf{K}_x^m) & -(\mathbf{M}^m)^{-1}(\mathbf{D}_r + \Omega \mathbf{G}^m) \end{bmatrix}, \\ \mathbf{B}_r &= \begin{bmatrix} \mathbf{0} \\ -(\mathbf{M}^m)^{-1} \mathbf{K}_i^m \end{bmatrix}, \quad \mathbf{C}_r = [\mathbf{S}_s \boldsymbol{\Phi}^m \quad \mathbf{0}], \quad \mathbf{D}_r = \mathbf{0}. \end{aligned} \quad (2.41)$$

The state vector \mathbf{x}_r combines both the modal position and the velocity $\mathbf{x}_r = [\mathbf{q} \quad \dot{\mathbf{q}}]^T$. The inputs to the system are the control currents for each bearing in each plane $\mathbf{u} = [i_{c,A,x} \ i_{c,A,y} \ i_{c,B,x} \ i_{c,B,y}]^T$. The outputs are the positions of the rotor at each bearing $\mathbf{y}_r = [x_A \ y_A \ x_B \ y_B]$.

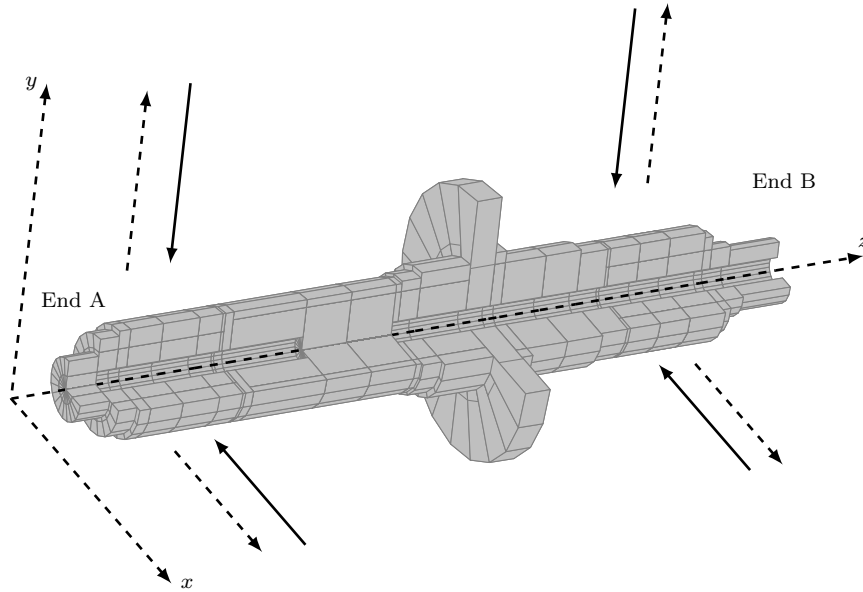


Figure 2.9. FEM model of the first rotor for the blower system. The positions of the actuators and the sensors are indicated by solid and dashed lines.

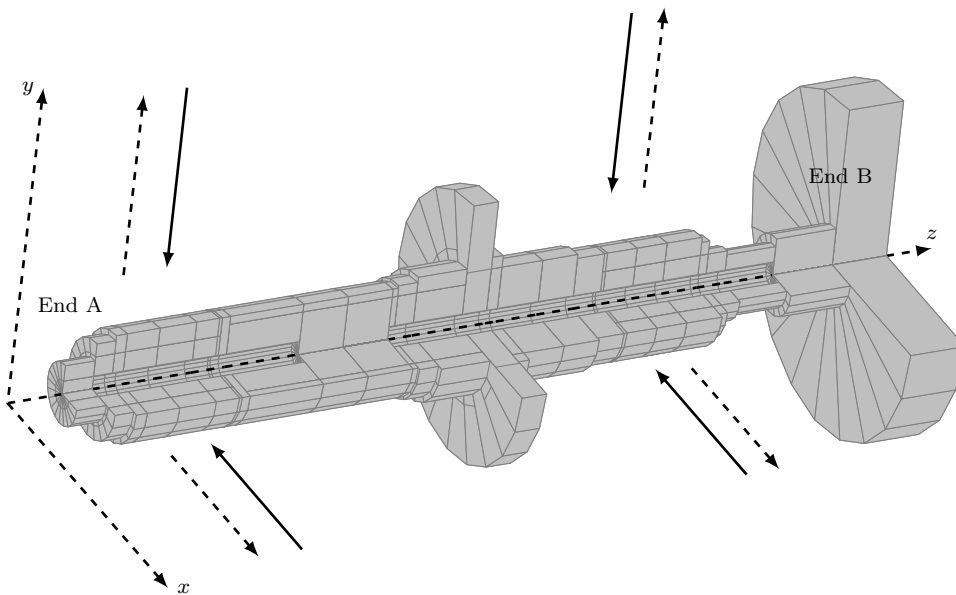


Figure 2.10. FEM model of the first rotor for the blower system with an impeller. The positions of the actuators and the sensors are indicated by solid and dashed lines.

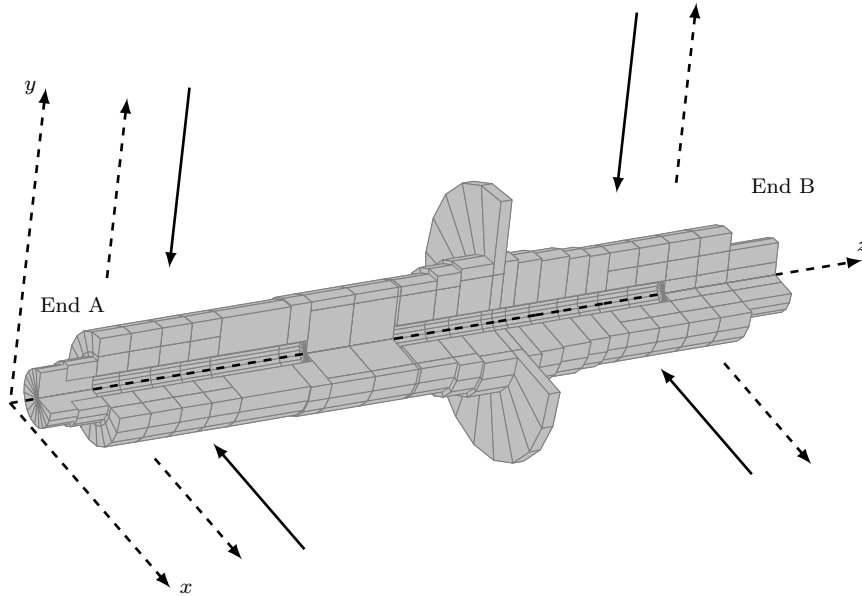


Figure 2.11. FEM model of the second rotor for the blower system. The positions of the actuators and the sensors are indicated by solid and dashed lines.

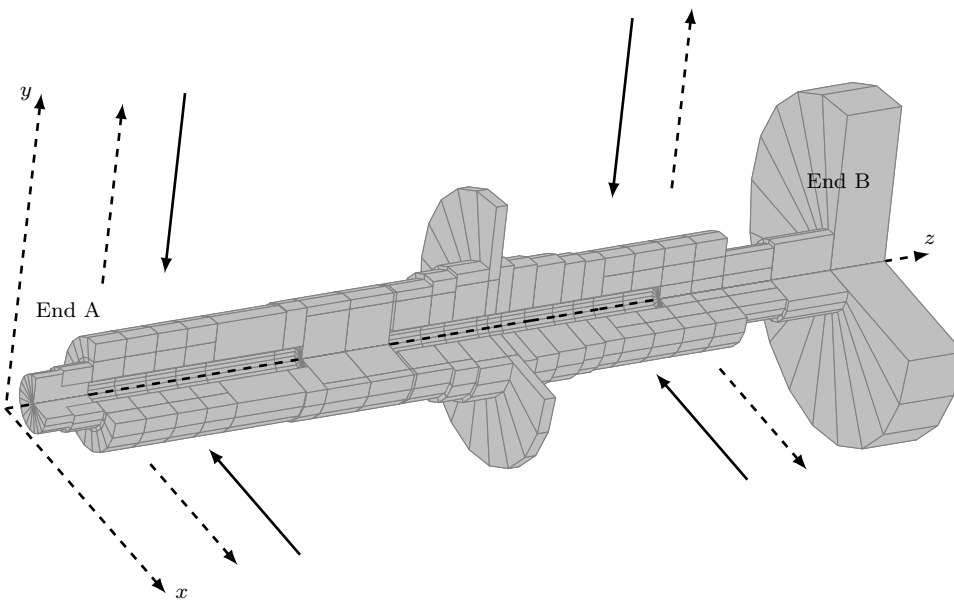
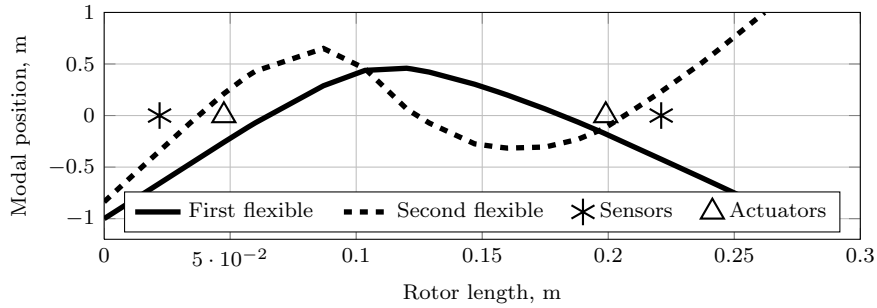
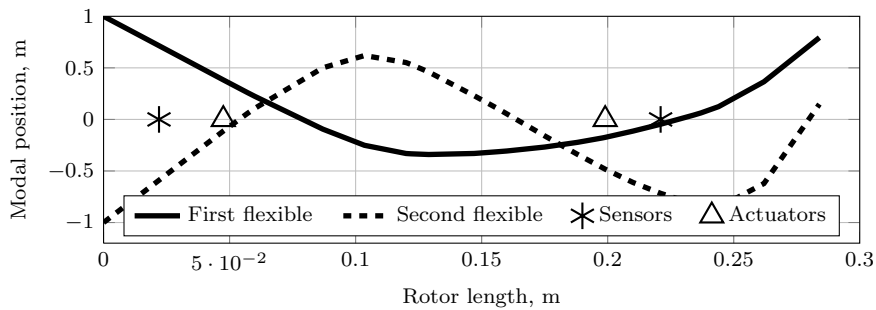


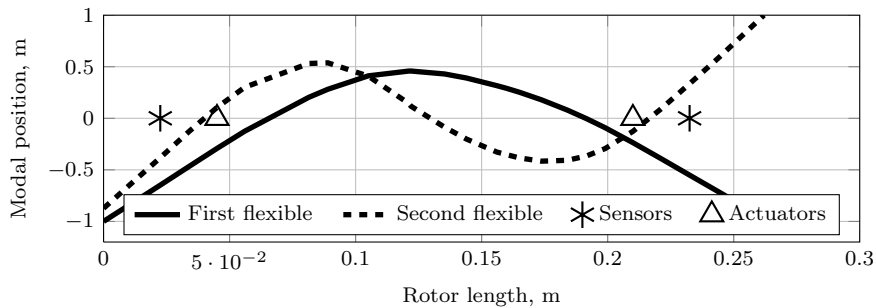
Figure 2.12. FEM model of the second rotor for the blower system with an impeller. The positions of the actuators and the sensors are indicated by solid and dashed lines.



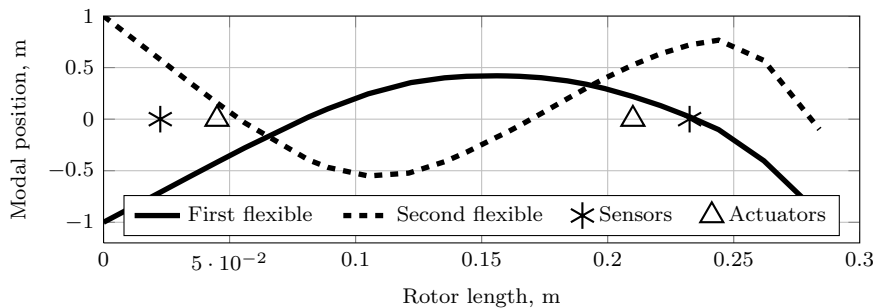
(a) First rotor



(b) First rotor with an impeller



(c) Second rotor



(d) Second rotor with an impeller

Figure 2.13. Mode shapes of the rotors. The first two flexible modes are presented for each rotor. The modes are scaled so that the maximum displacement from the center position is 1 m. The positions of the sensors and the actuators are also denoted.

The full plant model consists of a reduced rotor model and the linearized actuator dynamics. It can be expressed in the form of first-order differential equations suitable for controller synthesis.

$$\begin{aligned}\dot{\mathbf{x}} &= \mathbf{A}\mathbf{x} + \mathbf{B}\mathbf{u} \\ \mathbf{y} &= \mathbf{C}\mathbf{x} + \mathbf{D}\mathbf{u}\end{aligned}\quad (2.42)$$

$$\begin{aligned}\mathbf{A} &= \begin{bmatrix} \mathbf{A}_a & \mathbf{0} \\ \mathbf{B}_r\mathbf{C}_a & \mathbf{A}_r \end{bmatrix}, \quad \mathbf{B} = \begin{bmatrix} \mathbf{B}_a \\ \mathbf{0} \end{bmatrix}, \\ \mathbf{C} &= [\mathbf{0} \quad \mathbf{C}_r], \quad \mathbf{D} = \mathbf{0}.\end{aligned}\quad (2.43)$$

The state vector combines the states of the rotor and the actuator $\mathbf{x} = [\mathbf{x}_a \quad \mathbf{x}_r]^T$. The subscripts (r and a) denote the rotor part and the actuator part, respectively.

For the actuator matrices, the simple linearization described in Eq. (2.17) is used for each channel. Thus, the matrices are diagonal $\mathbf{B}_a = -\mathbf{A}_a = \text{diag}([w_{bw} \ w_{bw} \ w_{bw} \ w_{bw}])$ and $\mathbf{C}_a = \mathbf{I}_{4 \times 4}$. The model presented in (2.43) is a linear representation of the rotor-actuator system that describes the dynamics of an AMB system. It is important to list the assumptions made for the linearization of the generally nonlinear system:

1. the rotor operates in the region close to the magnetic center of electromagnets,
2. the deviations of the rotor from the center point are small,
3. the rotor material is considered to be linear and elastic,
4. saturation (B-H curve, current limit, voltage limit) is not considered,
5. the rotor model has a reduced number of flexible modes,
6. the inductance of the electromagnets is constant and does not depend on the rotor position, and
7. the stray flux, flux leakage, and eddy currents are omitted from the magnetic circuit.

These assumptions are quite common in the literature and are widely adopted in the research community to describe a linear AMB system (Schweitzer and Maslen, 2009).

2.6 Axial Magnetic Bearings

Axial magnetic bearings are used to stabilize the system in one direction. The construction is relatively simple compared with the radial case. As usual, two electromagnets are used to provide the attractive force in opposite directions. The details are presented in Fig. 2.14. The electromagnets are of the common U-type. The force provided by

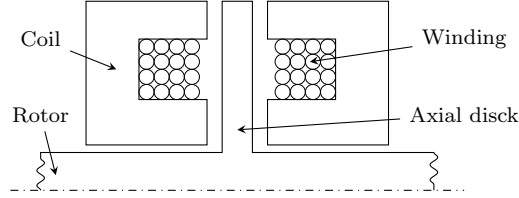


Figure 2.14. Axial thrust bearing. Usually, the axial bearing is presented by two electromagnets and a disc on the rotor with which they interact. Unlike laminated radial bearings, these parts are made of solid steel.

one electromagnet is expressed by the same equation Eq. (2.8) as for the radial case. The difference is that the angle χ in the axial case is zero.

The axial bearings, unlike the radial ones, are quite seldom laminated. The lamination of an axial disk is challenging. Thin sheets cannot withstand stresses at high rotational speeds. Thus, a solid iron disc is usually used. In a solid medium under a constantly changing magnetic flux, eddy currents are generated. These currents cause ohmic losses and limit the rate of flux change. These effects produce additional boundaries for the system performance. The eddy currents in axial bearings are widely investigated by numerous authors (Knospe and Zhu, 2011; Fukata et al., 1991; Sun et al., 2009). Using the results of Zhu and Knospe (2010) with the correction to the axial bearings used, the effect of eddy currents is estimated to be negligible. The estimation is based on the following inequality

$$R^0 \geq \frac{c^2 \mathcal{R}_{\text{ax}}}{N^2}, \quad (2.44)$$

where \mathcal{R}_{ax} is the resistance of an axial coil, N is the number of turns in axial bearings, R^0 is the static reluctance coefficient, and c is the eddy current coefficient for the magnetic path approximation. The last two coefficients describe the frequency domain model of the magnetic contour including the eddy currents in the following manner

$$R = R_0 + c\sqrt{s}, \quad (2.45)$$

where s is the Laplace variable. For the nominal air gap, the right-hand part of inequality (2.44) is 40 times as high as the left-hand part; when the air gap is increased, also this value is growing. Thus, the eddy currents can be neglected in the system under study.

2.7 Conclusions

This chapter provided the description of an AMB system with an application to a specific prototype. The description was based on physical laws and was summed up in the state-space form.

The most complicated dynamics in the system was presented by the rotor and the actuator. These two elements were analyzed individually in detail.

In the actuator part, a conversion of current from power amplifiers into magnetic force was discussed. The process is complex and highly nonlinear including current saturation and magnetic flux saturation. An approach to linearize the system behavior with a classical method of bias currents was described.

The model of the rotating rotor has a complex and high-dimensional description. Under several assumptions applied to the material properties and connections between different parts, the rotor can be considered linear. The process of obtaining a linear model was presented, and methods used to reduce it to a reasonable size were described.

Power amplifiers were also discussed and presented by a first-order transfer function. The bandwidths of the sensors used in the system are high enough to consider their effect negligible for a general description.

The applicability and limitations of the methods applied to the axial bearings were presented and discussed. The main difference compared with the radial case is the absence of lamination in axial bearings, and thus, eddy currents have a stronger effect on the system. It was demonstrated that for a particular system, the effect is negligible for the controller synthesis procedure. As a result, a physical model was obtained. Further, the model will be used in the identification procedure and for the controller synthesis.

Chapter 3

Commissioning of Active Magnetic Bearings

In this chapter, commissioning of an AMB system is discussed. The process is divided into two stages. The problems of the second stage are discussed. The possible ways to overcome these problems are proposed. The process includes an initial checkup of the system and preparation for the levitation. Most of the problems are mathematically treated as linear matrix inequalities (LMIs) that are efficient to solve. The discussion in the chapter is limited to the systems that operate in the open loop.

3.1 Overview

As it was discussed in Chapter 2, an AMB system is a complex mechatronics product. On the other hand, its sophisticated nature also provides great benefits. A drawback is that it requires a lot of attention during the assembly and commissioning.

The commissioning can be divided into two phases according to the location where it is carried out. It can take place at the manufacturer's facility during the assembly. This part can be called the "initial" phase. During the initial phase, each component can be tested individually and tuned separately. Thus, numerous additional test setups and instruments are required.

The second phase, here referred to as the “final” phase, is carried out in the field at the end user. In that case, the tuning of the system is limited and should be done for the system at a general level. Although there is an opportunity to test the components individually, the accuracy is much lower. Another important factor is the distance between the manufacturer and the customer, as they can be located geographically far from each other, and for instance national borders may also introduce some time delays.

Plenty of attention has been paid to the problems of the final phase. These problems have introduced a field for techniques that allow to facilitate the tuning, and to perform it either remotely or fully automatically. Thus, the commissioning time is reduced.

3.2 Sensor tuning

A sensor is an essential part of an AMB system. The accuracy of the measurements affects the stability of the plant. To improve the accuracy, each sensor requires a calibration. The calibration can be done in several steps. The first one is to determine the linear gain of the sensor. The second one is to find a correct offset.

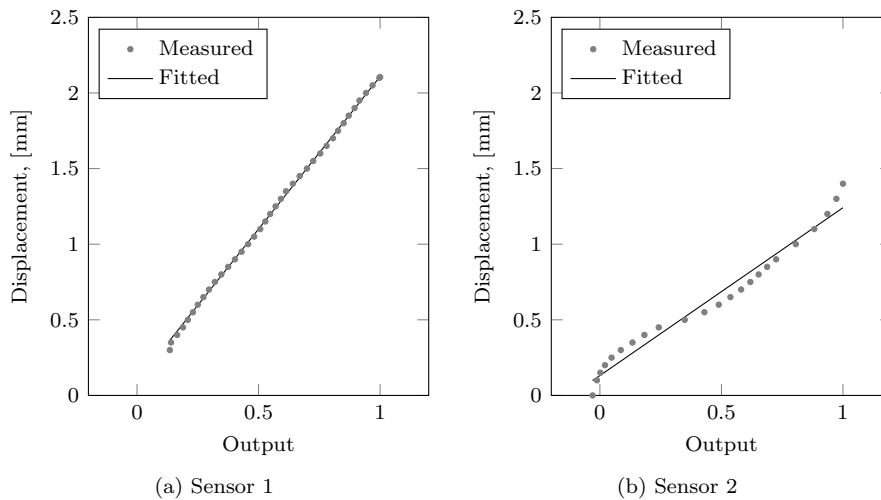


Figure 3.1. Input/output relation for the actual measurements and their approximation. The measured data are usually approximated by the linear function. In a case where the deviations are too large, either splines or a look-up table are used.

The linear gain is obtained by comparing the sensor output with a known distance to the measured object. This is done with a micrometer and a polished piece of the target material. Based on the data obtained, the input-output relation can be approximated

by a linear function

$$y = \beta_1 x + \beta_0. \quad (3.1)$$

Higher-order polynomials or a look-up table can be used to minimize the error. In Fig. 3.1, the measured data for two sensors are presented. The left-hand presentation is almost linear, and a linear approximation is used. The second illustration demonstrates a slight nonlinearity, and to overcome this, a look-up table is implemented.

The second tuning should be carried out during the commissioning of the system in the field. As a result, an offset, that is, the term β_0 in Eq. (3.1) should be obtained. There are lots of different factors that can affect the offset of a sensor. Besides straightforward mechanical reasons, these can include external magnetic fields close to the sensor tip, and the length and arrangement of the sensor cabling.

In the calibration of AMBs, the sensor offset is only a midway task, the final target being to be able to estimate the center of the rotor in the sensor plane. In a general case, the movement of the rotor in the xy plane is regulated by the control law. The idea is to stabilize the rotor in the midpoint and keep it there regardless of all the incoming disturbances. In the case of a failure, auxiliary bearings are used that can withstand several rotor drops at the nominal speed. These auxiliary bearings are the boundary of the rotor movement in the xy plane. The center of the boundary is a geometric center and the desired point to keep the rotor in to avoid an accidental touch of the safety bearings during the operation.

The above-described boundary should be a circle up to the manufacturing tolerance. In the suggested approach, a center can be estimated at a standstill using AMBs without any extra hardware. There are different types of bearings (homopolar and heteropolar) with different numbers and arrangements of electromagnets. A common feature is that the electromagnets are evenly distributed around the rotor. By providing enough current to each electromagnet or to the nearest pair at the same time, it is possible to obtain the number of points that is twice the number of electromagnets. All these points are at the boundary of the safety bearings.

In Fig. 3.2, three different cases are demonstrated. The energized electromagnets are indicated by thicker lines and filled by a grid pattern. The centered rotor position is illustrated by a thin dashed circle. The first figure demonstrates the rotor position under the gravitational force. This is the position of the system at rest. In Fig. 3.2b, the rotor position is presented for the case when current is applied to one electromagnet. The rotor moves as close as possible to the energized electromagnet. The movement is limited by auxiliary bearings. The other case when two neighboring electromagnets are energized is demonstrated in Fig. 3.2c. As two electromagnets have current, the rotor tends to take the position in the midpoint. This way, by applying current to one electromagnet or to the neighboring pair, the boundary positions of the rotor on the auxiliary bearings are estimated. The points obtained from the measurements in the demonstrated rotor positions are presented in Fig. 3.2d, where g_a is the air gap between the rotor and the auxiliary bearings.

With the above-mentioned set of points, it is easy to obtain the initial offset for the sensors. It is done by finding the center point from the maximum and minimum displacements from all the measured points for a particular sensor. After that, depending on the arrangement of sensors, a transformation may be required. The transformation converts the distance between the sensors and the rotor surface into the xy coordinate system of the rotor center. Providing the transformation, the measured set is transformed into xy coordinates.

Instead of searching a circle that best fits the obtained set of coordinates, it is possible to find the largest circle that is inscribed in the figure. The figure is obtained by connecting each point to the nearest one with a straight line. For example, in the case of a heteropolar system with four electromagnets, this should roughly result in an octagon. The problem does not depend on the number of electromagnets and can be converted into a problem of finding a Chebyshev center of a polyhedron. This is a classical example of a convex optimization problem (Boyd and Vandenberghe, 2004).

In the mathematical language, it is necessary to find the largest Euclidean ball

$$\mathbf{B}_{\text{Eu}} = \{\mathbf{x}_c + \mathbf{u} \mid \|\mathbf{u}\|_2 \leq r\} \quad (3.2)$$

that is lying in a polyhedron described by linear inequalities

$$\mathbf{P}_{\text{Eu}} = \{\mathbf{x} \mid \mathbf{a}_i^T \mathbf{x} \leq \mathbf{b}_i, \quad i = 1, \dots, m\}. \quad (3.3)$$

In Eqs. (3.3) and (3.2), \mathbf{x} is a vector of the xy coordinates, \mathbf{a}_i and \mathbf{b}_i are the coefficients of the line that connects the two nearest points, m - is the number of points, \mathbf{x}_c is the center of the inscribed circle with the radius r , and \mathbf{u} is any arbitrary vector with the corresponding dimensions. Each inequality represents a surface in the n -dimensional space. In that particular case with only two dimensions, the inequalities are reduced to planes, and the target is to find the center and radius of a circle.

Each inequality in the set (3.3) limits the search space to half plane on one side of the line. The line is constructed between two nearest points as it is demonstrated in Fig. 3.2d for two points and in Fig. 3.4 for the full set. After constructing the line, the correct half plane should be specified for the inequality. For that purpose, it is necessary to find on what side the center point is lying. Approximate coordinate values of the center point can be found as an average of all the measured points. An example presented in Fig. 3.3 shows how a set of points forms a polyhedron. The gray area is the feasible space defined by the inequalities (3.3). A ball with the largest radius fitted in the polyhedron is indicated by a dashed line. The thick outer circle describes the boundary on which the points are lying. Under ideal conditions, the centers of the inner and outer circles coincide. With noise measurements and disturbance forces these centers are different. However, the center for the inner ball corresponds to the worst conditions and thus meets the safety requirements.

Detailed information on the coordinate transformation, obtaining the offsets, and calculating the coefficients for inequalities is given in Appendix A. An example is provided for one B end and one set of measurements for a case with the rotor in the

negative z direction. The graphical representation of the example can be found in Fig. 3.4.

One of the benefits of the proposed method is that it does not limit to only one set of points. The distance between the sensor and the rotor can vary under different angles because of the surface roughness. This has to be taken into account because the rotor is rotating during the operation. This distance is also subjected to variations according to the position of the rotor in the axial direction. All these effects can be taken into account and substituted into the same problem (3.3)–(3.2), thereby providing one general solution that should represent the worst-case scenario.

The straightforward variation that can be observed in the system is the position of the rotor along the z axis. For the open-loop measurements, the rotor can be either in the most positive or in the most negative direction. For both cases, a full set of points are recorded. According to the above-mentioned procedure, the points are connected and the center of the Euclidean ball is found. The result is presented in Fig. 3.4.

Figure 3.4 shows that the geometric center is found for the worst-case scenario. The results obtained for different positions along the z axis are similar except for the top left plane. The plane for the negative z direction is slightly lower, thereby reducing the operating region for the rotor. This gives insight into why the ball with the largest radius is placed relatively far from the top right corner.

The distribution of the measured points in Fig. 3.4 is not fully even but has a specific pattern. In the lower left corner, the points are placed more densely compared with the top right corner. The reason is the direction of the gravitational vector that provides an additional bias force. A more even distribution, if necessary, can be achieved with more current applied to the electromagnets. That case is demonstrated in Fig. 3.5b, where the measurements were made with the maximum current.

The results presented in Fig. 3.5 are obtained for different positions of the rotor in the z direction and for six different angles. The examined system is a permanent magnet synchronous machine (PMSM) with three pole pairs (Jastrzebski et al., 2012b). The rotor tends to stabilize its angular position to one of these poles. The results obtained for the end B have a relatively small deviation. All the measured positions are close to the predicted points. However, the results for the end A show a significant deviation. There can be several explanations for this. The first one is a runout on the sensor surface and/or on the surface that comes in contact with the auxiliary bearings. The second reason is the above-mentioned permanent magnet that provides an additional force and shifts the rotor to the poles of the electrical machine.

To determine what causes the difference in the variation of the rotor angle, the same measurements were repeated with a second rotor. For the second rotor, the runout was measured on the sensor surface and on the surface that touches the auxiliary bearings. The measurements demonstrated a deviation of about $20\ \mu\text{m}$ for the end A. The deviation for the center point calculated separately for each angle also varies in

the range of $\pm 20 \mu\text{m}$ thus showing that the main cause for the difference is the runout. The same estimation for the end B provides a variation in the range of $\pm 7 \mu\text{m}$, which is close to the noise level of the sensors and can be neglected.

The last set of measurements compares the system without an impeller and with an impeller attached to the end B with a special housing. We can see in Fig. 3.7 that the housing of the impeller limits the rotor movement. However, the estimates of the center point are very close for both cases. The result shows that the method demonstrates the worst-case scenario, in which it is possible to estimate a suitable operating point and a safety region. A global solution can be obtained efficiently by converting the problem into a convex optimization framework. To get a solution, a commercial product such as MATLAB can be used, similarly as a number of open source packages and solvers. Software of this kind has lately become available even for embedded systems (Mattingley et al., 2011).

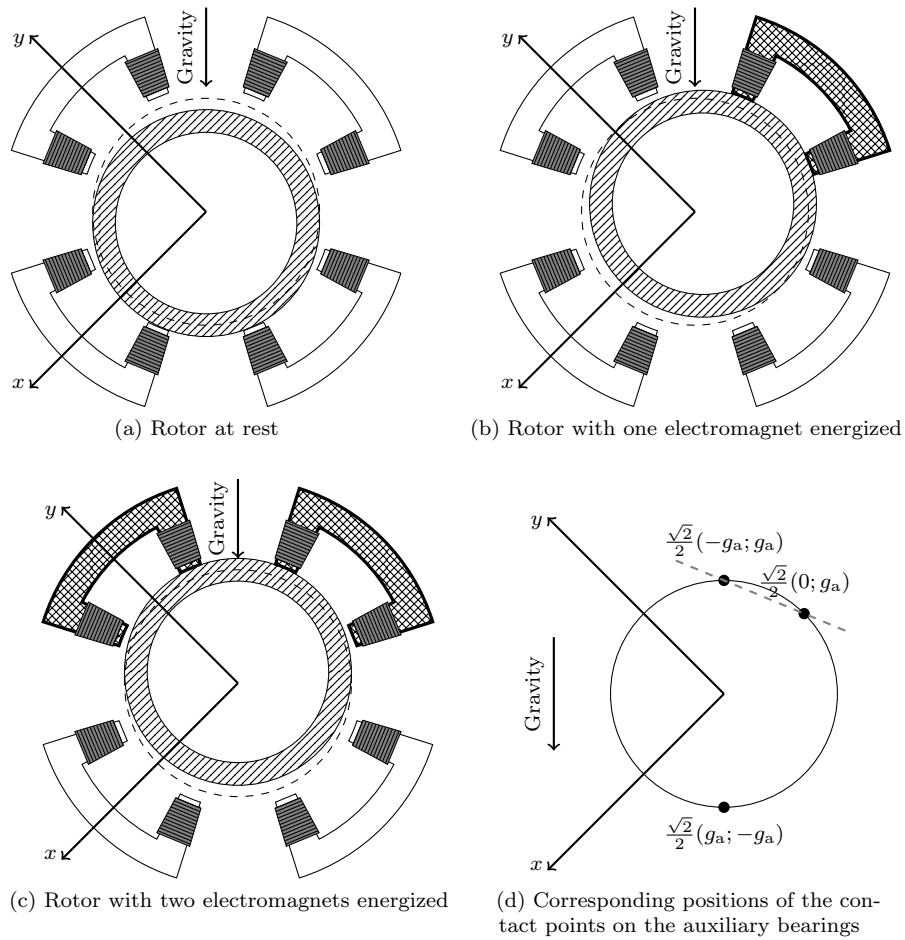


Figure 3.2. Rotor positions for different cases. In the figure, the position of the rotor is demonstrated when current is applied to one or two neighboring electromagnets. The position under the gravitational force is also shown. Further, the theoretical values for these positions are given.

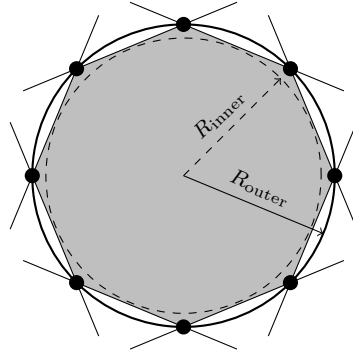


Figure 3.3. Ball fitted inside a polyhedron. The eight evenly distributed points on the surface of the outer circle form a polyhedron. It is obtained by connecting the closest points with a line. The inner circle is the one with the largest radius that fits inside the polyhedron. For ideal measurements and circles, the centers for outer and inner circles coincide.

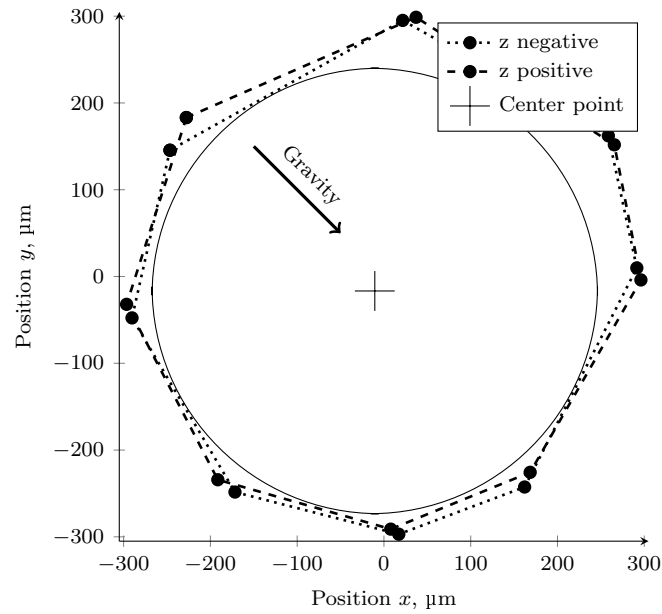


Figure 3.4. Geometric center at one end for two sets of measurements. The difference in the measurements appears as a result of the sensor noise and the rotor movement in the z direction. All the polyhedrons can be combined into one problem to find the worst-case scenario.

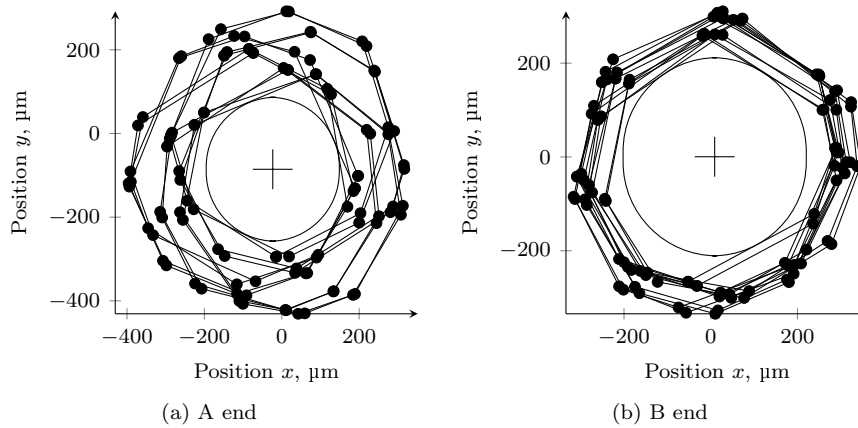


Figure 3.5. Geometric center for the first rotor. The end A is characterized by a significantly greater variation. This is due to the greater runout on the surfaces and a closely placed permanent magnet of an electrical machine.

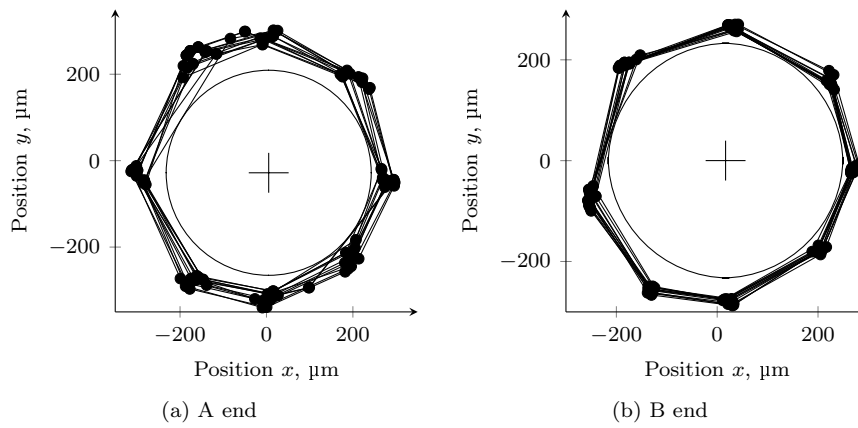


Figure 3.6. Geometric center for the second rotor. For the second rotor, the runout was almost eliminated during the manufacturing process. The variations at the end A are caused by a permanent magnet.

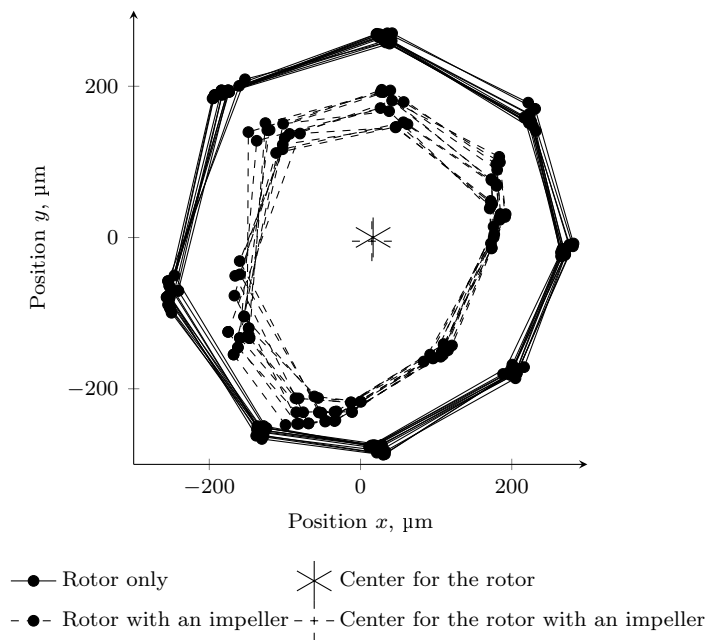


Figure 3.7. Geometric center for the rotor with and without an impeller. The housing for the impeller limits the rotor movement. This leads to a smaller operating range.

3.3 Actuator tuning

Description of the actuator in AMBs was given in Section 2.1. It should be recalled that the actuator is an electromagnet that provides a pulling force in one direction. The number of electromagnets depends on the application in question and its specific requirements. In the case of radial bearings, the smallest number is three, and in this section, the discussion is limited to a radial case unless it is explicitly specified.

All actuators provide their force vector that is translated into an xy plane for control purposes. Transformation to the same plane is made for the sensor measurements. This way, the controller receives information about the xy rotor displacement from the center point and provides the force vector. The force vector is distributed between individual electromagnets, and thus, their geometric sum provides the desired correcting force.

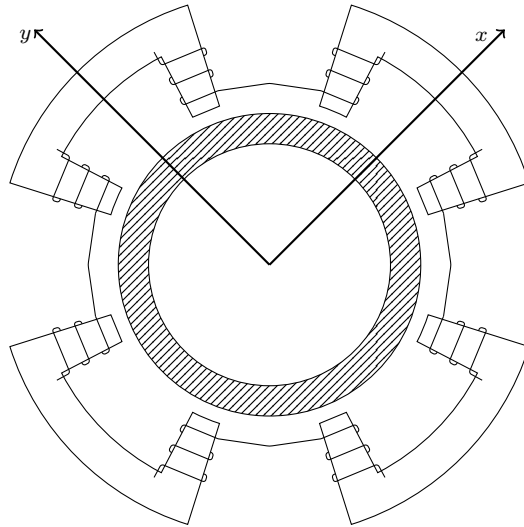


Figure 3.8. Winding misplacement by one tooth. With such a misplacement, the force vector is turned by 45° resulting in a system malfunction.

It is important that the geometric planes of actuators and sensors correspond to each other. If it is physically not constructed, it should be implemented with software coordinate transformations to obtain the correspondence. There can be several reasons for misalignment:

- The actuators and sensors are placed in different positions related to the rotor length, as it is easier from the construction point of view. Thus, they can be placed in different stator parts that have mechanical misalignment.
- The actuator windings in a heteropolar case can be misplaced by one stator tooth, see Fig. 3.8.

Yet another problem is the cabling as there is a separate cable with a separate current source for each electromagnet. The cabling is easily mixed. The problem can be avoided by accurate labeling. However, testing of the product is an important process that should be carried out continuously and repeated in every stage. This is especially true for sophisticated systems. In general, the task of the cable assignment and removal of the misalignment between the sensor and actuator planes can be solved simultaneously. This provides an additional diagnostic tool for the commissioning process.

3.3.1 Cable assignment as a factorial analysis problem

The problem of assigning the cables is stated as follows. There is a defined coordinate system for the sensors that is an xy plane for each radial bearing and an z plane for the axial one. For an ordinary arrangement with two radial and one axial bearings there are five output coordinates. For each output coordinate there is a pair of electromagnets that acts in strictly opposite directions along that coordinate. By providing a set of inputs to the electromagnets and obtaining the measured outputs from the sensors, the corresponding inputs and outputs should be found. In other words, it is necessary to determine in what particular direction the electromagnet drives the rotor.

It is evident that one electromagnet pulls the rotor only in one direction. However, there are also changes in other outputs as they all are interconnected by a solid rotor body. The interest lies in finding only the main effects, neglecting the side effects. This way, the model of the system for analysis can be presented as

$$z_k = \beta_0 + \beta_1 x_{k1} + \beta_2 x_{k2} + \dots + \beta_{kp} x_{kp} + v_k, \quad (3.4)$$

where x_k and z_k denote the inputs and outputs in the k th run of an experiment, respectively. The unknown parameters are represented by a vector $\Theta = [\beta_0, \beta_1, \dots, \beta_{p-1}]^T$, where the subscript p stands for the number of inputs and v_k represents a random error. The presented model shows only the main interaction without considering the side effects of the input multiplications such as $x_{ki}x_{kj}$. Thus, the model is linear both in Θ and \mathbf{x} . It is assumed that the noise has a zero mean $E(v_k) = 0$.

Based on the set of measurements available and the estimate of the unknown parameters, Θ is obtained for a particular output. By generalizing this for the full system, a matrix is obtained that represents the effects of particular inputs for particular outputs. By extracting the main components from the matrix, we find a pair of electromagnets acting in a specific direction.

The above-mentioned linear model for all the measurements can be presented in a matrix notation as

$$\mathbf{Z}_n = \mathbf{H}_n \Theta + \mathbf{V}_n, \quad (3.5)$$

where $\mathbf{Z}_n = [z_1, z_2, \dots, z_n]^T$, $\mathbf{V}_n = [v_1, v_2, \dots, v_n]^T$ and the matrix \mathbf{H}_n consists of rows with a combination of inputs $[x_{k1} \ x_{k2} \ \dots \ x_{kp}]$ that provide a specific response

z_k . The vector of the unknown parameters Θ can be fitted with a well-known least squares method (Spall, 2003, Chapter 3). The loss function has the following form

$$\hat{L}(\Theta) = \frac{1}{2n} (\mathbf{Z}_n - \mathbf{H}_n \Theta)^T (\mathbf{Z}_n - \mathbf{H}_n \Theta). \quad (3.6)$$

When there are enough measurements ($n \geq p$), Eq. (3.6) has a unique solution

$$\hat{\Theta} = (\mathbf{H}_n^T \mathbf{H}_n)^{-1} \mathbf{H}_n^T \mathbf{Z}_n. \quad (3.7)$$

A different measurement vector is substituted for each available output. Thus, a matrix that relates the inputs and outputs is constructed

$$\Phi_{l_o} = [\Theta_1 \ \Theta_2 \ \dots \ \Theta_l], \quad (3.8)$$

where l denotes the number of measured outputs. Each column in the matrix Φ_{l_o} is a specific output, and each row is a specific input of the system. In the intersection there is a coefficient that defines the effect of a particular input on a particular output.

With an implementation of the above-mentioned model and the estimation techniques, the only question remaining is how to choose a relevant input set \mathbf{H}_n . The set should be informative enough so that it is possible to distinguish two inputs from the rest eight inputs for a particular output. These inputs pull the rotor in opposite directions along specific axes.

The system under discussion is not yet in a state where the rotor can be operated with a feedback. In an open-loop case, the small variation in the input signal does not produce any noticeable effect. Thus, the only relevant inputs would be high and low signals. For that case, a factorial design methodology fits perfectly. The method generates inputs for efficient system identification that can have only two levels. The method is also referred to as a 2^m factorial design, where m is the number of factors that can be altered during the experiment. Additionally, in contrast to the one-at-a-time approach, a full factorial design changes several variables simultaneously providing greater efficiency and insight. An extensive discussion about the benefits is provided by Spall (2010).

In the case of AMBs, the low signal is considered as an absence of current in the electromagnet. The high signal is high enough current to definitely drive the rotor to that electromagnet, when only one electromagnet is active. Thus, the low and high signals are denoted by -1 and $+1$.

Factorial design provides input matrices that are orthogonal. It means that the multiplication $\mathbf{H}_n^T \mathbf{H}_n$ gives a diagonal matrix. Orthogonality guarantees that the estimates of Θ are uncorrelated when v_k are uncorrelated.

A full factorial design implies 2^m experiments to be carried out. In the case of AMBs with ten inputs, it leads to $2^{10} = 1024$ experiments. The number is relatively high and leads to a significant time consumption in measurements. In that case, a fractional

factorial design can be used to save time. The approach uses only a fraction of all experiments required for the full factorial design.

The main idea is that the measurements of one effect should not depend on the measurements of other effects. The assumption is valid in the AMB system as the measurements in different ends of the rotor and in the z direction do not significantly affect each other. Furthermore, the measurements in the xy directions should also be independent; however, this is not strictly true. It is not possible in the open loop to move the rotor strictly in one direction. By applying current to one electromagnet, the rotor is driven as close to the electromagnet as possible. There is a gravitational force that may change the rotor position, and additionally, there is some magnetization left on other electromagnets that also affects the position. Taking into account these facts, it should be pointed that the xy planes depend on each other, but the main direction is still distinguished. Thus, the minimum number of independent factors that affect a particular measurement is chosen to be four. In that case, the number of experiments is decreased to 16.

For a statistical analysis, an additional first column of ones is added to each input matrix \mathbf{H} that represents a constant term. The term is denoted β_0 in Eq. (3.4), and should describe the bias value for the measurements. In an AMB system, the center of the rotor is considered to deviate from the midpoint. Thus, this term should be relatively low compared with the others, and may be neglected in the analysis. An example of the input matrix is presented in Table B.1 in Appendix B.

Several sets of measurements are carried out with a different number of input combinations such as 16, 32, 64, and 128. The measurements obtained from the sensors are normalized to the range of $[-1, 1]$ based on the absolute maximum value. The resulting matrices Φ_{i0} for the sets of 16 and 128 are presented in Table 3.1 and Table 3.2. The inputs given on the left in these tables are known a posteriori and included here for the sake of convenience.

When observing the results in Table 3.1 and Table 3.2, we can see that each output column contains easily distinguishable positive and negative values. These values are placed in the rows that correspond to the inputs that affect that direction most. Thus, each output can be connected with two inputs that act in the opposite direction. This solves the problem of finding the corresponding inputs and outputs stated above. In addition, we see that with a number of experiments, the correlation between the inputs and outputs becomes more prominent.

A significant drawback of the input combinations used is the high values in the constant part (the 1st row in each column). According to the above discussion, the term should be negligible. To examine this contradiction, all experiments are compared in Table 3.3 based on the sum of the absolute values of the constant term. Thus, the metric is represented by

$$\varepsilon = \sum_{i=1}^l |\beta_{0i}|, \quad (3.9)$$

Table 3.1. Results obtained by a fractional experiment of the order of 16.

Inputs	Outputs				
	Ax	Ay	Bx	By	z
Constant	6.29	-0.0775	10.1	3.41	-114.0
Ax+	8.91	0.0154	8.77	2.76	-1.90
Ax-	-3.97	0.751	-0.676	-2.33	1.37
Ay+	0.514	4.47	-2.19	2.38	-0.056
Ay-	-0.955	-3.69	1.29	-2.27	-0.927
Bx+	3.93	-2.82	12.1	-2.00	0.613
Bx-	-2.33	0.554	-6.66	-0.925	1.01
By+	4.11	1.49	0.258	6.62	0.622
By-	-1.52	-0.797	-1.76	-3.14	-1.69
z+	-0.238	-1.13	0.726	-0.703	1.66
z-	-0.268	-0.717	0.718	-2.00	-2.80

where β_{0i} is a constant term that corresponds to the output i .

By analyzing the fractional factorial design approach with the values presented in Table 3.3, it is possible to draw several conclusions. First, the constant term does not vary significantly from run to run, as it is seen in the experiments with the same number of measurements. Second, the constant term is greatest for the greatest number of measurements. However, there is now a direct correlation between the number of measurements and the evaluation value. Measurements should not depend on the order of execution as the rotor position is defined only by the currents applied with some small deviations according to the previous step and magnetization left.

The problem is that in the factorial design, a large number of inputs are changing and have a positive value. This leads to a case in the AMB system where two opposite electromagnets are switched simultaneously. In another case there is a current in the radial direction, and there may be not enough force to drive the rotor in the axial direction because of friction. In both situations, for some inputs there are no changes for the specific output.

To overcome the problem related to the factorial analysis, the number of inputs with +1 value at a time was limited to two or three. A full combination of possible inputs is applied, providing 55 and 175 measurements, respectively. These combinations represent limited subsets from the full factorial design. In this arrangement, orthogonality is lost, and thus, the estimated results may have some correlation. Table 3.3 shows that these experiment designs provide the smallest constant term. The resulting matrices are presented in Table B.2 and Table B.3 in Appendix B. We can see that the main effects can be easily recognized. The experiment with 55 measurements is the most effective one based on the time required and the accuracy provided.

Table 3.2. Results obtained by a fractional experiment of the order of 128.

Inputs	Outputs				
	Ax	Ay	Bx	By	z
Constant	7.12	0.401	9.02	2.13	-123.0
Ax+	10.9	0.859	3.82	4.66	-2.69
Ax-	-9.65	-1.11	-3.27	-4.25	2.08
Ay+	0.864	11.9	-4.00	4.92	0.488
Ay-	-1.12	-8.63	2.97	-4.00	-0.336
Bx+	7.18	-8.08	15.5	-0.752	-0.518
Bx-	-4.18	2.33	-8.39	-1.59	-1.24
By+	4.96	4.87	0.298	12.4	-3.39
By-	-3.37	-3.11	0.063	-8.44	-1.06
z+	0.223	-0.173	0.209	1.08	3.24
z-	-0.461	-0.748	-0.297	-0.571	-4.65

In order to fully automate the process of assigning the inputs to the outputs, the AMB system should be able to provide current in the open loop. Additionally, the sensors should be tuned in advance and provide the measurements in two dimensions for radial bearings and in one dimension for the axial bearing. As a final part, an algorithm that chooses the correspondence based on the matrix Φ_{io} is required.

Then implementation of the algorithm is straightforward. The basic idea is to find the elements with an absolute maximum value for each row and column excluding the first row that represents the constant part. Each match between the elements found provide one connection. In the best case, the algorithm should assign all directions in two runs as each column contains values for two electromagnets (positive and negative directions). In other cases, the input (row) is removed from the matrix when it is assigned to the output. The output is removed when it is assigned to two inputs. Additionally, when the output is assigned with either negative or positive inputs, all negative or positive values in that column should be replaced with zeros. This allows to have a more robust fitting in the case of noisy measurements or a poor experiment design. The algorithm is presented as a pseudo code in Listing B.1.

Table 3.3. Comparison of different experiment designs.

Type of input design	Number of measurements	Evaluation value ¹
Iteration	55	3.02
Iteration	55	3.21
Iteration	175	15.1
Iteration	175	16.0
Fractional factorial	64	26.9
Fractional factorial	64	27.3
Fractional factorial	64	29.0
Fractional factorial	32	68.1
Fractional factorial	16	130.0
Fractional factorial	16	134.0
Fractional factorial	128	142.0
Fractional factorial	128	167.0

¹ The evaluation value used here is based on the sum of constant terms for each output. These metric should be low when each new set of measurements moves the rotor to the different position. In a case when after applying a new set the rotor stays in the same position, no new information is obtained and the constant term increases.

3.3.2 Cable assignment and misalignment

As it was mentioned above, the force vector of the actuator should be validated. The planes of the sensors and forces should be correlated to ensure a correctly operating system. In addition, the cable assignment procedure cannot be carried out correctly without correlation.

The problem is explained in Fig. 3.9. The sensor axes are indicated by solid black color, and the actuator plane by gray diagonal lines. In Fig. 3.9a, the planes for the sensors and actuators are perfectly aligned while in Fig. 3.9b there is an angle θ between these planes. For a large angle, the control system will obviously not stabilize the system. The controller can tolerate some difference, but it depends highly on the controller itself.

This kind of a misalignment should be removed from the system. There is a straightforward way to do this by mechanically adjusting the planes. The second solution is to make a coordinate transformation either for the force vector or the position coordinates. The last option is relatively easy to implement in software. In the case of sophisticated controllers that apply the coupling between the rotor ends and planes, it is better to adjust the force vector. Such a transformation corresponds to the original controller and does not require additional modeling effort.

It is important to notice that the angle θ , which is a multiple of 90° , does not affect the

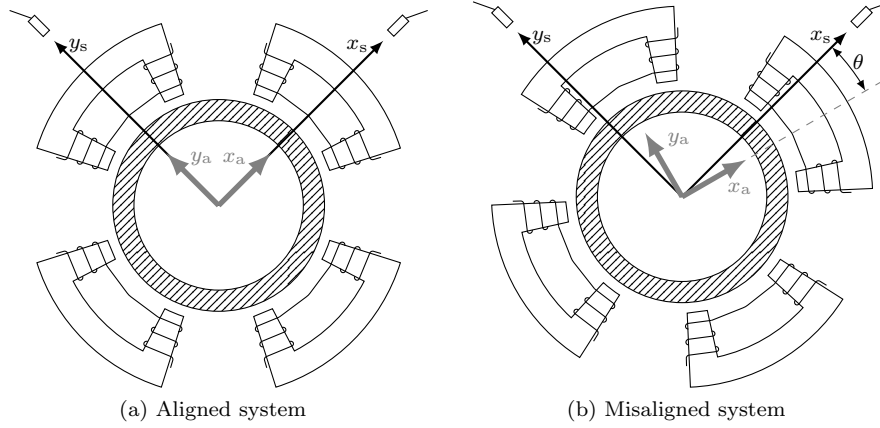


Figure 3.9. Alignment of the sensor plane and the force plane. These planes should correspond to each other, or alternatively, the coordinate transformation should be applied to obtain the working system.

cable assignment procedure. In that case, it would be just a different actuator in the same place. For heteropolar systems in general, the angle is expressed as $4 \times \chi$, where χ is from Eq. (2.7). Thus, it is necessary to search the angle of misalignment only in the range of $\pm 2 \times \chi$. In the case of a heteropolar system with four electromagnets, it is $[-\frac{\pi}{4}; \frac{\pi}{4}]$. In the cable assignment procedure, a matrix Φ_{10} was constructed. The elements of the matrix define the effect of each input on each output. In the case of misalignment, the effect of one input is distributed between two outputs. The distribution depends on the value of the angle θ . Thus, it is necessary to find such a value that maximizes the effect of one input on the specific output.

The columns in the matrix Φ_{10} represent the outputs, and therefore, it is necessary to maximize the magnitude of one value in the column. This corresponds to the infinite norm of the vector. For any arbitrary vector \mathbf{x} with a number of elements n , the infinite norm is defined as follows

$$\max(\mathbf{x}) \equiv \|\mathbf{x}\|_{\infty} \triangleq \max_i |x_i|, \quad i = 1, 2, \dots, n. \quad (3.10)$$

The objective of the optimization problem is defined as

$$\zeta = \sum_{i=1}^l \|\Theta_i\|_{\infty}. \quad (3.11)$$

The optimization is usually made to minimize the objective function, and thus, it is necessary to change the sign of the function $\zeta^* = -\zeta$. The infinite norm is always positive, and the sum of these norms is always positive; thus, the function is valid.

For each radial bearing in the system, one angle should be found. For the system with two radial bearings, two angles θ_1 and θ_2 are necessary. The measured output data

should be transformed according to these angles

$$\begin{bmatrix} x^* \\ y^* \end{bmatrix} = \mathbf{T}(\theta) \begin{bmatrix} x \\ y \end{bmatrix} = \begin{bmatrix} \cos(\theta) & -\sin(\theta) \\ \sin(\theta) & \cos(\theta) \end{bmatrix} \begin{bmatrix} x \\ y \end{bmatrix}, \quad (3.12)$$

where $\mathbf{T}(\theta)$ is the transformation matrix for the angle θ . For the system with two radial bearings, the matrix measurements \mathbf{Z}_n should be transformed in the following way

$$\mathbf{Z}_n^* = \mathbf{Z}_n \begin{bmatrix} \mathbf{T}(\theta_1) & \mathbf{0} \\ \mathbf{0} & \mathbf{T}(\theta_2) \end{bmatrix}^T. \quad (3.13)$$

The transformation is necessary as the x and y coordinates are in the \mathbf{Z}_n columns, not in rows. Hence, to keep the structure of the matrix the same, the following algebraic operation is made

$$(\mathbf{T}(\theta)\mathbf{Z}_n^T)^T = \mathbf{Z}_n\mathbf{T}^T(\theta). \quad (3.14)$$

The full equation for the matrix Φ_{io} by substituting \mathbf{Z}_n^* instead of \mathbf{Z}_n has the form

$$\Phi_{io} = (\mathbf{H}_n^T\mathbf{H}_n)^{-1}\mathbf{H}_n^T \begin{bmatrix} \mathbf{T}(\theta_1) & \mathbf{0} \\ \mathbf{0} & \mathbf{T}(\theta_2) \end{bmatrix}^T. \quad (3.15)$$

With the sin and cos functions in the transformation matrix, the problem is nonlinear and difficult to solve. Thus, it is suggested to divide it into two optimization problems at two different intervals of the angle α

$$\begin{aligned} 0 &\leq \theta \leq \frac{\pi}{4} \\ -\frac{\pi}{4} &\leq \theta \leq 0. \end{aligned} \quad (3.16)$$

At these intervals, the sin and cos functions can be accurately approximated by linear functions. The approximation is presented in Fig. 3.10. For the interval $[0, \frac{\pi}{4}]$, the transformation matrix is expressed as

$$\mathbf{T}(\theta)|_{\theta \in [0, \frac{\pi}{4}]} \approx \mathbf{I} + \begin{bmatrix} \frac{2(\sqrt{2}-2)}{\pi} & -\frac{2\sqrt{2}}{\pi} \\ \frac{2\sqrt{2}}{\pi} & \frac{2(\sqrt{2}-2)}{\pi} \end{bmatrix} \theta. \quad (3.17)$$

With the above-mentioned approximation of the transformation matrix, the optimization problem can be efficiently solved at the specific interval with the help of LMIs. LMIs can be efficiently solved with open source software and solvers (Lofberg, 2009). Finally, when the angle is found, a constant value can be calculated for the transformation matrix and substituted into the control software.

As it is possible to solve the problem only at a specific interval for each angle, a set of these problems should be solved for each combination of intervals and angles. Thus, the number of solutions is proportional to the number of radial bearings. For n radial bearings, there are 2^n problems to solve.

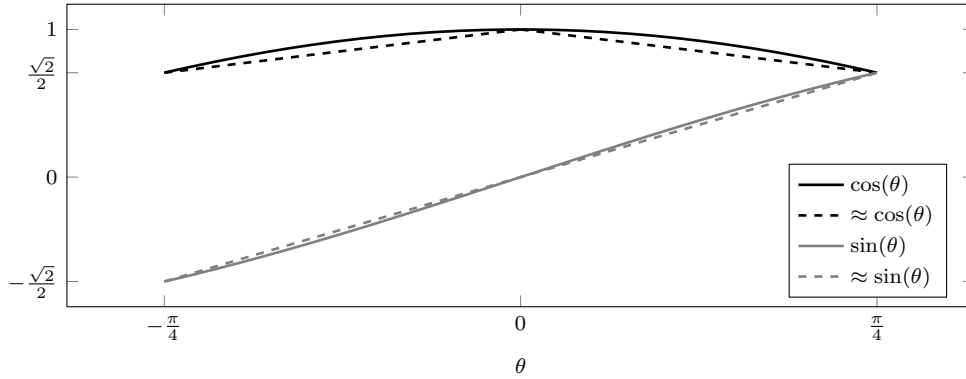


Figure 3.10. Linear approximation of the \cos and \sin functions used for the transformation. The approximation is needed in a small interval, and thus, the difference is insignificant. Without the transformation, the optimization problem is a nonlinear one.

There are seldom more than two radial AMB in a system. In addition, in larger systems, instead of four, more electromagnets (e.g. eight or sixteen) are usually used. (Shi et al., 2012) In these cases, the angle θ is reduced and there is no need to search for a solution at different intervals. In the prototype described in this work, the winding was misplaced. The details were discussed in Section 3.8 and the problem is illustrated in Fig. 3.8. In Fig. 3.11, there is a photo of the AMB with the misplaced winding. In the figure, the white rectangles indicate one electromagnet and the arrows show the actuator and sensor planes. With such a misplacement, the cable assigning procedure provides unreliable results. Thus, the described set of four LMIs were solved with the data available. Each solution provided the same value for the objective function. This is the boundary case, in which the direction of rotation does not matter. The value for the end A was 0.785 rad, that is, 45° . For the end B, the value was 8.16×10^{-16} rad, and it was treated as zero. Each solution converged in the interval from seven to nine steps with the mean time of 1.14 s.

With the angles achieved, the force vector was transformed in software to correspond to the actual position of the electromagnets. Tests with the system were continued until the next disassembling for changing the rotor. At that point, the AMB was turned in the correct position.

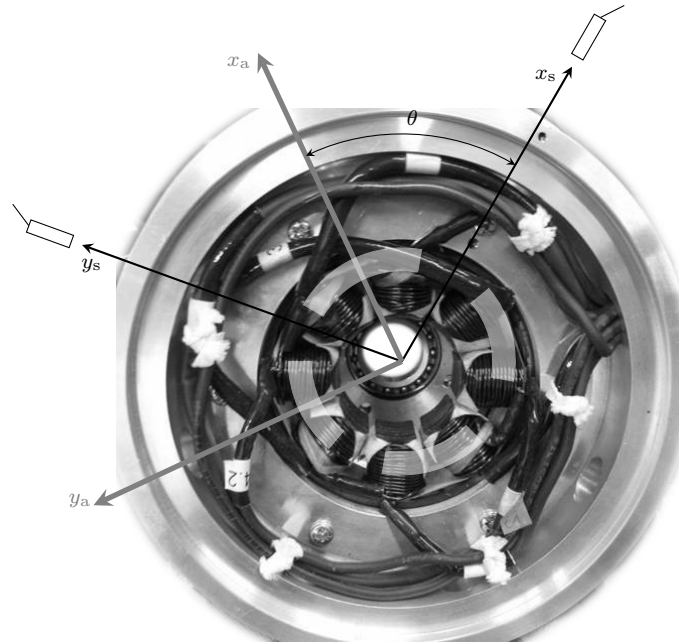


Figure 3.11. Photo of one bearing of the prototype with a misplaced winding. The coils are wound in pairs to provide a horseshoe electromagnet. During the manufacturing process, the correspondence between the electromagnets and the sensors was violated.

3.4 Conclusions

In this chapter, the commissioning process of an AMB system was addressed. The general guidelines for all steps were given and the initial phase was discussed in detail. The initial phase covers the steps that can be carried out in the open loop. This includes tuning of the sensors and the actuators.

The first problem was the determination of the geometric center for each bearing. The problem also covers the determination of the safety operation region. The proposed solution was expressed in the form of an optimization problem. The problem was solved efficiently by an LMIs approach.

The next challenge in the initial commissioning was the correct assignment of the cables. The suggested approach is to use a regression analysis with a specific design of experiments. This way, by applying knowledge on the bearing geometry and dynamics,

the number of measurements can be reduced.

The last problem was to align the actuator and sensor planes. The method applied aims at an optimal combination of angles. The optimization was made by the LMIs by using the input data from the previous problem. This provides an efficient solution.

All these methods can be combined and carried out with one set of measurements. In fact, to solve the above-described problems, the same input data are required. Thus, it is natural to combine them into a single procedure, which provides help during the commissioning process but also serves as a diagnostic tool.

Chapter 4

System Identification

With the steps described in the previous sections, a system that is ready to operate in the closed loop was obtained. In this chapter, the next step is to tune the parameters by identification techniques. To obtain a model that can be used directly to the controller synthesis, a linear gray-box model is identified. Further, the choice of parameters is discussed and their effect on the final model is assessed. The experimentally obtained model is compared with the analytical one. As a result, a model suitable for the controller synthesis is estimated.

System identification is the process of developing or improving the mathematical representation of a physical system by using experimental data. The process is usually carried out by statistical methods, and to increase the accuracy, a special design of experiments can be used.

Models that are identified can be divided based on the a priori knowledge (Ljung, 1999):

1. Black box model – no a priori knowledge available, the parameters are adjusted to fit the data without any relations to the physical nature of the object.
2. Gray-box model – the model is obtained by applying physical laws, but still, some information is missing. The parameters are fitted to reflect the physical processes in the object.

In this work, the focus is on the controller synthesis. This requires an accurate linear

model, and thus, only gray-box models are discussed.

4.1 Parametric identification of a linear model

It was discussed above that a controller synthesis procedure requires a linear state-space model as an initial point. The general model can be obtained based on physical laws, as it was demonstrated in Chapter 2. However, in an actual system, the parameters may vary compared with the analytical prediction. To specify these parameters, system identification methods should be applied.

The parameters for a gray-box model can be obtained both in the frequency domain and in the time domain. The frequency domain method provides a very good signal to noise ratio, and thus, accurate estimates of the parameters. On the other hand, the method is quite time consuming. The method requires to excite the system at each desired frequency, to measure the response, and to extract the necessary data. Alternatively, a multisine excitation method can be used (Hynynen, 2011). However, the frequency domain approach is limited in the case of nonlinear models.

An alternative to the frequency domain is a time domain method. The method uses the original model and fits it directly to the measurements available. Thus, the method can provide fast results. As a drawback, the noise to signal ratio is not that good.

Each model is presented in a state-space form based on the physical laws. The unknown parameters in the state-space gray model can be fitted with the least square estimator (LSE) or the maximum likelihood estimator (MLE). According to (Ljung, 1999, Chapter 7.4), the estimator maximizes the probability that the measured data fits the model. Mathematically, the measured data y^N for the set of parameters θ should take the value with the probability proportional to the following probability density function

$$f_y(\theta; y^N). \quad (4.1)$$

The estimate of the parameters $\hat{\theta}$ for the MLE is then given as

$$\hat{\theta}_{\text{MLE}}(y^N) = \arg \max_{\theta} f_y(\theta; y^N). \quad (4.2)$$

The LSE is a well-known method that minimizes the sum of squared residuals from the measurements and the model (Ljung, 1999, Section 7.3) As the identified models are linear gray-box models, and frequency domain data are used, the iterative LSE is applied to the routines.

These algorithms are widely adopted, and in practical applications, their implementation in Ljung (2011) is used.

4.1.1 Parametric frequency domain identification

Radial AMBs are identified in the frequency domain. As mentioned above, the method is applicable to the linear system and provides a good signal to noise ratio. The system is identified in several steps according to the diagram presented in Fig. 1.3. First, the system is identified at a standstill, and then at a speed that corresponds to the operating point. The results for the identification are obtained for the system supported by the magnetic bearings and by a step-sine method. To support a rotor, an linear quadratic Gaussian (LQG) controller synthesized for the rigid body model is applied. That way, the damping of flexible modes is not affected by the controller.

The identification at a standstill is performed to estimate the parameters that are independent of the rotational speed. These are the main characteristics of AMBs: the current (k_i) and position (k_x) stiffness. The stiffness for each electromagnet may vary. The main variation source is the runout because of the manufacturing tolerances. When rotating, these variations are evenly distributed between the electromagnets of one bearing, and thus, it is suggested to assume that the values of stiffness are similar for all electromagnets at one bearing. The other parameter of interest is the bandwidth of the actuator. The actuator is roughly approximated as Eq. (2.17), and identification helps to validate the value given by Eq. (2.18). The above-mentioned parameters affect the general behavior of the system in the full frequency range. Furthermore, some parameters of the rotor can be clearly seen from the identification results. Such parameters are the flexible modes. The main interest is in the first flexible mode as the others have too high a frequency. The flexible mode corresponds to a pole zero pair and can be seen in the frequency response only in a short frequency interval. As it is shown in Fig. 4.1, the first flexible mode appears around $1 \times 10^4 \text{ rad s}^{-1}$, and it is characterized by a significant shift in phase and by magnitude variation. The two main characteristics of the flexible mode are frequency and damping. The frequency for the initial model is obtained from the FEM, and the damping factor is assumed to be 0.02. (Cremer et al., 2005) Typically, these parameters are validated by an EMA, but they can change in the final assembly. In the assembled machine, the identification routine helps to tune these parameters. It is especially helpful as cases have been reported where the natural frequencies of the rotor have shifted after some time. (Li, 2007)

At a standstill, the x and y directions of the rotor are not coupled. The rotor itself is axisymmetric. Thus, for the identification of a flexible mode, only one axis can be chosen. Consequently, the model is reduced from a 4-by-4 multi-input multi-output (MIMO) model to a 2-by-2 MIMO one. The rotor is modeled as a point mass with an additional coordinate transformation for inputs and outputs. This way, the system can be reduced further to the single-input single-output (SISO) case. An important point worth remembering is that the flexible mode of interest should be possible to be excited and measured in the chosen direction. For the excitation, the modal shape node should not be located in the actuator position. For the measurement, the modal shape node should not be located in the sensor position. To obtain the data for the identification procedure, the system is excited with a step-sine signal. The excitation

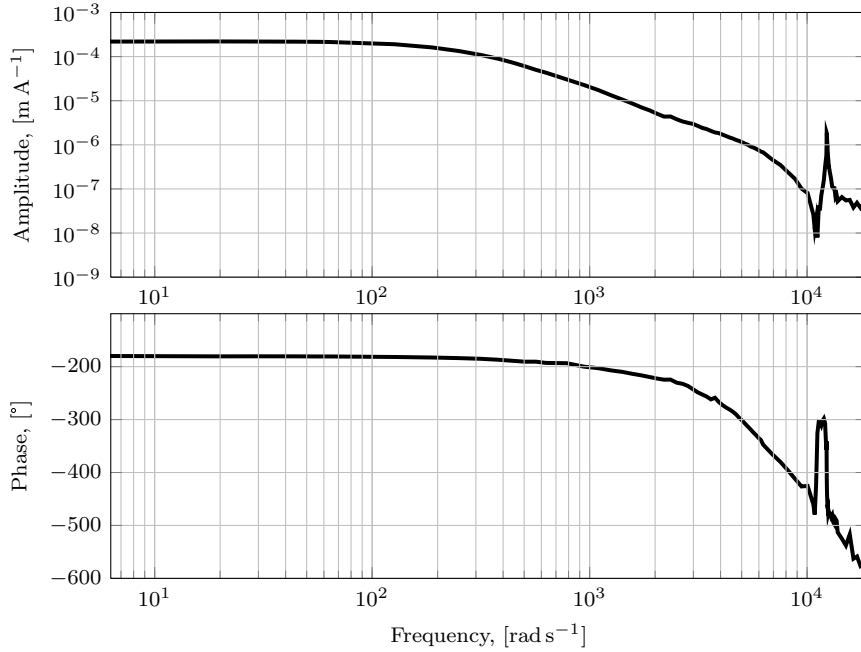


Figure 4.1. Measured bode diagram of the first rotor in the x direction at the end A. The first flexible mode is clearly seen. In addition, a significant shift in phase especially at higher frequencies indicates a time delay.

is carried out with AMBs and measured with the sensors available in the AMBs. Thus, no external hardware is used. The excitation signal is inserted in the control current, and the position of the rotor is measured. This way, an open-loop characteristic is obtained. The system is excited separately from each direction. The initial set of excitation frequencies are presented in Table 4.1. To achieve a better resolution around specific points (frequencies of flexible modes), a denser grid was used. The identification is performed for the linear model, and to get accurate results, the system should be excited in the linear region. This is verified by a harmonics analysis. There should be no subharmonics of the excitation frequency for the linear system. The excitation amplitude is varied with the frequency to keep the system in the linear

Table 4.1. Initial excitation frequencies used for the identification routine.

Frequency range, Hz	Step between points, Hz	Excitation amplitude, mA
1 – 10	2	300
10 – 100	10	300
100 – 1000	25	900
1000 – 3000	100	1200

region and to compensate the decline in the actuator bandwidth. The values of the amplitude are presented in Table 4.1.

The system is excited at each frequency and all outputs are measured. The sampling time is $100\ \mu\text{s}$, and thus, the Nyquist frequency is 5 kHz. The measurements are made up to 3 kHz, as above this the results are out of interest for the synthesization of the controller. For each input and output signal, a discrete Fourier transformation (DFT) is made, and then relation of the output signal to the input is found for the excitation frequency. For the SISO system, a full set of these points represent the frequency response function (FRF). In the case of a MIMO system, the FRF is obtained as follows

$$\hat{\mathbf{G}}(j\omega_k) = \mathbf{Y}(\omega_k)\mathbf{U}^{-1}(\omega_k), \quad (4.3)$$

where j is an imaginary unit, ω_k is the k th excitation frequency, \mathbf{Y} is the matrix of outputs, and \mathbf{U} is the matrix of inputs. Each row in the matrix corresponds to the particular input and output, respectively. The columns represent separate experiments. Thus, the value of the DFT on the m th row and the n th column in the output matrix ($U_{m, n}$) corresponds to the m th output of the n th experiment.

The value for the actuator bandwidth can be estimated from the same measured data. The currents are usually available for the inner current control loop. Thus, the desired value can be estimated from the specific FRF from the input current to the measured one. Thus, a higher accuracy is achieved. The other solution is to include the bandwidth as an estimation parameter in the model with stiffness. This results in a less accurate estimation. In this work, the first method is applied. As it was discussed above, the system may operate with two different rotors and with an impeller as a useful load. It is important to identify each rotor separately with and without the impeller as the dynamics of the system changes significantly with the load. The load itself can be changed to a different one, which is one reason for the retuning of the system. The results of an iterative identification for the system at a standstill are presented in Fig. 4.2. Only the results on one axis are presented as the rotor is axisymmetric, and there is no coupling between x and y at a zero speed. It can be seen that with each iteration, the fitting accuracy is increased. The last iteration provides a relatively small improvement when compared with the full FRF range. The iteration fits the flexible mode, which affects only a small frequency range of approximately a quarter of a decade in the logarithmic scale.

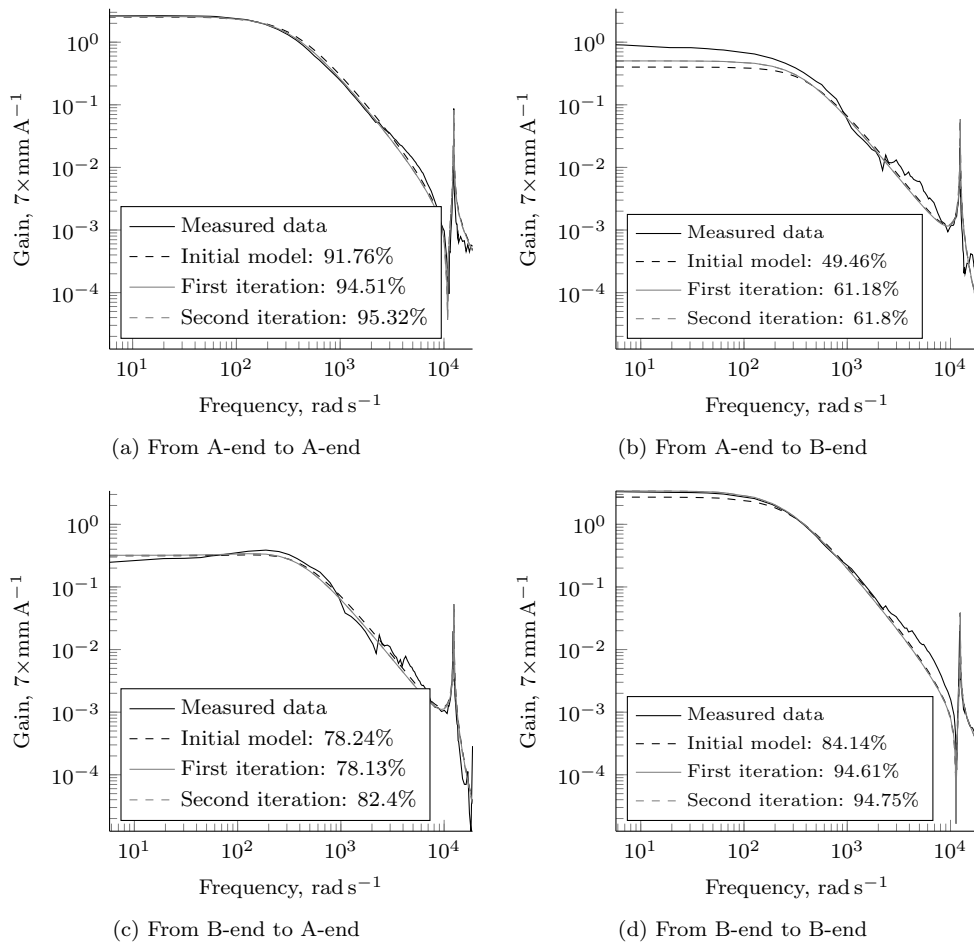


Figure 4.2. Iterative identification of the model parameters for the first rotor at a standstill. At the first step, the general slope of the response is fitted with k_i and k_x . Next, the parameters describing the flexible mode are fitted.

The combined results and numerical values for the flexible rotor are presented in Table 4.2. The values are identified with a sufficient accuracy based on the standard deviation value. The frequency of the flexible mode is well predicted by FEM, although the damping is five times as high compared with the initial value. We can see that the identified values of stiffness are about 20 % lower than the modeled ones. If this difference is translated into the difference in the air gap, according to Eqs. (2.13) and (2.14), it is 35 μm or about 7 % of the nominal air gap. The difference is mostly due to the manufacturing tolerances and the rotor runout.

In the identification process, an increase in the frequency phase lag is spotted in the FRFs. Such behavior is typical for the system with input and/or output delays. Such delays are common for digital systems when data are digitally transferred to the actuators from the controller. The reason is the time required for the digital-to-analog and analog-to-digital conversions and the actual transfer of data. From the phase lag, the delay is estimated to be 300 μs , which corresponds to three sampling steps. For the identification, the delay can be either included in the model or subtracted from the measured data. The known time delay still allows to identify the parameters of the linear system (Orlov et al., 2002) and can be removed (Ljung, 1999).

In Chapter 4 on identification, the delay is excluded from the measured data and introduced in the model later in Chapter 5 on control. Based on the identified data, the FEM model of the rotor can be updated and validated; in addition, a new controller can be synthesized, if necessary. The next step is to collect the data from the rotating system. When rotating, the system is affected by the gyroscopic effect, and therefore, the coupling between the x and y directions is presented. The magnitude of the coupling is defined by the rotational speed and I_p . The polar moment of inertia is equivalent to the I_z defined in Eq. (2.23). The moment of inertia provides coupling in the full frequency range. However, there is an additional coupling from the flexible mode. It results in the splitting of the mode frequency. The FRFs of the modeled and measured system with the splitting of the flexible mode frequency is presented in Fig. 4.3. The gyroscopic effect is not that significant for the rotor without a wheel, and hence, the splitting is not significant either.

To identify the polar moment of inertia, the FRF is measured at the rotational speed of 22 000 rpm. The speed is approximately half of the nominal speed of 45 000 rpm and is enough to capture the interaction between the x and y axes. From these data, the polar moment of inertia is identified with the same identification routine. The values for the second rotor are presented in Table C.1. The identified value for I_p is 20 % more than the initial one. The standard deviation is relatively small, and thus, it can be concluded that the parameter is identified accurately. The same identification routine is carried for the rotors with an impeller as a load. The impeller has a relatively large diameter compared with the other parts of the rotor. Thus, it introduces a visible gyroscopic effect. Besides the gyroscopic effect, the frequency of the first bending mode becomes significantly lower; see Table 2.1. Under these conditions, the splitting of the flexible modes is distinguished already at 10 000 rpm. It gives an opportunity to verify the gyroscopic part of the flexible mode obtained by the FEM.

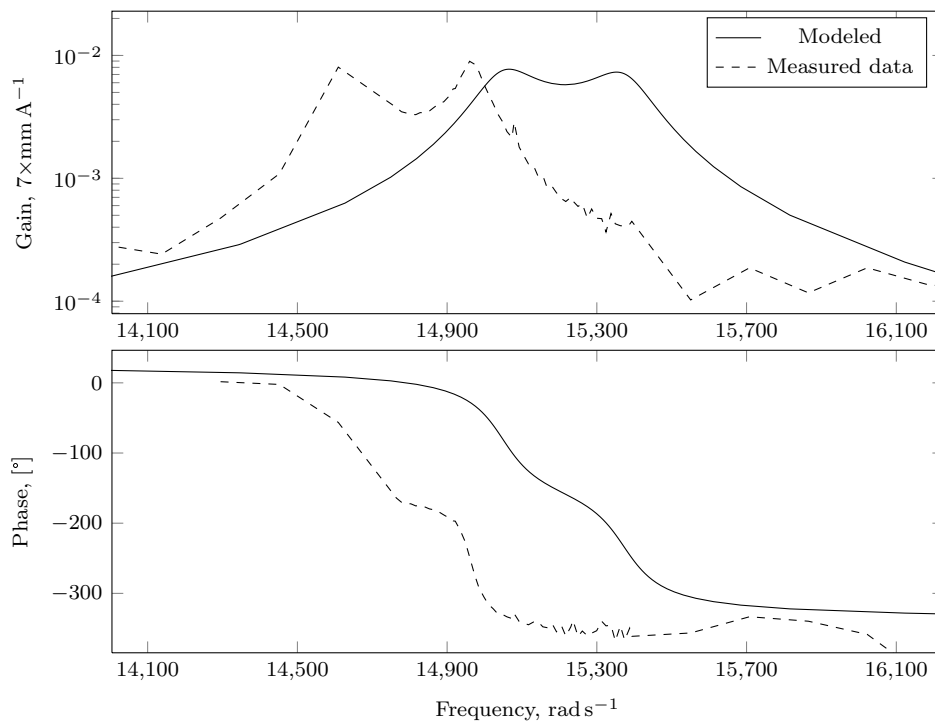


Figure 4.3. Frequency response of the second rotor at 22000 rpm, from the A-end x input to the A-end x output. The presented model is identified at a standstill, and the corresponding parameters are updated. The splitting of the flexible mode caused by the gyroscopic effect is demonstrated. In addition, a small shift in the frequency of the flexible mode can be seen.

Table 4.2. Results of parametric identification for the flexible mode for the first rotor.

Parameter		Initial value	Identified value	Standard deviation
Current stiffness	A-end,	21.863	17.218	0.51931
[A m ⁻¹]				
Position stiffness	A-end,	110310	79779	222.35
[N m ⁻¹]				
Current stiffness	B-end,	21.863	18.536	0.63217
[A m ⁻¹]				
Position stiffness	B-end,	110310	83796	6285.1
[N m ⁻¹]				
Actuator bandwidth,		7324.1	8372.9	995.14
[rad s ⁻¹]				
Flexible mode frequency,		12431	12290	608.96
[rad s ⁻¹]				
Flexible mode damping ratio		0.002	0.010681	5.6955e-5

The same set of frequency measurements are obtained for the second rotor with an impeller at a standstill and at 22 000 rpm. The measurements at a high speed are made only for the second rotor. The first rotor has a significant runout on the sensor surfaces (see Fig. 3.6 and the related comments in Section 3.2), which leads to results with too much noise at high speeds. By following the described procedure, the initial set of parameters is obtained and presented in Table C.2. The standstill results show already with the rotor without a load. Now, the current and position stiffness at the ends A and B are different. The stiffness at the end A is slightly lower. Damping for the flexible mode is greater, and also for the rotating system, the polar moment of inertia is slightly higher than estimated. These effects are explained by the complex nature of the impeller. It has a sophisticated geometry compared with the other parts of the rotor, and it is therefore difficult to model. The simplest parameter weight is easy to take into account. The difficulties appear when modeling transversal inertia and rotational inertia.

Transversal inertia appears in the mass matrix of the system as in Eq. (2.23). If it is incorrectly estimated in the model, the only way for the identification procedure to compensate it is to increase the stiffness. This can be seen from Eq. (2.24). As the inertia is not identified in the identification routine, the algorithm fits the measured signal by changing the values of stiffness. In the case of a rotor with quite a simple geometry, these differences are close to the noise level, and are thus neglected. With the impeller, these differences can be distinguished, which is demonstrated by the results. The best solution is to update the model of the impeller. The drawback is that it takes time and additional tools. The other option is to use the values provided by the identification routine as they compensate the differences in inertia by the changes in stiffness. Modeling of a rotational moment of inertia is also challenging for a complex

geometry. In addition, the measurements were carried out in an open environment, and the impeller was pumping air in standard conditions.¹ The air flow in the housing provides additional forces on the impeller, such as cross-coupled forces (Ertas and Vance, 2007; Mushi et al., 2008, 2012). These forces are not taken into account in the model, and thus, they can contribute to the rotational moment of inertia. The effect of the impeller on the flexible mode was already mentioned. In addition to the lower frequency of the flexible mode, increased damping is spotted. There can be various explanations to this. First, the impeller has blades with their own natural frequencies, and energy can dissipate through these blades. Another possible reason is the connection between the rotor and the impeller. The impeller is screwed, and such a connection may not correspond to the FEM model that assumes linear elasticity of materials.

Taking into account these problems, some of the parameters should be identified separately in the operating point. Therefore, the frequency of the flexible mode and damping are identified for the system at 22 000 rpm. There is a small shift in frequency from $7792.9 \text{ rad s}^{-1}$ at a standstill to $7915.1 \text{ rad s}^{-1}$ while rotating. The damping factor is estimated to be 0.05, which is closer to the original result from the FEM and the measurements of the rotor only. In addition, the modal inertia of the flexible mode is identified. That inertia is responsible for the splitting of the flexible modes, and could not be clearly seen with the previous setups.

The differences between the original model obtained at a standstill and interpolated to the 22 000 rpm and the measured data are presented in Fig. 4.4. In the figure, also the model with the tuned parameters is presented. It is evident that in the original model the damping was overestimated and the actual value is lower. The frequency of the flexible mode is almost the same in both cases, and the difference is around 1%. The gyroscopic effect is more significant for the flexible mode than it was predicted, and 2.2 times as high as in the original model. That parameter is responsible for the splitting of the flexible mode, which is clearly seen in Fig. 4.4. In general, we may conclude that an additional tuning of the identified parameters is necessary for the particular operating point. It increases the model accuracy and helps to overcome the difficulties in extrapolating the model from the experiments at a standstill. The largest differences between the modeled system and the measured data are spotted in the gyroscopic effect, the moments of inertia, and damping of the flexible mode. The last parameter is identified quite accurately for the rotor itself, but with an impeller, the results for low and high rotational speeds are slightly different.

It should be noted that the system is designed for subcritical applications. Even the first flexible mode can be accurately observed as it is still in the high frequency region. Thus, the parameters of the flexible mode can be used mainly for modelling purposes. The mode cannot be affected or excited by the controller with a bandwidth that is significantly lower than the frequency of the mode. Thus, inaccurate values for damping and the modal moment of inertia do not affect the controller synthesis.

¹Standard conditions refer to standard ambient conditions. The temperature is 298.15 K and the absolute pressure is 100 kPa.

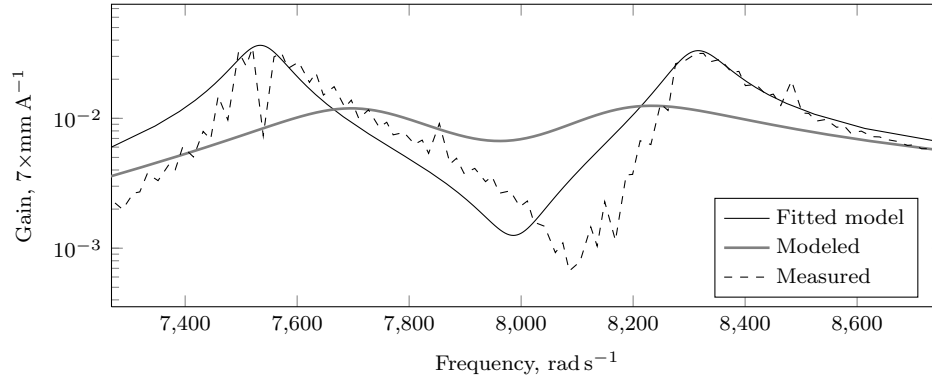


Figure 4.4. Frequency response of the second rotor with an impeller at 22 000 rpm, from the A-end x input to the A-end x output. The impeller significantly increases the gyroscopic effect. The identification routine allows to identify the gyroscopic matrix and fit the model to the measured data.

In the work of Li (2007), the author examines different parameters of an AMB system and their effect on the stability with a ν -gap metric approach. Li (2007) shows that the uncertainty of the moments of inertia that are compensated by differences in stiffness are tolerated well by the feedback control. In that sense, the controller can still be synthesized without updating the model of the rotor. In the same work by Li (2007), the gyroscopic effect is stated as the one that requires accurate modeling. The reason is that the feedback control is very sensitive to the uncertainty in that parameter. Thus, accurate identification in the operating point is necessary, as it was mentioned above. To conclude the discussion on the identification results, it should be noted that in this work, the main idea of identification is to specify the parameters of the system for the controller synthesis. The controller deals with a linear system in a limited frequency range. The frequency range is mostly dictated by the actuator bandwidth. Thus, the most interesting parameters for the identification are the current and position stiffness, the actuator bandwidth, and the gyroscopic effect. The rest of the parameters are necessary to validate the model and can also serve for diagnostics purposes.

A stepped sine identification is quite time consuming. An alternative is a multisine excitation, which was investigated in relation to AMBs by Hynynen (2011). The main benefit of the stepped sine approach is the signal to noise ratio. In addition, it is the widely used approach with a straightforward implementation, and it is relatively easy to apprehend. The drawback with the number of measurements can be alleviated by applying the knowledge on parameters that are necessary to identify.

Table 4.3 presents a set of parameters discussed in this work. Along with each parameter, the frequency range and the number of required inputs and outputs are provided. Thus, to identify the stiffness values, the full frequency range and all inputs and outputs are required. On the other hand, to identify the parameters of the flexible

mode, quite a dense but narrow frequency grid is necessary, and one input with one output is sufficient for that. Taking into account that the model for the controller is necessary, the identification procedure can be summed up for subcritical applications as follows:

1. All inputs with all outputs with a sparse frequency grid at a standstill have to be determined.
2. The inputs and outputs in the x and y directions at one end close to the operating point with a sparse frequency grid have to be identified.

The first step allows to specify the stiffness values and the actuator bandwidth. As these parameters affect the full frequency range, a sparse grid can be used. The second step allows to tune the gyroscopic effect, which also affects the full frequency range. The gyroscopic effect appears as an interaction between the rotor x and y planes, and thus, two inputs and outputs suffice.

The possibility to achieve identification results is limited in the frequency range from the top by the Nyquist-Shannon sampling theorem. This limit is half of the sampling frequency. On the other hand, from the control perspective, the high frequency dynamics above the bandwidth of the controller is rarely taken into account and damped to avoid noise propagation problems. Thus, based on the application and specified requirements, the measured response can be limited to the frequency between the controller bandwidth and half of the sampling frequency.

4.2 Conclusions

In this chapter, the AMB system was identified. The identification was carried out in the frequency domain using step-sine excitation signals. An approach of this kind provides a good signal to noise ratio. To obtain accurate results, a dense frequency grid is required. However, as a result, the time and number of measurements required are

Table 4.3. Steps of the identification procedure.

Step	System part	Parameters	Frequency range	Model order
1	Delay	τ_d	Full	1-by-1
2	Power amplifier	w_{bw}	Full	1-by-1
3	Actuator circuit	k_x and k_i	Full	4-by-4
4	Rotor	ω, ξ	Narrow	1-by-1
5	Rotor	I_p	Full	2-by-2
6	Rotor	I_{fl}	Narrow	1-by-1

increased. Therefore, the behavior of the system was analyzed in different frequency ranges, and guidelines were provided on which regions require more attention.

The main idea for the identification is to obtain a more accurate model for the controller synthesis, thereby reducing the difference between the actual plant and the modeled one. To provide a model suitable for the controller, parametric identification was adopted. A set of parameters were chosen, and their effect on the specific frequency ranges was described. Finally, an iterative approach to specify the parameters was taken.

It was shown that with an iterative approach, the parameters can be fitted accurately and only to the frequency region that is affected by the parameter in question. That way, it is possible to avoid a situation where unphysical fitting of parameters takes place. This was demonstrated with the fitting of the flexible mode parameters. When a full frequency range was used, these parameters were fitted incorrectly; actually, the identification routine tuned the low-frequency behavior instead.

The flexible modes for the examined rotors have too high a frequency and can be neglected for the controller synthesis. In this work, the states corresponding to the flexible modes are removed from the linear system. The other opportunities are to approximate the modes with an additive high-frequency uncertainty or to use model reduction techniques. For these cases, special identification routines can be implemented (Lu et al., 2008).

An iterative identification method demonstrated its validity, and as a final result, a model suitable for the controller synthesis was obtained.

Chapter 5

Control of an AMB System

In this chapter, the theoretical background is given on the applied robust control techniques. The inclusion of an uncertain set is justified. Some techniques for switching between controllers during operation are presented. The model of the system from a common linear time invariant (LTI) to a LPV form is converted. The objectives of the loop-shaping techniques are discussed and their transformation to particular transfer functions is provided. Controllers are evaluated and their performance with an analytical model and an actual setup is demonstrated.

In Chapter 2, it was shown that AMBs are open-loop unstable. To make the system stable, a control law is required. Control theory, according to the definition, deals with the behavior of dynamical systems as an interdisciplinary branch of engineering and mathematics. The discussed AMBs present a challenging topic for the control theory. The system is nonlinear with a variation of parameters and different kinds of disturbances. There are more than one input and output correlated with each other, which makes it a MIMO system.

It is enough to implement a simple PID regulator to stabilize the system. It is a well-known and widely used industry solution (Knospe, 2006). The drawback of simplicity is the relatively poor performance and robustness. To make the system stable at each rotational speed from zero to nominal, a set of PIDs are usually used. The particular controller from the set is chosen based on the current speed. This makes the controller synthesis an ad-hoc solution without formal proof for the stability in intermediate phases. A lot of simulations under different conditions are required to validate the stability.

5.1 Model-based control approaches

The evolution of control theory has provided the modern tools to synthesize controllers with different properties. The synthesis is carried out based on the plant dynamics. Additional knowledge on how the control signal propagates through the plant allows building of more robust controllers with a better performance. As a side effect, these modern controllers tend to have quite a high order, usually comparable with or higher than the order of the plant. Additionally, they can no longer be hand-tuned just by changing several gains.

The model-based controllers require full information about the states of the plant. However, only a few outputs are available for measurement. Thus, an estimate of the unmeasured states is required. The estimate is provided by the observer, which is based on the same inputs as the plant, and the latest measurements available provide the full set of states for the controller; Fig. 5.1. Hence, the term 'controller' usually refers to a combination of the controller itself (\mathbf{K}_k) and the state observer (\mathbf{O}). In this work, the vector \mathbf{r} denotes the reference signal, and \mathbf{x} is the state vector of the linear plant model (\mathbf{G}). The modern control theory usually treats the problem of controller synthesis already with an observer. Thus, the discussed model-based controllers can be divided into a deterministic controller and a state estimator.

One popular model-based approach for the controller synthesis is an LQG controller. It consists of an linear quadratic regulator (LQR) and a Kalman filter as an optimal state estimator. A controller of this kind has received significant attention; however, the main problem is that there are no guaranteed stability margins Doyle (1978). The controllers to an AMB system is discussed in by Jastrzebski (2007).

As a solution to the robustness properties, an \mathcal{H}_∞ control approach is evaluated. It provides the guaranteed stability margins.

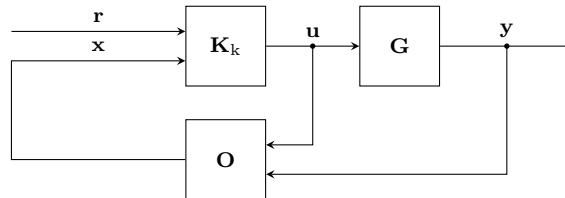


Figure 5.1. Control configuration with a state observer. The state feedback controller needs all the states of the system to operate. All states are not always available for measurements, and thus, an estimator is used. The estimator based on the controller signal and measurements available estimates the current state of the system.

5.1.1 Generalization of the control problem

To discuss the controller synthesis techniques further, it is necessary to provide a general framework. It is assumed that the plant \mathbf{P} has the control inputs \mathbf{u} , the measured outputs \mathbf{y} , the exogenous inputs \mathbf{w} , and the exogenous outputs \mathbf{z} . The first pair of inputs and outputs is used as the controller outputs and inputs, respectively. These are the only signals that are available for the controller in its operating conditions. These relations are described in Fig. 5.2. The second exogenous pair can be any arbitrary input and output. They are used to provide objectives for the signals to be minimized to achieve the desired properties of the control system. The minimization is achieved with a specific mathematical framework. A framework already mentioned in relation to the Kalman filter is the mean square approach. In general, the approach is referred to as the \mathcal{H}_2 synthesis (Zhou and Doyle, 1998). Zhou and Doyle (1998) define the approach as follows definition:

The \mathcal{H}_2 control problem is to find a proper, real rational controller \mathbf{K} that stabilizes \mathbf{G} internally and minimizes the \mathcal{H}_2 norm of the transfer matrix \mathbf{T}_{zw} from \mathbf{w} to \mathbf{z} .

Another approach that was mentioned above and will be applied to the AMB system is the \mathcal{H}_∞ synthesis. Here, the infinite norm of exogenous inputs and outputs is minimized. The main benefit is the ability to have definite stability margins. The definition by the same authors (Zhou and Doyle, 1998) is given as follows

Suboptimal \mathcal{H}_∞ control problem: Given $\gamma > 0$ find all admissible controllers $\mathbf{K}(s)$, if there are any, such that $\mathbf{T}_{zw} < \gamma$."

5.1.2 Uncertainty description

The importance of the correct uncertainty description cannot be underestimated for the control systems. The uncertainty comes from the limited availability of exact

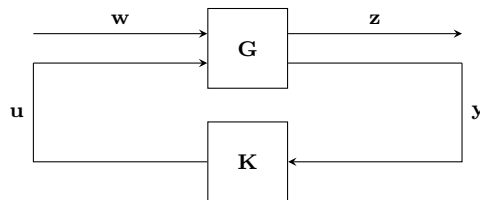


Figure 5.2. Generalized control problem. The initial model of the system (\mathbf{G}) is altered with additional inputs \mathbf{w} and outputs \mathbf{z} . These inputs can be additionally weighted to specify the objectives. The obtained system is used for the controller synthesis.

measurements of parameters. There is always some unpredictable variation in the manufacturing process or as a result of external effects not taken into account in the model. Another reason for using uncertainty is the limited theory for nonlinear systems. Thus, a nonlinear model is usually linearized around some operating point. The linearization assumes some parameters to be fixed, although they can change. To keep the model simple and linear, these parameters can be presented as uncertain ones. In general, the difference between the actual system and the obtained model is described by the uncertainty.

Uncertainties in control theory are usually divided into structured uncertainty and unstructured one (Zhou and Doyle, 1998). Unstructured uncertainty is used to describe the unknown behavior of the model. This refers to some missing dynamics, which is usually related to high frequencies (Skogestad and Postlethwaite, 2005). In the discussed AMB system, this uncertainty can cover the unmodeled high-frequency modes of the rotor and/or sensor noise.

The unstructured uncertainty appears in an additive or multiplicative form as it is demonstrated in Fig. 5.3. Yet another form is a coprime, discussed in more detail in Section 5.1.4. The structured uncertainty describes the variation in the parameters of the model. This is usually related to the lower frequency range. For a particular parameter, its variation bounds are provided and the model is examined with respect to these bounds. A method used in this work is an inclusion of the rotational speed of the rotor as the uncertain parameter.

The structured uncertainty can also be presented with a Δ structure. Each parameter is expressed with its nominal value and an uncertain set. Thus, an arbitrary parameter m with a nominal value of m_0 and a variation of 20% is written as $m = m_0 \pm m_1 m_0 = 0.2m_0$. Inserting an uncertainty $\delta \in [-1, 1]$, the parameter can be expressed as $m = m_0(1 + m_1\delta) = m_0(1 + 0.2\delta)$. Assuming that it is a parameter of a linear system and by adding the input and output related as $w = \delta z$, the uncertainty can be solved. The described procedure is demonstrated in Fig. 5.4. In the same manner, all structured uncertainties are obtained, and the state-space matrices of the system are expressed as $\mathbf{A} = \mathbf{A}_0 + \delta\mathbf{A}_1$, $\mathbf{B} = \mathbf{B}_0 + \delta\mathbf{B}_1$, $\mathbf{C} = \mathbf{C}_0 + \delta\mathbf{C}_1$, and $\mathbf{D} = \mathbf{D}_0 + \delta\mathbf{D}_1$. The part that linearly depends on the uncertain parameters and their factorization is

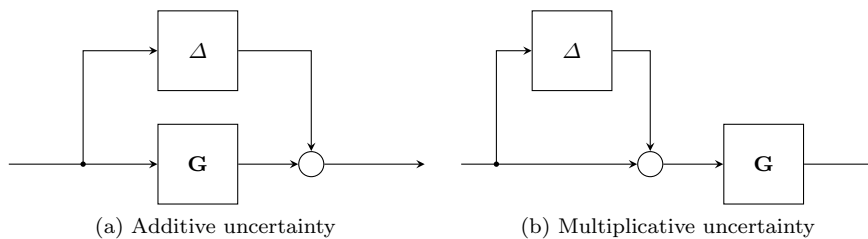


Figure 5.3. Types of unstructured uncertainty. Two common types of uncertainties that can be included in the generalized control problem.

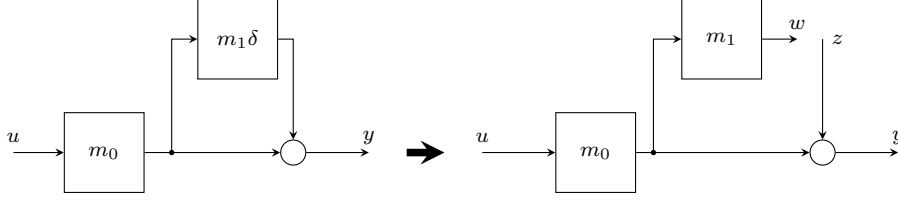


Figure 5.4. Structured uncertainty. The structured uncertainty is included in the generalized control problem by additional inputs and outputs. These additions are made by removing the normalized uncertain part δ .

written as follows

$$\begin{bmatrix} \mathbf{A}_1 & \mathbf{B}_1 \\ \mathbf{C}_1 & \mathbf{D}_1 \end{bmatrix} = \mathbf{U} \boldsymbol{\Sigma} \mathbf{V}^T. \quad (5.1)$$

The columns of \mathbf{U} and rows of $\boldsymbol{\Sigma} \mathbf{V}^T$ that correspond to the nonzero elements of the singular value matrix $\boldsymbol{\Sigma}$ can be partitioned. Finally, the augmented system with additional inputs and outputs for uncertainty is written as

$$\begin{bmatrix} \dot{\mathbf{x}} \\ \mathbf{y} \\ \mathbf{z} \end{bmatrix} = \begin{bmatrix} \mathbf{A}_0 & \mathbf{B}_0 & \mathbf{U}_1 \\ \mathbf{C}_0 & \mathbf{D}_0 & \mathbf{U}_2 \\ \mathbf{V}_1 & \mathbf{V}_2 & \mathbf{0} \end{bmatrix} \begin{bmatrix} \mathbf{x} \\ \mathbf{u} \\ \mathbf{w} \end{bmatrix}. \quad (5.2)$$

The uncertain part of the system written as $w = \Delta z = \begin{bmatrix} \delta_1 & & 0 \\ & \ddots & \\ 0 & & \end{bmatrix} z$ has a diagonal structure. It is important to minimize the number of elements in the matrix if there are several occurrences of the same uncertainty. It is done by finding a factorization (see Eq. (5.1)) with a full rank.

5.1.3 Inclusion of an uncertainty set

An uncertainty set can be included as an additional perturbation block. The infinite norm of that block is not greater than one. Under such conditions, if there is a controller, it guarantees the stability. Now, the generalized control problem has the form demonstrated in Fig. 5.5. A full transfer function from the structure in Fig. 5.5 can be obtained with a lower or upper Linear Fractional Transformation (LFT) that defines the following operations

$$\mathcal{F}_l(\mathbf{P}, \mathbf{K}) = \mathbf{P}_{11} + \mathbf{P}_{12} \mathbf{K} (\mathbf{I} - \mathbf{P}_{22} \mathbf{K})^{-1} \mathbf{P}_{21} \quad (5.3)$$

$$\mathcal{F}_u(\mathbf{P}, \boldsymbol{\Delta}) = \mathbf{P}_{22} + \mathbf{P}_{21} \boldsymbol{\Delta} (\mathbf{I} - \mathbf{P}_{11} \boldsymbol{\Delta})^{-1} \mathbf{P}_{12} \quad (5.4)$$

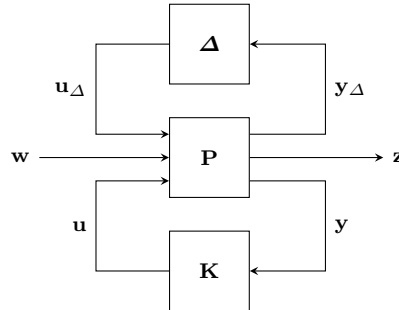


Figure 5.5. Generalized control problem with uncertainty. In this case, the inputs and outputs for uncertainties are separated from \mathbf{w} and \mathbf{z} .

5.1.4 Weighting inputs and outputs

In the generalized control problem, the objective is to minimize a norm between specific inputs and outputs. To meet the control aims, it is necessary to choose those signals accordingly. The choice of signals is insufficient as such, and additional weights should be included to fine-tune the control problem.

In Fig. 5.6, the feedback control problem is presented. The symbols d_i and d_o denote the input and output disturbances, respectively, n is the sensor noise, r is the reference signal, u is the control signal, and y is the output signal of the plant.

Although there is no theoretical difference, it is possible to distinguish two approaches for choosing the signals and their weights. The first one is a loop-shaping and the second one a signal-based approach by Skogestad and Postlethwaite (2005).

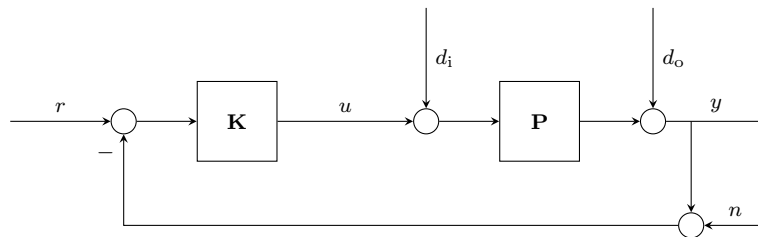


Figure 5.6. Feedback control problem. The control problem with additional inputs for noise n , input d_i , and output d_o disturbances.

Loop-shaping

In the loop-shaping procedure of the tuning the controller, based on the specifications, the engineer changes several closed-loop transfer functions that have a specific meaning. This specific meaning gives some insight into the control problem and makes the process more intuitive.

One popular solution is to use a mixed sensitivity approach. In that case, the sensitivity function is shaped along with other transfer functions. The list of important transfer functions with their meanings is presented in Table 5.1 (Zhou and Doyle, 1998, Chapter 6).

Table 5.1. Important transfer functions.

Function	Name	Meaning
$\mathbf{L}_i = \mathbf{K}\mathbf{P}$	Input loop transfer function	
$\mathbf{L}_o = \mathbf{P}\mathbf{K}$	Output loop transfer function	
$\mathbf{S}_i = (\mathbf{I} + \mathbf{L}_i)^{-1}$	Input sensitivity transfer function	Actual plant input
$\mathbf{S}_o = (\mathbf{I} + \mathbf{L}_o)^{-1}$	Output sensitivity transfer function	Performance tracking
$\mathbf{T}_i = \mathbf{L}_i(\mathbf{I} + \mathbf{L}_i)^{-1}$	Input complementary sensitivity function	Input usage disturbance function
$\mathbf{T}_o = \mathbf{L}_o(\mathbf{I} + \mathbf{L}_o)^{-1}$	Output complementary sensitivity function	Performance noise

The scheme for the mixed sensitivity approach is presented in Fig. 5.7. By providing a specific weight for each exogenous output, it is possible to apply the necessary requirements for the general control problem presented in Fig. 5.2. The question of choosing weights is a vast one; however, the general rule is to provide a low-pass filter for the output sensitivity function \mathbf{S}_o . The weight for the $\mathbf{K}\mathbf{S}_o$ function should have a bandwidth equal to the desired bandwidth of the controller. To minimize the disturbance from the noise, the complementary sensitivity weight is usually a high-pass filter (Skogestad and Postlethwaite, 2005). Another popular approach to shape the plant is proposed by Glover and McFarlane (1989). With this method, the designer should provide the input and output weights. Thus, a desired open-loop shape of the plant is obtained. The general scheme for the approach is presented in Fig. 5.8. In the figure, \mathbf{W}_1 and \mathbf{W}_2 denote pre- and postcompensators. In the postcompensator, the importance of a particular output is usually emphasized. Again, the precompensator defines the shape of the plant and usually contains an integral part (Skogestad and Postlethwaite, 2005). The shaped plant for the controller synthesis is obtained as

$$\mathbf{G}_s = \mathbf{W}_1 \mathbf{G} \mathbf{W}_2. \quad (5.5)$$

After that, a common \mathcal{H}_∞ procedure is applied to obtain a controller \mathbf{K}_s . To get the

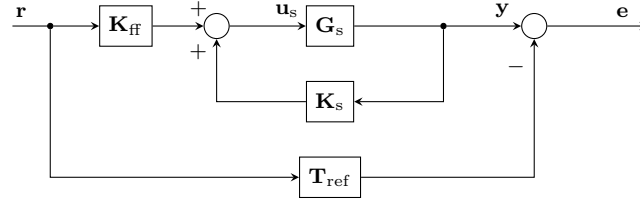


Figure 5.9. Glover-McFarlane \mathcal{H}_∞ two-degrees-of-freedom scheme. One additional weight is added. The reference transfer function (\mathbf{T}_{ref}) describes the desired closed-loop dynamics of the system.

signal. This is useful when there are strict time-domain specifications for the output signals. In the case of an AMB system, this may take place during the initial levitation when overshoot is not desired. However, the stability and response to disturbances are fully defined by the closed-loop part of the system. The approach discussed by Glover and McFarlane (1989) is intended to maximize the stability margin of the plant. The stability margin is estimated for the coprime uncertainty description of the plant. The description is presented in Fig. 5.10. It gives the following set of plants

$$G = (M_1 + \Delta_M)^{-1}(N_1 + \Delta_N), \quad \|[\Delta_N \quad \Delta_M]\|_\infty \leq \epsilon. \quad (5.8)$$

In the equation, M_1 and N_1 denote the left coprime factorization of the plant $G = M_1^{-1}N_1$. Thus, M_1 contains all the right-hand plane poles, and N_1 contains all the right-hand plane zeros of the plant G . The uncertainty is moved to the Δ with the specific subscript. This kind of an uncertainty description is very general, and both the poles and zeros can shift to the right-hand plane. The procedure allows to find a controller and robustly stabilize the plant. The approach gives the maximum stability margin with respect to the coprime uncertainty. The uncertainty itself should be included into the plant model with pre- and postcompensators. Thus, it is not possible to apply a directly structured uncertainty as it should be converted into specific weights. On the other hand, the great benefit of the method is that it gives an explicit solution by solving two Riccati equations. Other \mathcal{H}_∞ methods require several steps with the DK iteration procedure (Zhou and Doyle, 1998).

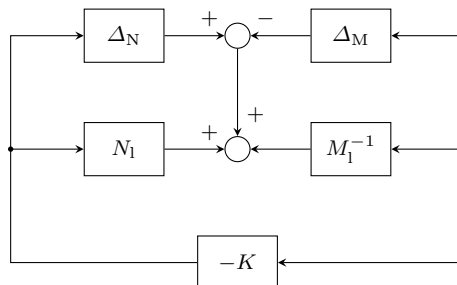


Figure 5.10. Coprime uncertainty description.

5.1.5 Weight selection

Above, two approaches to robustly stabilize the plant were discussed. In the first one, it is possible to directly include structured uncertainty, while the second requires additional steps in weight selection to take the uncertainty into account. Finally, it can be noted that both methods require an accurate choice of weights. There are some basic guidelines and step by step procedures proposed by different authors. A systematic \mathcal{H}_∞ loop-shaping design procedure is given in (Skogestad and Postlethwaite, 2005, Chapter 9). Extensive guidelines are presented in (Zhou and Doyle, 1998, Chapter 16). However, the problem is still iterative and requires some experience.

One way to overcome such a problem is proposed in the robust identification of the system. A set of weights for the Glover–McFarlane approach are obtained during identification (Oomen and Bosgra, 2012). Other authors use genetic algorithms and their modifications to find suitable weights. In the work of Smirnov and Jastrzebski (2009), weights for Glover–McFarlane procedure are obtained. For the mixed sensitivity design, the weights are found in the work of Jastrzebski et al. (2010). With genetic algorithms, the problem of specifying a good objective function is relatively hard to solve. The problem of choosing weights is complex. The solution depends significantly on the particular application and its requirements. In this work, as the general structure of the plant is known, the problem can be reduced. First, it is pointed out that MIMO AMB systems actually have very similar inputs and outputs. The importance of these inputs and outputs is equal. Thus, each signal in the system should have a similar weight extended to four channels.

Secondly, AMB systems, above all, require stability and then, disturbance rejection. Thus, time-domain constraints do not play a crucial role. The main objective is to shape the closed-loop part of the system. The feed-forward can be added as an extension mainly to the initial levitation. The flexible modes of the rotor and the structural resonances can be treated with a notch filter added to the weight. In the case of flexible modes, it should be large enough to cover the splitting range of modes in the operating point.

In the case of shaping, special attention should be paid to the minimization of the output sensitivity function peak. Based on that value, AMB systems are graded in the ISO standard (Li et al., 2006). In addition, it is always desirable to add an integral action. It removes the steady-state offsets caused by constant disturbances. In the process of automatic commissioning, some controllers should already be synthesized based on the analytical model. After tuning the parameters of the system by the identification procedure, the same controllers should be synthesized again. It may be necessary only to tune the frequencies of the notch filters and their width.

Taking into account the above considerations and the actual plant of the system, the weights are specified with transfer functions in Section 5.4.2.

5.2 Bumpless switching

The modern control theory can provide controllers that are robust to some uncertainty in the plant model, as it was discussed in Section 5.1. Thus, such controllers may satisfy the robust stability and robust performance criteria under some changes that take place in an actual plant. However, it might be impossible to meet all the requirements with one controller for all operating conditions. The conditions may change according to some law as discussed in Section 5.3, or they may change in an unpredictable way. The second case includes changes in the surrounding environment that occur rarely and are included in the control law as constants. These can include temperature, humidity, natural frequencies of foundation, and many other factors.

It can be stated that it is always beneficial to update the controller according to the changing environment. However, a straightforward way to stop the plant and reprogram the controller may not be feasible or it is too expensive. It is always easier to carry out such tasks remotely and seamlessly.

A direct switch from one controller to another produces a bump in the control signal. These controllers are usually referred to as off-line and on-line controllers (see Fig. 5.11). An off-line controller has the same inputs as the on-line one. After some time, working under the same conditions, the input of the plant is shifted from the on-line controller to the off-line one. During the switch, glitches may appear in the control signal damaging the process quality or leading to instability in the worst case. The reason is that different controllers have different levels of control signal for the same operating conditions. The difference in the control signal level during the switch acts as an input disturbance, which is undesirable. To avoid the problem, there is a bumpless switch technique.

One solution is to close the off-line controller by the feedback gain to drive the control signal close to the on-line one. This method tends to be inefficient especially in the case of modern high-order controllers that have right half plane zeros (Green, 1995).

Another bumpless transfer scheme was implemented by Hanus et al. (1987), but it is conservative in some ways, as it is discussed by Turner and Walker (2000). Further, the technique is developed for the linear quadratic (LQ) bumpless transfer based on the works of Turner and Walker (2000, 1999) and investigated further in (Zheng et al., 2006). Another extension to the method deals with the controller uncertainty (Zheng et al., 2009). Bendtsen et al. (2005) and Li (2007) used bumpless transfer for the gain-scheduled techniques.

In this work, bumpless transfer is implemented according to the work of Turner and Walker (2000). The decision is based on the idea that such an approach does not require much computation power and guarantees inner-loop stability of the off-line controller.

The state feedback signal α for the off-line controller according to Turner and Walker

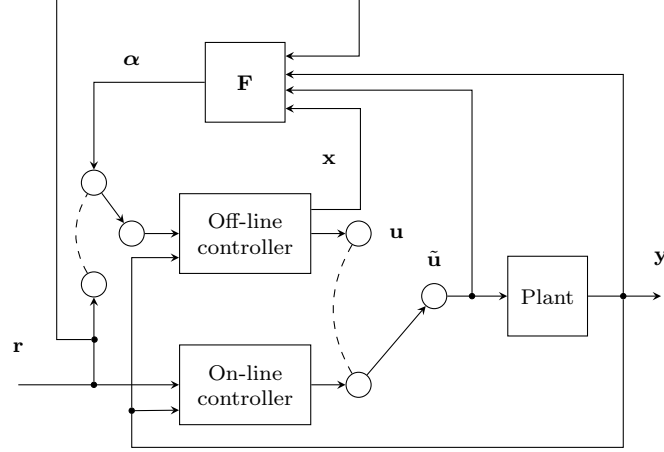


Figure 5.11. Bumpless transfer scheme. When the difference between the control signals for the on-line ($\tilde{\mathbf{u}}$) and off-line (\mathbf{u}) controllers is small, the system switches to the off-line controller.

(2000) is calculated as

$$\boldsymbol{\alpha} = (\mathbf{I} - \mathbf{A}\mathbf{B}_1^T\mathbf{P}\mathbf{B}_1)^{-1} \mathbf{A} \begin{bmatrix} (\mathbf{D}_1^T\mathbf{W}_u\mathbf{C} + \mathbf{B}_1^T\mathbf{P})^T \\ (\mathbf{D}_1^T\mathbf{W}_u\mathbf{D}_2 - \mathbf{B}_1^T\mathbf{M}\hat{\mathbf{Y}})^T \\ (-\mathbf{D}_1\mathbf{W}_u + \mathbf{B}_1^T\mathbf{M}\hat{\mathbf{U}})^T \\ (-\mathbf{W}_e + \mathbf{B}_1^T\mathbf{M}\hat{\mathbf{R}})^T \end{bmatrix} \begin{bmatrix} \mathbf{x} \\ \mathbf{y} \\ \tilde{\mathbf{u}} \\ \mathbf{r} \end{bmatrix}, \quad (5.9)$$

where \mathbf{x} , \mathbf{y} , $\tilde{\mathbf{u}}$, and \mathbf{r} are the state vector of the off-line controller, the measured output of the plant, the control signal of the on-line controller, and the reference signal, respectively. Eq. (5.9) assumes that the off-line controller has two degrees of freedom and can be divided into

$$\mathbf{B} = [\mathbf{B}_1 \ \mathbf{B}_2] \quad \mathbf{D} = [\mathbf{D}_1 \ \mathbf{D}_2], \quad (5.10)$$

where the subscripts 1 and 2 denote the feed-forward and feed-back parts, respectively. The rest of Eq. (5.9) is shortened according to

$$\mathbf{A} = -(\mathbf{D}_1^T\mathbf{W}_u\mathbf{D}_1 + \mathbf{W}_e)^{-1}, \quad (5.11)$$

$$\mathbf{M} = (\tilde{\mathbf{A}}^T + \mathbf{P}\tilde{\mathbf{B}})^{-1}, \quad (5.12)$$

$$\tilde{\mathbf{Y}} = (\mathbf{C}^T\mathbf{W}_u\mathbf{D}_1 + \mathbf{P}\mathbf{B}_1)\mathbf{A}\mathbf{D}_1^T\mathbf{W}_u\mathbf{D}_2 + \mathbf{P}\mathbf{B}_2 + \mathbf{C}^T\mathbf{W}_u\mathbf{D}_2, \quad (5.13)$$

$$\tilde{\mathbf{U}} = \mathbf{C}^T\mathbf{W}_u + (\mathbf{C}^T\mathbf{W}_u\mathbf{D}_1 + \mathbf{P}\mathbf{B}_1)\mathbf{A}\mathbf{D}_1^T\mathbf{W}_u, \quad (5.14)$$

$$\tilde{\mathbf{R}} = (\mathbf{C}^T\mathbf{W}_u\mathbf{D}_1 + \mathbf{P}\mathbf{B}_1)\mathbf{A}\mathbf{W}_e, \quad (5.15)$$

$$\tilde{\mathbf{A}} = \mathbf{A} + \mathbf{B}_1\mathbf{A}\mathbf{D}_1^T\mathbf{W}_u\mathbf{C}, \quad (5.16)$$

$$\tilde{\mathbf{B}} = \mathbf{B}_1\mathbf{A}\mathbf{B}_1^T, \quad (5.17)$$

$$\tilde{\mathbf{C}} = \mathbf{C}^T(\mathbf{W}_u + \mathbf{W}_u\mathbf{D}_1\mathbf{A}\mathbf{D}_1^T\mathbf{W}_u)\mathbf{C}. \quad (5.18)$$

To find out \mathbf{P} and ensure the inner stability the Riccati equation is solved

$$\mathbf{P}\tilde{\mathbf{A}} + \tilde{\mathbf{A}}^T\mathbf{P} + \mathbf{P}\tilde{\mathbf{B}}\mathbf{P} + \tilde{\mathbf{C}} = 0. \quad (5.19)$$

The solution can be tuned to the specific requirements by adjusting two weights (\mathbf{W}_e and \mathbf{W}_u). The first one allows to emphasize the difference between the reference signal and the state feedback signal α . The second weight tunes the difference between the off-line and on-line control signals. These weights are diagonal positive-definite matrices with the corresponding dimensions.

To validate the above approach, an SISO axial AMB system was used as a plant. Two different controllers are synthesized and switched. It is seen in Fig. 5.12 that there is a significant overshoot at the moment of switching. To avoid this drawback, a bumpless approach is taken with $\mathbf{W}_u = 10^3$ and $\mathbf{W}_e = 0.1$. The rotor is moved out from the central position to simulate the effect of an output disturbance such as gravity. In

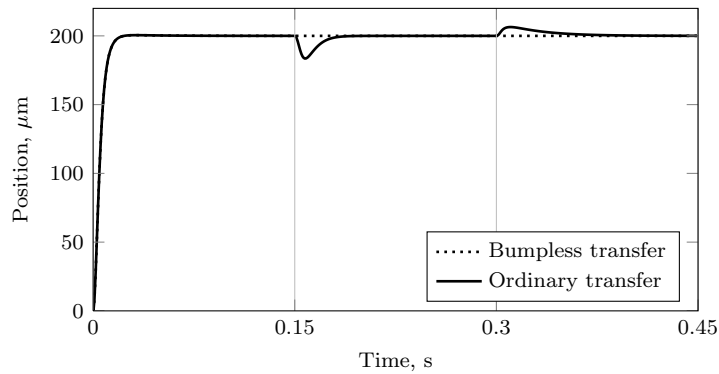


Figure 5.12. Simulation of the system with the bumpless transfer and ordinary transfer approaches. The system switches to the new controller at 0.15 s and back to the previous one at 0.3 s.

Fig. 5.12 the bumpless scheme has reduced the overshoot and ensured stable operation of the plant.

The hardware implementation of the bumpless scheme and experimental results for axial AMBs are discussed by Smirnov et al. (2010).

5.3 LPV control

It was discussed above that uncertainties degrade the performance and stability of an AMB system. The modern control theory can provide robustness and guarantee stability in some range. To extend the stability region, some additional information can be used and provided for the controller.

A widely used approach to deploy additional information about the system is the gain-scheduling method. Assuming one varying parameter available for the measurement, a set of controllers are synthesized. Each controller satisfies the requirements in a short range around a particular value of the parameter. To obtain stability and performance in the full range, there are two alternative strategies. The first one is to explicitly switch to the next controller when the system gets into a new range of the parameter. Thus, the boundaries for each controller are strictly defined. The second approach is to get the two closest controllers and interpolate their gains in proportion to the distance. The interpolated controllers are called gain-scheduled controllers (Leith and Leithead, 2000).

The parameter in an AMB system that is almost always available for measurements is the rotational speed of the rotor Ω . If the rotational speed is significant or a polar moment of inertia of the rotor is greater than the diametral one $I_p > I_a$, the system is considered gyroscopic (Schweitzer and Maslen, 2009, Ch. 10).

For the gyroscopic systems, the rotor speed has a significant influence on the frequencies of the flexible modes. It causes a splitting effect when one natural frequency splits into forward and backward modes. These modes have a higher and lower frequency, respectively (see Fig. 5.13). The splitting causes the corresponding poles to shift considerably in the frequency response. Li et al. (2006) show that a ν -gap metric can be high for changing the frequencies of the flexible modes. This means that from the feedback perspective, the systems are different, and obtaining the robustness can be problematic. However, the controller must stabilize the system in the full range of the operating speed.

To overcome this problem, the speed measurements available are used. The speed is considered a varying parameter, and a set of different controllers are synthesized for different rotational frequencies. When applying the first approach described at the beginning of the section, a problem during the switch appears. The levels of the control signal are different for different controllers in the same operating point. In the case of a MIMO system, the problem can cause even more problems as there are several output signals, all with different values. One option to overcome the issue is to apply a bumpless switch technique proposed by Turner and Walker (2000) and described in Section 5.2. An extension of this approach is to synthesize the robust controllers and provide switching between them as suggested in AMB system by Li (2007).

The second approach to avoid bumps is to interpolate the controllers along with a changing parameter, which is the rotor speed in this case. The method places some restrictions on the controllers. They should have the same order and structure. In addition, the problem of verifying the robustness and stability arises. Theoretically, such an interpolation does not guarantee stability during the transition from one controller to another (Leith and Leithead, 2000). Thus, a significant effort should be put on validating the controllers in the full speed range, under different disturbances, and variation of other parameters.

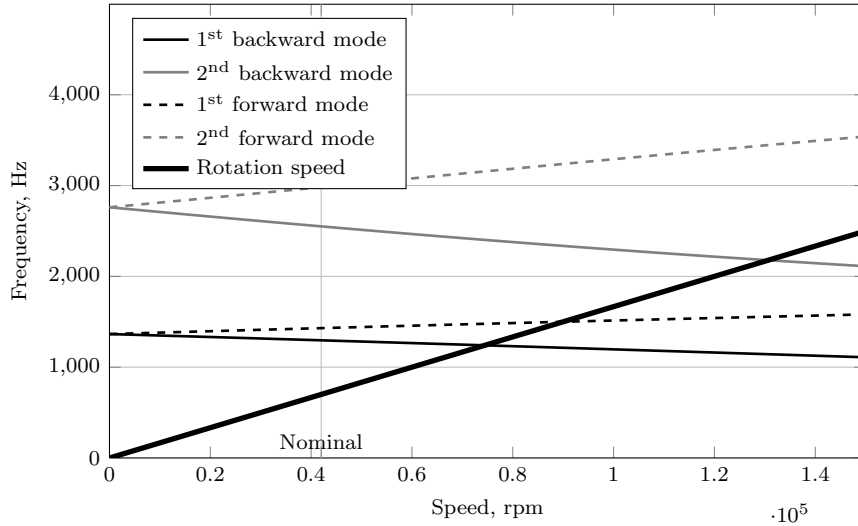


Figure 5.13. Campbell diagram for the rotor with an impeller. The nominal speed is indicated by the vertical line. Two first flexible modes and their splitting are demonstrated. The operation point is far below the first backward mode.

In particular, a model of AMBs can be presented as a system where the rotor speed is a linearly varying parameter. Thus, it is referred to as a category of LPV systems, for which special LPV gain-scheduling methods can be applied. These methods are free of the above-mentioned drawbacks and provide a unified approach to the controller synthesis.

Matsumura et al. (1996) presented one of the first examples in the AMB system to systematically adjust the controller to the rotor speed. In their paper, the sinusoidal disturbance of a rigid rotor is rejected with a robust loop-shaping controller. It is done in an \mathcal{H}_∞ framework by applying additional boundary constraints.

The LPV theory is applied to a rigid rotor AMB system by Lu et al. (2008). The authors provided additional techniques to systematically capture uncertainty from the measurements available and provide weighting functions for the general control problem. The problem is also solved in an \mathcal{H}_∞ framework, which is presented with a Lyapunov function as a set of parameter-dependent LMIs.

The problem of LPV controllers was also investigated in the work of Li (2007), where the author compared an LFT approach with a Lyapunov function approach and additionally, with a “frozen” \mathcal{H}_∞ controller. The model used is highly accurate, including not only higher-frequency modes but also structural resonances resulting in a nominal model with as many as 48 states. However, the author provided the comparison based only on the theoretical γ values of \mathcal{H}_∞ controllers.

5.3.1 LPV model of the AMB system

From the equation of motion for the rotor (2.41) we can see that it depends on the rotational speed. The speed appears as a multiplier for the gyroscopic matrix \mathbf{G}_M , which has a skew-symmetric structure. Thus, the gyroscopic matrix provides a coupling between the x and y planes of the rotor. It is easy to see that the system depends on the speed in an affine way, and can thus be expressed in an LPV form as follows

$$\begin{aligned}\dot{\mathbf{x}}_r &= \mathbf{A}_r(\Omega)\mathbf{x}_r + \mathbf{B}_r(\Omega)\mathbf{u}_r, \\ \mathbf{y}_r &= \mathbf{C}_r(\Omega)\mathbf{x}_r + \mathbf{D}_r(\Omega)\mathbf{u}_r.\end{aligned}\quad (5.20)$$

Actually, Eq. (5.20) describes the general form of the LPV system. In the particular case discussed in this work, only the matrix \mathbf{A}_r depends on the parameter Ω . Similarly as is Section 2.5, the system is extended with an actuator model. This leads to a full AMBs model in the LPV form as follows

$$\begin{aligned}\dot{\mathbf{x}} &= \mathbf{A}\mathbf{x}(\Omega) + \mathbf{B}\mathbf{u}, \\ \mathbf{y} &= \mathbf{C}\mathbf{x} + \mathbf{D}\mathbf{u}.\end{aligned}\quad (5.21)$$

5.3.2 LPV controller implementation

For the model obtained in Eq. (5.21), it is possible to synthesize an LPV controller. In this work, the approach proposed by Apkarian et al. (1995) is used. The parameter-dependent plant is divided into a set of systems, each corresponding to a vertex. The vertex represents an extreme combination of time-varying parameters. In this work, the only varying parameter available for the measurements is the speed Ω . Thus, there are two vertices $\Omega \in [0, \Omega_{\max}]$. The strict mathematical definition is given as

$$\Omega = \left\{ \sum_{i=1}^r \alpha_i \omega_i : \alpha_i \geq 0, \sum_{i=1}^r \alpha_i = 1 \right\}, \quad (5.22)$$

where r denotes the number of vertices and w_i is a specific vertex, and α_i denotes the relative distance between vertices. In such a notation, the plant model for each vertex is defined by the corresponding state-space matrices \mathbf{A}_i , \mathbf{B}_i , \mathbf{C}_i , and \mathbf{D}_i . It is shown by Apkarian et al. (1995) that if the quadratic \mathcal{H}_∞ performance holds for each vertex, then it holds for all trajectories of the varying parameters. Thus, for each vertex, the controller \mathbf{K} with the same Lyapunov function is synthesized, and then scheduled along the parameter trajectory as

$$\begin{bmatrix} \mathbf{A}_K(\Omega) & \mathbf{B}_K(\Omega) \\ \mathbf{C}_K(\Omega) & \mathbf{D}_K(\Omega) \end{bmatrix} = \sum_{i=1}^r \alpha_i \omega_i \begin{bmatrix} \mathbf{A}_{K_i}(\Omega) & \mathbf{B}_{K_i}(\Omega) \\ \mathbf{C}_{K_i}(\Omega) & \mathbf{D}_{K_i}(\Omega) \end{bmatrix}, \quad (5.23)$$

where \mathbf{A}_K , \mathbf{B}_K , \mathbf{C}_K , and \mathbf{D}_K are the state-space matrices of the controller in a particular point, and the same matrices for a specific vertex are denoted by the subscript i .

5.4 Controller synthesis

In this work, a set of different controllers are synthesized and evaluated for the investigated AMB system. In total, there are four different types, which are: \mathcal{H}_∞ mixed-sensitivity, \mathcal{H}_∞ Glover-McFarlane, LPV controller, and \mathcal{H}_∞ gain-scheduled. The last controller is a set of two \mathcal{H}_∞ mixed-sensitivity controllers synthesized for zero and maximum values of the rotor speed and scheduled (interpolated) according to (5.23). Thus, the \mathcal{H}_∞ gain-scheduled controller is also addressed as an interpolated controller.

The main objective was to achieve closed-loop robust stability and good disturbance rejection. Thus, the quantity to compare these controllers is the maximum value of the output sensitivity function S_o (see Table 5.1).

5.4.1 AMB system from a control point of view

For the controller evaluation, a system with a second rotor is used with an impeller attached to it. Thus, it corresponds closer to a system in a production environment with nominal loads.

The model of the system for the controller synthesis includes only rigid body modes. According to the Campbell diagram (see Fig. 5.13) and the identification results, the frequency of the first flexible mode is high enough to consider the system subcritical.

The system with an impeller has a significant gyroscopic effect. It introduces variation in the frequency characteristic of the plant at different rotational speeds. An example of pole shifting according to the rotational speed is presented in Fig. 5.14.

The right-half plane (RHP) poles introduce some limitations to the controller (Skogestad and Postlethwaite, 2005). Thus, the bandwidth of the closed-loop system should be two times greater than the frequency of the unstable pole. In a strict mathematical description, this requirement is presented as follows

$$\bar{\sigma}(\mathbf{T}(j\omega)) \geq 1, \quad \omega \leq 2|p|, \quad (5.24)$$

where $\bar{\sigma}$ is the maximum singular value, \mathbf{T} is the complementary sensitivity function, and p is the frequency of the unstable pole. In the discussed system there is a pole in the RHP with the frequency of 282 rad s^{-1} . The minimum closed-loop frequency of the system should be 564 rad s^{-1} .

For all the controllers except for the LPV and gain-scheduled controllers, the speed parameter is unknown and thus treated as an uncertainty. For the LTI controllers, speed cannot be included directly in the model for the controller synthesis. This parameter does not depend on the states or inputs of the system. It is a parametric real-valued uncertainty. For the controller synthesis, it is solved as described in

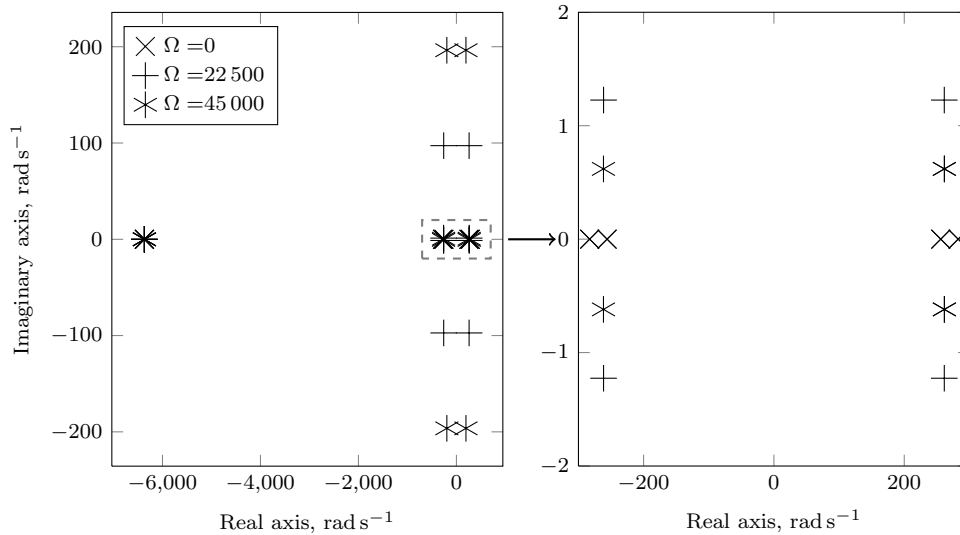


Figure 5.14. Pole location for the AMB system at different rotational speeds. The gyroscopic effect shifts the poles from the real axis. As a result, instead of identical real-valued poles, a complex conjugate pole pair appears.

Section 5.1.2. Thus, the system has additional exogenous inputs and outputs related to the uncertainty. The rest of the parameters describing the system such as the current and position stiffnesses (k_i and k_x) are identified and considered to have small variations. Inclusion of an excessive number of uncertainties may lead to conservative controllers.

With the above-mentioned techniques, the objective is to minimize the infinite norm for these inputs and outputs thereby reducing the effect of rotational speed on the system performance. In the case of a subcritical system with rigid modes, only this uncertainty results in two additional inputs and outputs. This is the result of the skew-symmetric structure of the gyroscopic matrix. It can already be noted that such an approach is conservative. During the controller synthesis, each input and output is treated separately, although there is only one source of uncertainty.

The AMB system during operation is usually subjected to different external disturbances. The simplest one is the gravitational force. The disturbances differ for specific applications. In a case where the external disturbance can be modeled, it is included as a special transfer function in the controller synthesis procedure. That way, additional rejection of the specific disturbance is achieved. The question is very wide, it depends significantly on the application, and was not examined in the work. Thus, all disturbances are considered unknown.

The effect of uncertainty on the rigid system is demonstrated in Fig. 5.15 The nominal value for the plant is taken at 22 500 rpm, and the boundaries of the uncertainty are

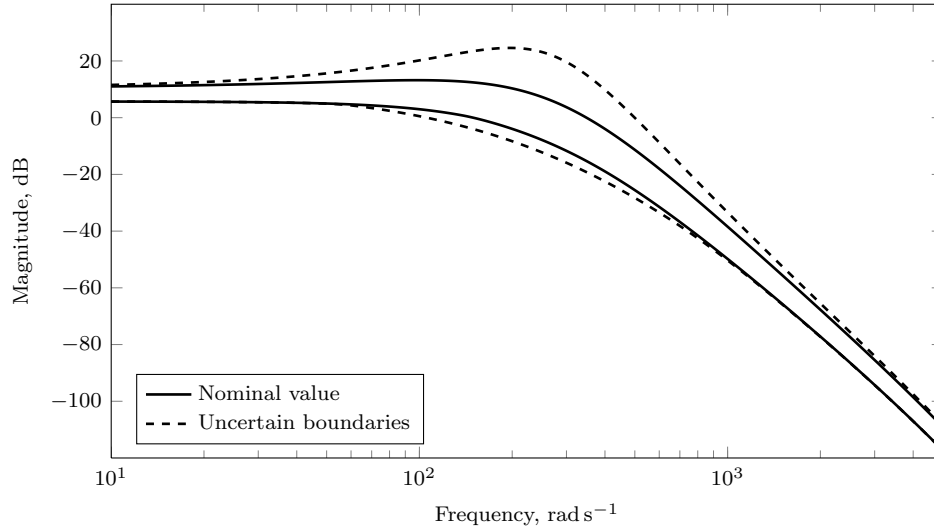


Figure 5.15. Singular values of the nominal system and the uncertainty boundaries (scaled system). The y axis unit values are $7 \times \text{mm A}^{-1}$.

calculated as the maximum and minimum singular values for 10 plants with evenly spaced speed values. It can be seen that the uncertainty alters the system significantly around the point where the frequency characteristic crosses the zero. This cross point is very important when considering the robust stability of the system. Theoretically, the inclination for the best robustness should be 20 dB for a decade. In addition to the above-mentioned challenges, the plant has an input delay that was estimated in Chapter 4. The value is approximated by the first-order Pade approximation and included in each input channel of the plant. To compare different controllers, some of them are synthesized with the inclusion of the delay, and some without.

5.4.2 Synthesis procedure

For the controller synthesis, the procedure proposed in Balas et al. (2011) is used with the model obtained from the identification procedure.

All the controllers except the \mathcal{H}_∞ Glover–McFarlane use the same weight scheme. It is an S/SK scheme that shapes the output sensitivity function and limits the usage of the control signal. The following weights are applied to the controller synthesis

$$\begin{aligned} \mathbf{W}_S &= 0.85 \mathbf{I}_{4 \times 4} \frac{1}{s+1} \cdot \frac{s+150}{1}, \\ \mathbf{W}_{KS} &= -10^3 \mathbf{I}_{4 \times 4} \frac{s+0.1}{0.1} \cdot \frac{50}{s+50}, \end{aligned} \quad (5.25)$$

where s is a Laplace variable. The first weight adds an integral action to the system and

shapes the bandwidth close to 150 rad s^{-1} . The gain of that weight at a high frequency is 0.85 to cut the peaks of the sensitivity function above $\frac{1}{0.85} = 1.1765$. The second weight limits the actuator usage above 50 rad s^{-1} . The weights are demonstrated in Fig. 5.16.

For the gain-scheduled controller, the plant is obtained at zero and maximum speeds, and adjusted with the above-mentioned weight functions. Thus, two controllers are obtained for two speed values. These two controllers are interpolated according to the particular speed in the same manner as an LPV controller in Eq. (5.23). The LPV controller is also synthesized for two points but using the described procedure that ensures the stability in each trajectory point.

For the Glover-McFarlane procedure, the open-loop plant is shaped with the following weight

$$\mathbf{W}_1 = \mathbf{I}_{4 \times 4} \frac{s + 100}{s + 0.1} \cdot \frac{s + 200}{200} \cdot \frac{1000}{s + 1000}. \quad (5.26)$$

The weight provides high enough gain at low frequencies with a slope of 20 dB in the range of 0.1 rad s^{-1} to 100 rad s^{-1} . The cut at 0.1 rad s^{-1} is necessary as the synthesis procedure requires proper weights. The slope of the plant was also altered around the crossover frequency to provide an inclination closer to 20 dB as it provides robustness for the system (Skogestad and Postlethwaite, 2005). Exact frequencies for changing the slope are compromised based on the variations of the plant at different speeds. For the reference weight of a closed-loop system, a second-order transfer function with a bandwidth of 300 rad s^{-1} is chosen as follows

$$\mathbf{W}_{\text{ref}} = \mathbf{I}_{4 \times 4} \frac{360^2}{s^2 + 2 \cdot 360s + 360^2}. \quad (5.27)$$

The function determines the desired bandwidth of the system and has approximately the same decline at frequencies above 300 rad s^{-1} as the initial plant model. These weights and also the plant before and after applying the weights are demonstrated in Fig. 5.17.

With the Glover-McFarlane approach and the chosen weights, the final order of the controller obtained is 40. Such a high-order controller produces too much computational burden for the prototype processing unit available. Thus, the order was reduced to 28 states with a modal reduction procedure (Safonov and Chiang, 1988). Further, for all the tests, a reduced version of the Glover-McFarlane controller was used.

5.4.3 Controller evaluation

All controllers are evaluated with the test rig available in the same conditions. A discrete version is used for the implementation. Discretization is carried out with a $100 \mu\text{s}$ sampling time and a bilinear approximation (Tustin) method. To reduce the computation burden, the controllers, if possible, are converted into a canonical form. For the LPV controller, the controller for the first vertex is canonized, and the

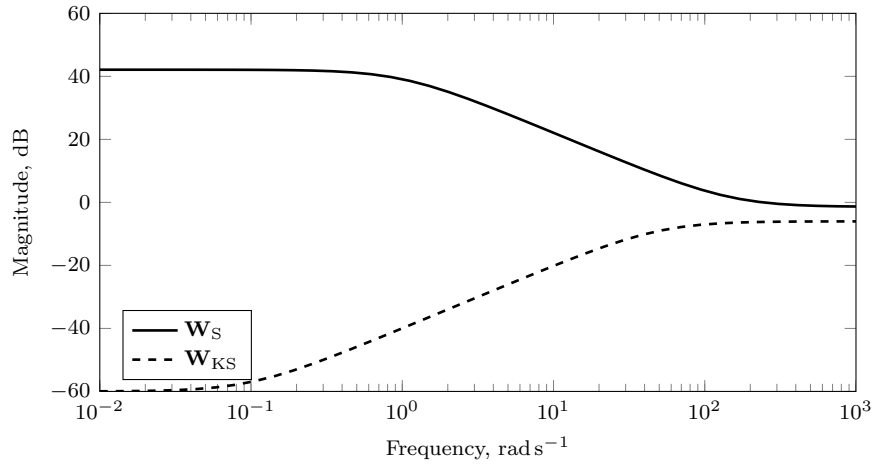


Figure 5.16. Weights for the mixed sensitivity problem.

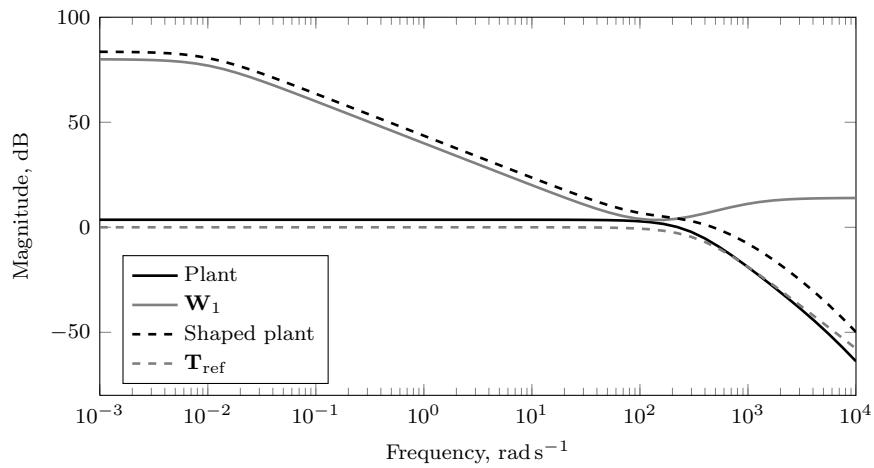


Figure 5.17. Weights, the plant at the nominal speed, and the weighted plant. Special attention is paid to the cross-over frequency to make the slope more gentle.

same transformation matrix is applied to the second vertex. However, that way, the diagonal structure of \mathbf{A} matrix is achieved only at a standstill.

To evaluate the necessity of the inclusion of a delay, an \mathcal{H}_∞ Glover-McFarlane approach is tested. Two controllers are synthesized with and without a delay, and both are tested with the prototype. The output sensitivity function is presented in Fig. 5.18. It is seen that an inclusion of a delay is important for the controller synthesis as it decreases the sensitivity function peak from 2.5556 to 2.1627 for 15 % of the measured results. Furthermore, it is demonstrated that the controller objectives are met; the plant is stabilized and the measured data correspond to the theoretical values. Based on the results, all other controllers are synthesized with an inclusion of a delay.

First, the theoretical performance of the controllers is evaluated. As one of the main objectives is to minimize the peak of the output sensitivity function, this value is chosen as an evaluation criterion. To evaluate the controllers, the output sensitivity function is calculated for each rotational speed. After that, the infinite norm for the function is found, which is the peak value for the particular speed. Mathematically, this can be expressed as

$$\|\mathbf{S}_o(s, \Omega)\|_\infty = \bar{\sigma}(\mathbf{S}_o(s, \Omega)), \quad \Omega \in [0, \Omega_{\max}]. \quad (5.28)$$

For LPV and gain-scheduled controllers, not only the plant but also the controller is updated according to the chosen speed.

In Fig. 5.19, the theoretical peak values for the output sensitivity function along the trajectory of the rotational speed are presented. These values are obtained for the controllers and the plant system that include time delay. For the synthesis procedure, the delay is approximated with a first-order approximation. For the evaluation, the fifth order is used in the plant model.

The theoretical results show that the mixed sensitivity approach with uncertainty and the LPV approach behave as expected. They are robust to the speed variation, and thus, the peak value does not change. The interpolated controller provides the best objective values at the vertices for which it was synthesized. Between the vertices, the peak value tends to increase. For the minimum and maximum speeds, the values of the sensitivity function for the interpolated and LPV controllers are almost identical within the numerical tolerance. The synthesis procedure for the LPV case uses LMIs, while the gain-scheduled controller uses γ -iteration with a default tolerance of 0.1. This results in a small difference between the vertex points; on the other hand, this small difference demonstrates the common nature (mixed sensitivity approach) of these controllers.

The robust controller has the worst peak sensitivity value. This is a consequence of the included structured uncertainty, and a trade-off for the robustness. The Glover-McFarlane controller has the best objective value below 35 000 rpm. It was synthesized for the plant at 22 500 rpm. Thus, the smallest peak value is in that region. When deviating from the nominal point, the peak value is growing. This is especially

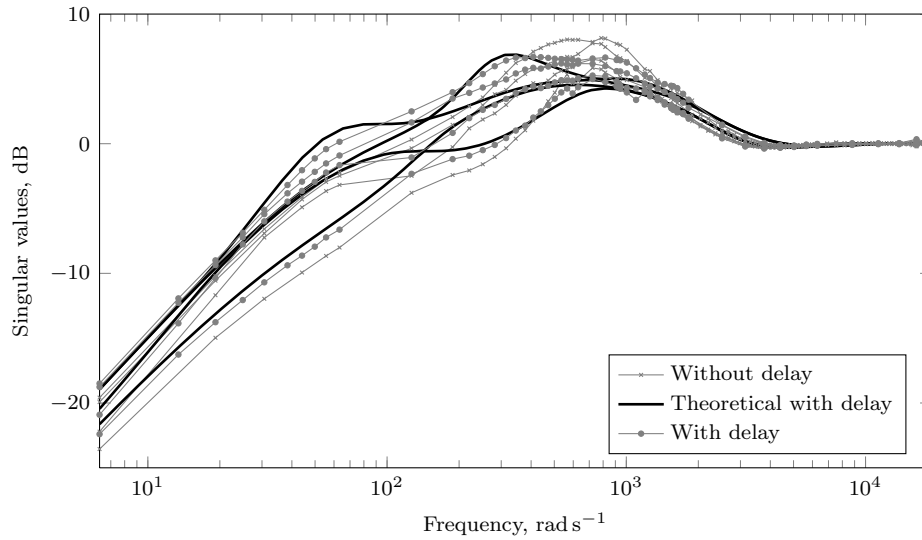


Figure 5.18. Singular values of the output sensitivity functions at a standstill. The controller with an inclusion of the delay has a smaller sensitivity peak. The differences between the measured and theoretical values are explained by the nonlinear nature of the system.

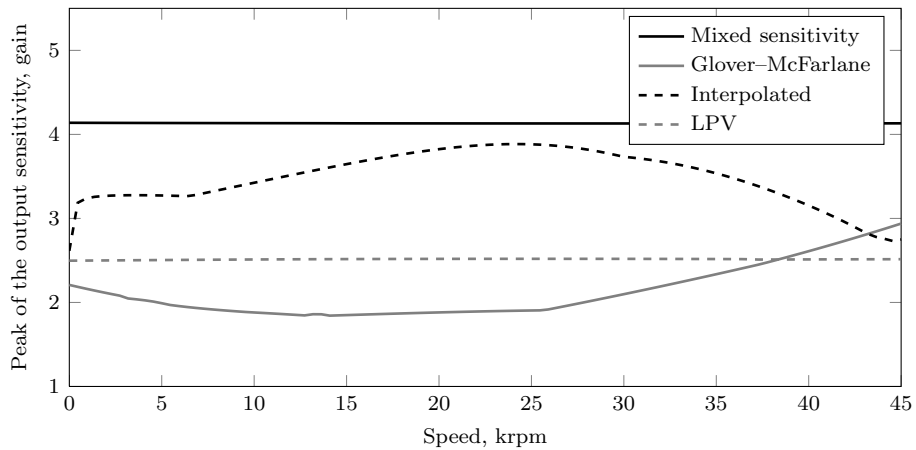


Figure 5.19. Peak values of the output sensitivity functions for different controllers. The values are obtained for the linear models with the time delay approximated by the transfer function of the order five.

noticeable with an increased speed, as the interaction between planes is stronger because of the gyroscopic effect, and the controller cannot handle it appropriately enough. In general, the objective values for a Glover-McFarlane controller are smaller compared with other controllers. The only exception is the LPV controller in the region above 35 000 rpm.

A direct comparison of the Glover-McFarlane controller with the others is not valid as the specifications for these controllers are provided in different ways. The main difference compared with the mixed sensitivity approach is that the parametric uncertainty caused by one parameter results in two inputs and outputs for the general problem formulation. As it was mentioned above, these inputs and outputs are treated separately in the synthesis procedure, thereby leading to conservative results as demonstrated in Fig. 5.19. The gain-scheduled and LPV controllers deal better with the conservatism, but the difference in weight schemes results in differences in the output sensitivity function. The weights for the Glover-McFarlane scheme are chosen by taking the uncertainty directly into account. In addition, the higher order of weights helps to meet the objectives accurately.

To verify the theoretical results, these controllers were implemented on a test rig. To estimate the peak value of the output sensitivity function, an excitation signal is provided at the corresponding input, and the position of the rotor is measured. The frequency of the excitation signal is chosen to be in the region of the theoretical peak value. As a result, the number of measurements required is reduced. After obtaining the measurements, the relation between the inputs and outputs of interest is found as in Eq. (4.3). Finally, the peak value is estimated as the maximum singular value for the full measured frequency range, Eq. (5.28). The speed of the rotor is varied in the range from zero to 25 000 rpm. The limitation of 25 000 rpm is imposed by the inverter used for operating the motor. However, the design point is 45 000 rpm, up to which point the rigid assumption of the rotor is valid (see Fig. 5.13). The results obtained for all controllers are presented in Fig. 5.20. The theoretical value for the LPV controller is also included for reference.

It can be seen that for the mixed sensitivity robust controller, the peak value does not change with the speed as it was expected based on the theoretical results. However, the absolute value is slightly higher; the theoretical value is 4.1 and the mean value is 4.88 for the practical results. An increase of 19% is explained by the differences in the theoretical linear model used for the controller synthesis and the actual system. In addition, the disturbances from the inverter and the runout on the rotor increase the peak value. However, the main feature, that is, the robustness to the speed variation is demonstrated by the controller.

The Glover-McFarlane controller shows the best results. The peak value at a standstill is even lower compared with the theoretical results; however, the difference is only 2%. This can be verified by examining the plots presented in Fig. 5.18. With an increasing rotational speed, the peak value also increases. The value is lower compared with other controllers; however, it differs from the theoretical results. This difference will

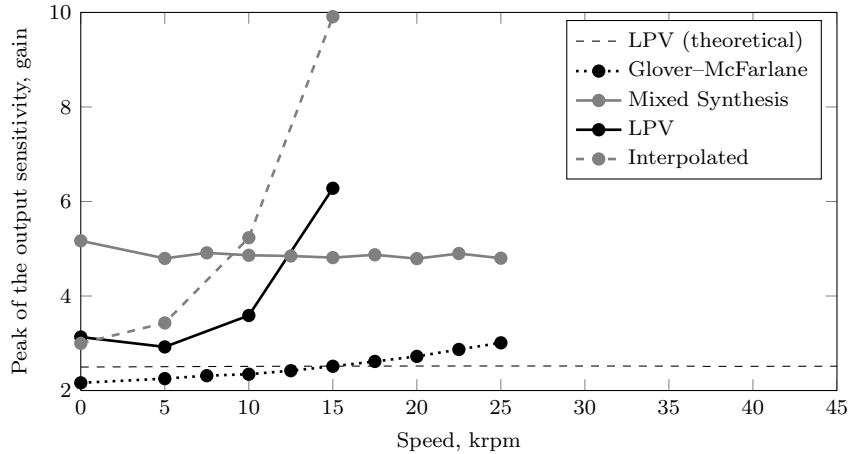


Figure 5.20. Measured peak values of the output sensitivity functions for different controllers. The measurements are carried out only to 25 000 rpm because of the hardware limitations imposed by the inverter used in the study. Two controllers demonstrate unstable behavior.

be discussed in more detail in this chapter.

The results for the interpolated and LPV controllers demonstrate an unstable behavior. With speeds above 15 000 rpm, the peak value grows significantly and the system loses its stability. An increase in the sensitivity function was expected for the interpolated controller. However, according to the theoretical results, the system should be stable in the full speed range. These two controllers are different from the other ones as they do not include any uncertainty. Thus, they have to be synthesized tightly to the theoretical model and cannot handle other uncertainties.

To improve the behavior of the LPV controller, it was decided to include uncertainty in the controller. The easiest way is to include a certain proportion of structured speed uncertainty similarly as it is done in the robust mixed sensitivity approach. Another option is to include additive or multiplicative dynamic uncertainty around the crossover frequency. The first approach is more straightforward and does not require accurate selection of weight. Thus, for each vertex in the LPV synthesis procedure, the plant model is updated to include 15% of the full speed variation. The value is estimated experimentally.

The results obtained for the original LPV and with inclusion of an uncertain set are demonstrated in Fig. 5.21. It can be seen that theoretically, the peak values are identical up to the numerical tolerance. The value has not increased as the included uncertain set is relatively small to the full variation as in the robust mixed sensitivity controller. The experiments also confirm that now the stability is achieved in the measured range. However, the value is growing with the speed. The system behaves similarly as was noticed above with the experimental results of the Glover-McFarlane controller. Such behavior is not predicted by the theoretical linear models.

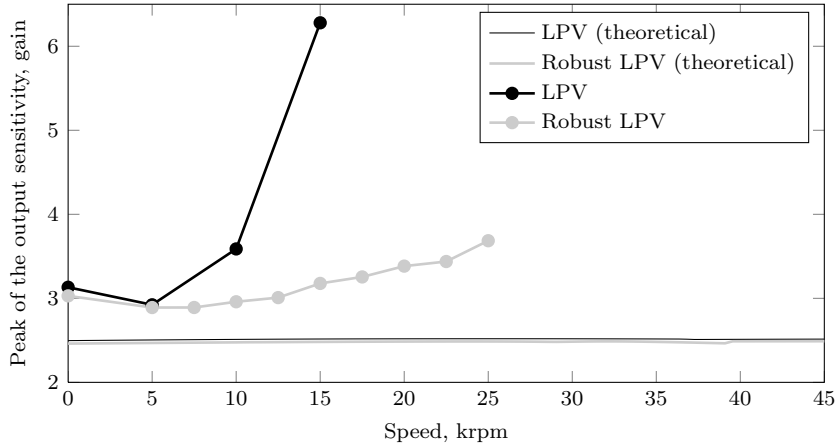
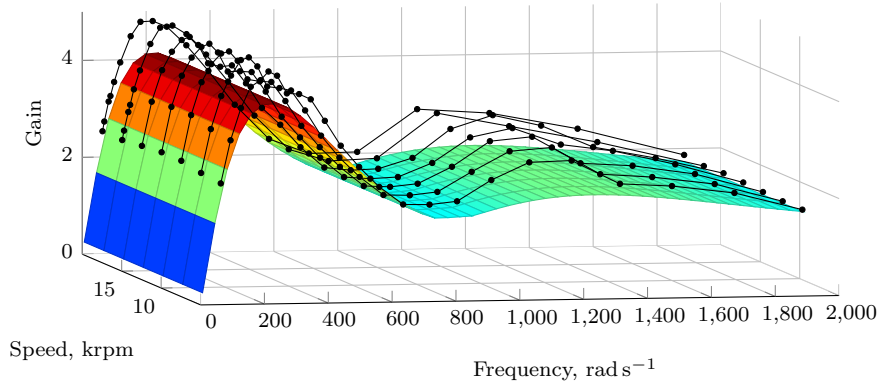


Figure 5.21. Peak values of the output sensitivity functions for LPV controllers. Inclusion of an uncertainty into the LPV controller makes it stable in the operating region.

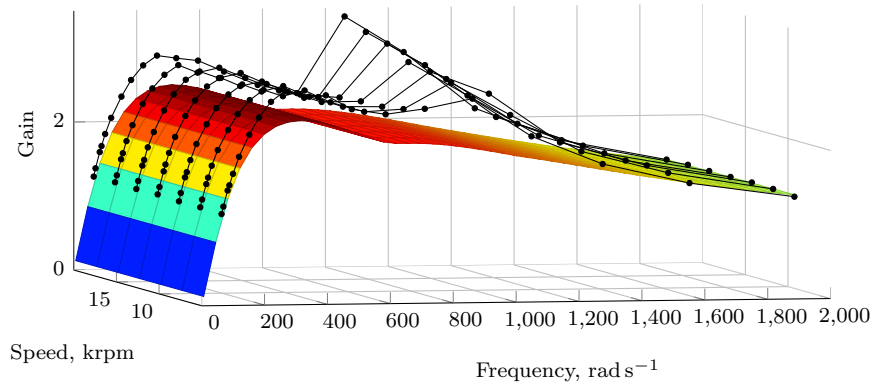
To investigate the reason for the above-mentioned behavior, the experimental results are plotted in Fig. 5.22. The surfaces represent the theoretical values for the output sensitivity function and the solid black lines the measured data. In the case of the LPV controller, the main contribution to the peak value is in the region between 800 rad s^{-1} to 1200 rad s^{-1} . A possible explanation is the structural resonance in that region. The system has been moved to a different basement after obtaining the identification results and thus the dynamics of basements may have changed. In addition, in this frequency range, a subharmonic from the three-phase rectifier propagates as a noise to the sensors and the actuators (Jastrzebski et al., 2012a). With a higher rotational speed, the structural resonance gets a higher excitation, which results in a higher sensitivity peak. The exact frequency of the measured peak for the LPV case is 860 rad s^{-1} .

For the Glover–McFarlane and robust controllers, the same resonance can be noticed. Although there is a difference, both these controllers have a band-stop filter behavior for the theoretical sensitivity function around the frequency in question. Thus, for the robust controller, the peak value is shifted to a higher frequency, and it is distributed in a wider region 910 rad s^{-1} to 1400 rad s^{-1} . Among the controllers under study, the Glover–McFarlane controller has the theoretical peak value with the highest frequency of 350 rad s^{-1} . This results in a growth in the sensitivity function around the original peak. In addition, the Glover–McFarlane controller was synthesized to achieve a better robustness exactly in this frequency region; see weights in Fig. 5.17. Thus, only a relatively small increase can be noticed around the structural resonance.

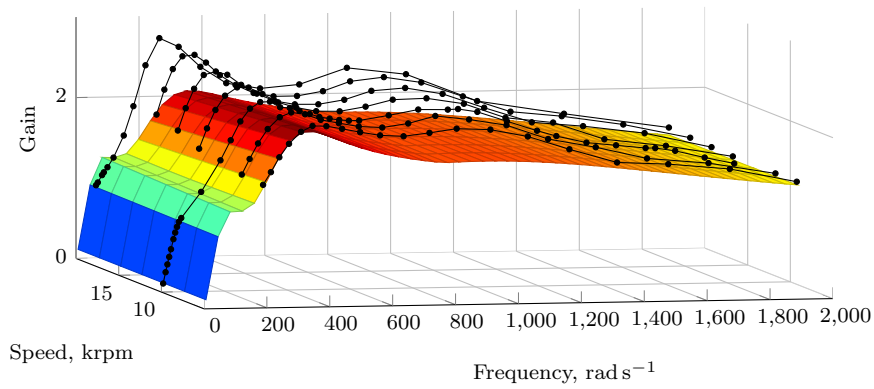
The displacement of the structural resonance frequency for different controllers takes place because of the water-bed effect (Skogestad and Postlethwaite, 2005); that is, the surfaces of an output sensitivity function above and below one must be the same. Thus, if suppressing one frequency band, there must be amplification in the other.



(a) Mixed



(b) LPV



(c) Glover-McFarlane

Figure 5.22. Experimental and theoretical values for the output sensitivity function around the peak value.

This also explains why the growth rates of the sensitivity peaks for the LPV and Glover–McFarlane controllers are very similar.

The best way to reduce the peak value arising from the structural resonance is to include that resonance in the plant model. That way, all the techniques can be directly applied without any changes in the weight schemes. Another solution is to include specially designed notch filters in the weights for the controller synthesis problems. A discussion on the weight design to overcome structural resonance is given by Jastrzebski et al. (2010).

5.5 Conclusions

This chapter provided the theoretical background for the applied control methods. The AMB system was analyzed from the control point of view, and its limitations were discussed. An \mathcal{H}_∞ framework for synthesizing a robust controller was presented.

As an objective for the controllers, the system stability and a small output sensitivity peak in the full operating range were chosen. A rotor with rotational speeds from zero to the maximum design value was described in the operating range. Thus, two models were presented; the first one considers speed as a parametric uncertainty. The second model is an LPV model that applies additional measurements of speed.

For the first case, a controller that uses a mixed sensitivity scheme and a Glover–McFarlane controller were synthesized. It was demonstrated that both controllers stabilize the system in the desired operating range. The Glover–McFarlane controller has a lower sensitivity peak value as the weight scheme takes the uncertainty directly into account, and is thus less conservative.

For the LPV plant, gain-scheduled and LPV controllers were implemented. The theoretical and experimental results demonstrate that in the gain-scheduled case, it is necessary to have a dense set of controllers over the speed variation. As it was shown, two vertices lead to inadequate performance and instability. The experimental results of the LPV controller also demonstrated instability. A further analysis showed that it is necessary to include a certain amount of uncertainty to make the system stable in the full range. The proportion of uncertainty was experimentally estimated to be 15 percent.

A further analysis of the experimental results explained the difference compared with the theoretical ones. The difference is a result of structural resonance that was not taken into account in the modeling process.

The test options for the system were limited and should be extended to obtain more representative results. From the results obtained, the Glover–McFarlane controller shows the best performance and can be suggested for the initial testing. Its structure

based on coprime uncertainty gives the best margin for unknown disturbances. After obtaining information about the system, the controllers with a mixed sensitivity scheme are more beneficial to use. They are easily adapted to the known uncertainties and modeled disturbances. The LPV controller combines both the option to be tuned as a mixed sensitivity scheme and additional information about the rotational speed, resulting in a better performance.

As a result, several controllers were obtained that can stabilize the system in the full operating range. The controllers stabilize the plant and achieve a reasonable sensitivity peak value even in the presence of unmodeled disturbances. Thus, the validity of the modeling and identification procedures was demonstrated.

Chapter 6

Conclusions

6.1 Summary

The main objective of the work was to provide an automated procedure for commissioning an AMB system. The problem was narrowed to the final stage when the number of tools and qualified personnel is limited. In that case, only the system itself can be used. Under such restrictions and assuming a priori knowledge of the system, the procedure was divided into several steps and automated.

The division is based on a bottom-to-top approach. First, the separate components were tuned, and finally, a tuning of a model-based controller for the whole system was performed.

The initial steps cover the tuning of an open-loop unstable plant. At this stage, the main concern was addressed to the sensors and actuators. First, the problem of sensor tuning was formulated as a problem of finding the offsets and geometric center of the rotor. These were solved by presenting the objectives in the form of an affine LMIs optimization problem. The optimal value provides not only the desired offsets along with the center point but also an estimate of the safe operation region in the worst conditions.

The actuator tuning problem was stated as a problem of finding a correspondence between the inputs and outputs of the system. This was done under an assumption that there might be a misalignment between the sensor and actuator planes. The solution was also expressed as an optimal value for the LMI optimization problem. It was demonstrated that with a limited number of measurements, it is possible to find the relation between the inputs and outputs and the angle between the planes. In addition, the number of measurements required was significantly reduced. This was done by constructing a special set of inputs based on the physical properties of an

AMB system.

The initial steps in the procedure were expressed as a mathematical optimization problem in the form of LMIs that can be solved efficiently with modern tools. The objective functions were expressed so that the results are easily transferred to the physical parameters of the system. Thus, an understandable and interpretable feedback was provided.

It can be concluded that the objectives and problems set for the open-loop system have been met and solved efficiently. This has been done under the above-mentioned restrictions and in an automated fashion so that the outputs of the procedures can be directly used for updating the parameters of the system and further steps.

As a second stage of the commissioning procedure, a system operation in the closed-loop was considered. The objective of this part was formulated as a synthesis and tuning of the controller that allows the stable behavior in the full operating range.

At the second stage, the system was identified in the frequency domain using a step-sine excitation method. The identification procedure was implemented for the gray-box model. This was done by tuning a specific set of parameters. The choice of these parameters and the necessary measurements were discussed. Under the identification procedure, an iterative approach was proposed. It allows to tune a limited amount of parameters to the measurements thereby improving the accuracy of tuning. Finally, the amount of measurements required and their sequence were discussed.

As a result of the identification procedure, a model suitable for the controller synthesis was obtained. Its parameters were tuned according to the measured data. This way, the uncertainty variation of these parameters is reduced. The identification procedure can be executed without human interaction. The obtained results can be directly provided for the fitting algorithms. Thus, only an agreement about the data formats between the measurements and the fitting procedure is required.

The model obtained in the identification step with an addition of uncertainty was used for the controller synthesis. A system that is stable in the full operating range was obtained. The set of obtained controllers were evaluated and compared from the disturbance rejection point of view. The results show that structured uncertainty description of the rotational speed is conservative compared with the coprime one. The necessity of an inclusion of the uncertain set in the LPV controller was shown. The amount of included uncertainty was experimentally estimated and found to improve the overall stability of the plant. Advantages of the LPV controller compared with the purely robust one were demonstrated.

As commissioning steps, identification and controller synthesis require significantly more computation power than the previous steps. The direct implementation of these algorithms on the chip tends to be challenging. Instead, these steps should be carried out remotely allowing to collect the data and update the controller. In order to

switch from the previous controller to the new one, a bumpless switching scheme was discussed and implemented. Such an approach provides a seamless controller update for the operating system.

The controller synthesis procedure is a complex one, and in some cases, it requires manual tuning of the weight functions. However, it was demonstrated that for the LPV approach with the mixed sensitivity scheme, it is possible to use the same weights and only update the plant model. Thus, stable operation is achieved.

The objectives stated in Chapter 1 were met. The proposed methods significantly reduce the time required for the commissioning of the prototype. In addition, the methodology helps to avoid human errors and provides additional diagnostics of the system.

6.2 Suggestions for future work

The scope of this work was limited by the ability to test and validate the proposed methods with the system available. Thus, a subcritical system with a specific structure of radial bearings was evaluated. Further work should be devoted to the extension of the methods to other AMBs arrangements.

The set of problems to be automated were chosen with the above-mentioned limitations in mind. To provide a broader view of the problem, more material should be collected from the commissioning results in the industry.

Considering the initial steps of the sensor and actuator tuning, it is necessary to investigate algorithms for a system with a homopolar bearing structure and a greater number of coils. The algorithm to estimate the misalignment requires to solve several optimization problems. The number of problems grows exponentially with the number of radial bearings in the system. Thus, research should be directed to reformulating the problem into a single optimization problem. In addition, extensive research and estimation of the accuracy of the proposed method are necessary.

The applied identification procedure for the gray-box model is limited to the fitting of only specified parameters. Unmodeled disturbances or features of the system result in the shifted estimation of the parameters. Instead of the step-sine excitation method, the multisine method should be applied to reduce the time spent on collecting data for the identification.

The controller synthesis demonstrated that the system is sensitive to the foundation resonances that lie in the bandwidth of the controller. These resonances should be accurately taken into account in the system model and the identification procedure. The external disturbances coming from the impeller were neglected in the work. The inclusion of these disturbances in the controller synthesis can significantly improve

the performance of the system. The experimental results demonstrated that a hand-tuned system still provides better robustness and disturbance rejection. Hence, the automated procedure for controller synthesis requires additional investigation.

Crossing of the flexible modes and operating in the supercritical region will pose additional challenges to the commissioning. These challenges should be tackled in the future.

In the applied controller techniques, stable operation was required in the full operating range. However, AMB systems usually operate at certain specific rotational speeds, and thus, the best characteristics are expected around these points. There are LPV control methods that allow to improve the system performance in the specific regions without the loss of general stability. These methods are a target of future investigation.

References

- Apkarian, P., Gahinet, P., and Becker, G. (1995), “Self-scheduled H_∞ control of linear parameter-varying systems: a design example,” *Automatica*, vol. 31, no. 9, pp. 1251–1261.
- Balas, G., Chiang, R., Packard, A., and Safonov, M. (2011), *Robust control toolbox. User’s guide.*, The MathWorks Inc., Natick, Massachusetts.
- Beckerle, P., Schaede, H., Butzek, N., and Rinderknecht, S. (2012a), “Balancing filters: An approach to improve model-based fault diagnosis based on parity equations,” *Mechanical Systems and Signal Processing*, vol. 29, pp. 137–147.
- Beckerle, P., Schaede, H., and Rinderknecht, S. (2012b), “Model-Based Fault Detection on Active Magnetic Bearings by Means of Online Transfer-Factor Estimation,” in *Proc. of 13th International Symposium on Magnetic Bearings*, Washington DC.
- Bendtsen, J.D., Stoustrup, J., and Tranbaek, K. (2005), “Bumpless transfer between observer-based gain scheduled controllers,” *International Journal of Control*, vol. 78, no. 7, pp. 491–504.
- Boyd, S.P. and Vandenberghe, L. (2004), *Convex Optimization*, Cambridge University Press.
- British Petroleum (2012), “BP Statistical Review of World Energy June 2012,” URL bp.com/statisticalreview.
- Chen, S.Y. and Lin, F.J. (2012), “Decentralized PID neural network control for five degree-of-freedom active magnetic bearing,” *Engineering Applications of Artificial Intelligence*.
- Cremer, L., Heckl, M., and Petersson, B. (2005), *Structure-Borne Sound*, Springer Berlin Heidelberg, Berlin, Heidelberg.
- Doyle, J.C. (1978), “Guaranteed margins for LQG regulators,” *Automatic Control, IEEE Transactions on*, vol. 23, no. 4, pp. 756–757.
- Ertas, B. and Vance, J. (2007), “The Influence of Same-Sign Cross-Coupled Stiffness on Rotordynamics,” *Journal of Vibration and Acoustics*, vol. 129, no. 1, p. 24.

- Fukata, S., Kouya, Y., Shimomachi, T., and Mizumachi, Y. (1991), “Dynamics of active magnetic thrust bearings,” *JSME international journal. Ser. 3, Vibration, control engineering, engineering for industry*, vol. 34, no. 3, pp. 404–410.
- Glover, K. and McFarlane, D. (1989), “Robust stabilization of normalized coprime factor plant descriptions with H_∞ -bounded uncertainty,” *Automatic Control, IEEE Transactions on*, vol. 34, no. 8, pp. 821–830.
- Green, M. (1995), *Linear robust control*, New York: Prentice Hall.
- Hanus, R., Kinnaert, M., and Henrotte, J.L. (1987), “Conditioning technique, a general anti-windup and bumpless transfer method,” *Automatica*, vol. 23, no. 6, pp. 729–739.
- Hynynen, K.M. (2011), *Broadband excitation in the system identification of active magnetic bearing rotor systems*, Ph.D. thesis, Lappeenranta University of Technology, URL <http://urn.fi/URN:ISBN:978-952-265-153-2>.
- Jastrzebski, R.P. (2007), *Design and implementation of FPGA-based LQ control of active magnetic bearings*, Ph.D. thesis, Lappeenranta University of Technology, URL <https://oa.doria.fi/handle/10024/32989>.
- Jastrzebski, R.P., Hynynen, K.M., and Smirnov, A. (2010), “H[infinity] control of active magnetic suspension,” *Mechanical Systems and Signal Processing*, vol. 24, no. 4, pp. 995–1006.
- Jastrzebski, R.P., Hynynen, K.M., Smirnov, A., and Pyrhonen, O. (2012a), “Influence of the drive and dc link generated disturbances on an AMB control system,” *Electrical Review*, vol. 2012, no. 1a, pp. 247–253.
- Jastrzebski, R.P., Smirnov, A., Hynynen, K., Nerg, J., Sopenan, J., Lindh, T., Heikkinen, J., and Pyrhonen, O. (2012b), “Commissioning and Control of the AMB Supported 3.5 kW Laboratory Gas Blower Prototype,” in *The 8th International Conference Mechatronic Systems and Materials MSM 2012*, Bialystok.
- Jeon, S., Ahn, H.J., and Han, D.C. (2002), “Model validation and controller design for vibration suppression of flexible rotor using AMB,” *KSME International Journal*, vol. 16, no. 2, pp. 1583—1593.
- Kjølhedde, K. and Santos, I.F. (2007), “Experimental Contribution to High-Precision Characterization of Magnetic Forces in Active Magnetic Bearings,” *Journal of Engineering for Gas Turbines and Power*, vol. 129, no. 2, p. 503.
- Knospe, C. (2006), “PID control,” *IEEE Control Systems Magazine*, vol. 26, no. 1, pp. 30–31.
- Knospe, C. and Zhu, L. (2011), “Performance Limitations of Non-Laminated Magnetic Suspension Systems,” *IEEE Transactions on Control Systems Technology*, vol. 19, no. 2, pp. 327–336.

- Kodochigov, N., Pobedonostsev, A., Ovchinnikov, V., and Drumov, I. (2012), “Development and Testing of the Code and Procedure for Balancing the Flexible Vertical Electromagnetically Suspended Rotor,” in *Proc. of 13th International Symposium on Magnetic Bearings*, Washington DC.
- Leith, D.J. and Leithead, W.E. (2000), “Survey of gain-scheduling analysis and design,” *International Journal of Control*, vol. 73, no. 11, pp. 1001–1025.
- Li, G. (2007), *Robust stabilization of rotor-active magnetic bearing systems*, Ph.D. thesis, University of Virginia.
- Li, G., Lin, Z., and Allaire, P.E. (2006), “Uncertainty Classification for Rotor-AMB Systems,” *Proc. of 10th International Symposium on Magnetic Bearings*.
- Limebeer, D.J.N., Kasenally, E.M., and Perkins, J.D. (1993), “On the design of robust two degree of freedom controllers,” *Automatica*, vol. 29, no. 1, pp. 157–168.
- Ljung, L. (1999), *System Identification: Theory for the User*, Prentice Hall, 2 edn.
- Ljung, L. (2011), *System identification toolbox. User’s guide*, The MathWorks Inc., Natick, Massachusetts.
- Lofberg, J. (2009), “Pre- and Post-Processing Sum-of-Squares Programs in Practice,” *IEEE Transactions on Automatic Control*, vol. 54, no. 5, pp. 1007–1011.
- Lösch, F. (2002), *Identification and Automated Controller Design for Active Magnetic Bearing Systems*, Ph.D. thesis, ETH Zurich, ETH Zurich.
- Lu, B., Choi, H., Buckner, G.D., and Tammi, K. (2008), “Linear parameter-varying techniques for control of a magnetic bearing system,” *Control Engineering Practice*, vol. 16, no. 10, pp. 1161–1172.
- Maslen, E.H., Cloud, H., Hauge, T., Tarald, S., and Arild, J. (2012), “Unbalance Response Assessment of a Subsea Compressor,” in *Proc. of 13th International Symposium on Magnetic Bearings*, Washington DC.
- Matsumura, F., Namerikawa, T., Hagiwara, K., and Fujita, M. (1996), “Application of gain scheduled H_∞ robust controllers to a magnetic bearing,” *Control Systems Technology, IEEE Transactions on*, vol. 4, no. 5, pp. 484–493.
- Mattingley, J., Wang, Y., and Boyd, S.P. (2011), “Receding Horizon Control,” *IEEE Control Systems*, vol. 31, no. 3, pp. 52–65.
- Mushi, S.E., Lin, Z., and Allaire, P.E. (2012), “Design, Construction, and Modeling of a Flexible Rotor Active Magnetic Bearing Test Rig,” *IEEE/ASME Transactions on Mechatronics*, vol. 17, no. 6, pp. 1170–1182.
- Mushi, S.E., Lin, Z., Allaire, P.E., and Evans, S. (2008), “Aerodynamic Cross-coupling in a Flexible Rotor : Control Design and Implementation,” in *The Eleventh International Symposium on Magnetic Bearings (ISMB 11)*, pp. 12–17.

- Oomen, T. and Bosgra, O. (2012), “System identification for achieving robust performance,” *Automatica*, vol. 48, no. 9, pp. 1975–1987.
- Orlov, Y., Belkoura, L., Richard, J., and Dambrine, M. (2002), “On identifiability of linear time-delay systems,” *IEEE Transactions on Automatic Control*, vol. 47, no. 8, pp. 1319–1324.
- Safonov, M.G. and Chiang, R.Y. (1988), “A Schur Method for Balanced Model Reduction,” in *American Control Conference, 1988*, pp. 1036–1040.
- Sawicki, J.T. and Maslen, E.H. (2008), “Toward Automated AMB Controller Tuning: Progress in Identification and Synthesis,” in *Proc. of 11th International Symposium on Magnetic Bearings*, pp. 68–74.
- Sawicki, J.T., Friswell, M.I., Kulesza, Z., Wroblewski, A., and Lekki, J.D. (2011), “Detecting cracked rotors using auxiliary harmonic excitation,” *Journal of Sound and Vibration*, vol. 330, no. 7, pp. 1365–1381.
- Schweitzer, G. and Maslen, E.H. (2009), *Magnetic Bearings*, Springer Berlin Heidelberg, Berlin, Heidelberg.
- Shi, L., Yu, S., Yang, G., Shi, Z., and Xu, Y. (2012), “Technical design and principle test of active magnetic bearings for the turbine compressor of HTR-10GT,” *Nuclear Engineering and Design*.
- Skogestad, S. and Postlethwaite, I. (2005), *Multivariable Feedback Control: Analysis and Design*, John Wiley & Sons.
- Smirnov, A. and Jastrzebski, R.P. (2009), “Differential evolution approach for tuning an H_∞ controller in AMB systems,” in *2009 35th Annual Conference of IEEE Industrial Electronics*, pp. 1514–1518, IEEE.
- Smirnov, A., Tolsa, K., and Jastrzebski, R.P. (2010), “Implementation of a bumpless switch in axial magnetic bearings,” in *2010 International Symposium on Industrial Embedded Systems (SIES)*, pp. 63–68.
- Spall, J.C. (2003), *Introduction to Stochastic Search and Optimization*, John Wiley & Sons, Inc., Hoboken, NJ, USA.
- Spall, J.C. (2010), “Factorial Design for Efficient Experimentation,” *IEEE Control Systems Magazine*, vol. 30, no. 5, pp. 38–53.
- Sun, Y., Ho, Y.S., and Yu, L. (2009), “Dynamic Stiffnesses of Active Magnetic Thrust Bearing Including Eddy-Current Effects,” *IEEE Transactions on Magnetics*, vol. 45, no. 1, pp. 139–149.
- Sun, Y. and Yu, L. (2002), “Analytical method for eddy current loss in laminated rotors with magnetic bearings,” *IEEE Transactions on Magnetics*, vol. 38, no. 2, pp. 1341–1347, URL <http://ieeexplore.ieee.org/lpdocs/epic03/wrapper.htm?arnumber=996021>.

- Swann, M. (2009), “Diffusion of magnetic bearings,” *Turbomachinery International*, vol. 50, no. 5, pp. 30—32.
- Turner, M.C. and Walker, D.J. (1999), “Modified linear quadratic bumpless transfer,” in *American Control Conference, 1999. Proceedings of the 1999*, vol. 4, pp. 2285–2289 vol.4.
- Turner, M.C. and Walker, D.J. (2000), “Linear quadratic bumpless transfer,” *Automatica*, vol. 36, no. 8, pp. 1089–1101.
- Walter, H., Denk, J., and Stoiber, D. (2010), “Active magnetic bearing systems with standard drive technology for large turbo machines,” in *2010 Record of Conference Papers Industry Applications Society 57th Annual Petroleum and Chemical Industry Conference (PCIC)*, pp. 1–8, IEEE.
- Zheng, K., Basar, T., and Bentsman, J. (2009), “ H_∞ Bumpless Transfer Under Controller Uncertainty,” *Automatic Control, IEEE Transactions on*, vol. 54, no. 7, pp. 1718–1723.
- Zheng, K., Lee, A.H., Bentsman, J., and Taft, C.W. (2006), “Steady-state bumpless transfer under controller uncertainty using the state/output feedback topology,” *Control Systems Technology, IEEE Transactions on*, vol. 14, no. 1, pp. 3–17.
- Zhou, K. and Doyle, J.C. (1998), *Essentials of Robust Control*, Prentice-Hall, Upper Saddle River, NJ.
- Zhu, L. and Knospe, C. (2010), “Modeling of Nonlaminated Electromagnetic Suspension Systems,” *IEEE/ASME Transactions on Mechatronics*, vol. 15, no. 1, pp. 59–69.

Appendices

Appendix A

Geometric center

Each radial bearing has three sensors that measure the distance from the sensor tip to the rotor surface. Two sensors are placed at 90° to each other, and the third sensor is placed between them. The angle between the third sensor and any other sensor is 135° . To estimate the center point of the rotor, it is necessary to find a circumscribed circle with the radius equal to the rotor surface radius for the triangle defined by these three measured points. Before coordinate transformation, the sensors should be shifted by the mean value. The mean value is obtained from the maximum and minimum possible deviation of the rotor surface from the sensor tip. An example of the procedure is presented in Table A.1.

Table A.1. Example of the coordinate transformation for a geometric center problem. The values are given in μm .

Comment	Sensor x	Sensor y	Sensor 3	x	y
1	400	702	1010	295.0	9.4
2	448	869	861	249.0	176.0
3	694	992	603	6.2	299.0
4	944	866	527	-234.0	166.0
5	995	651	642	-293.0	-49.2
6	894	463	845	-191.0	-235.0
7	679	395	1030	20.1	-298.0
8	520	462	1100	178.0	-232.0
max	995	992	1100		
min	400	395	527		
offset	698	694	812		

To make a polyhedron, each closest pair of the obtained boundary points is connected with a straight line. In two dimensions, the line in general is defined by three coefficients A , B , and C . The process of obtaining these coefficients is straightforward; an example

is presented in Table A.2.

Table A.2. Example of obtaining the coefficients for inequalities.

Point 1	Point 2	A	B	C
4	5	-215.0	53.2	-60200
5	6	-185.0	-102.0	-59300
6	7	-63.1	-211.0	-61600
7	8	66.1	-158.0	-48400
8	1	241.0	-117.0	-70000
1	2	166.0	45.9	-49600
2	3	123.0	243.0	-73400
3	4	-133.0	246.0	-72700

The center point for the example is found to be at $-10.1 \mu\text{m}$ along the x axis and $-11.8 \mu\text{m}$ along the y axis. The maximum radius of the safety region is computed to be $265 \mu\text{m}$.

The standard deviation calculated for the sensors with turned on power electronics is $4.5264 \mu\text{m}$. Thus sensor noise is relatively low and should not interfere with the above presented measurements.

Appendix B

Factorial design experiments

A factorial design of experiments can reduce the amount of necessary measurements by applying a specifically chosen input set. The set applies different signals to different inputs at the same time. An example of an input for a fractional factorial experiment is presented in Table B.1.

Table B.1. Example of the input matrix for the fractional factorial design with the order of 16.

Constant term β_0	Ax+ β_1	Ax- β_2	Ay+ β_3	Ay- β_4	Bx+ β_5	Bx- β_6	By+ β_7	By- β_8	z+ β_9	z- β_{10}
+1	-1	-1	-1	-1	+1	-1	-1	+1	-1	+1
+1	-1	-1	-1	+1	-1	+1	+1	-1	+1	-1
+1	-1	-1	+1	-1	-1	+1	+1	-1	-1	+1
+1	-1	-1	+1	+1	+1	+1	+1	+1	+1	-1
+1	-1	+1	-1	-1	-1	-1	+1	-1	-1	-1
+1	-1	+1	-1	+1	+1	+1	+1	-1	+1	+1
+1	-1	+1	+1	+1	-1	-1	+1	+1	+1	+1
+1	+1	-1	-1	-1	-1	+1	-1	-1	-1	-1
+1	+1	-1	-1	+1	+1	+1	-1	-1	+1	+1
+1	+1	-1	+1	-1	+1	+1	-1	-1	+1	+1
+1	+1	-1	+1	+1	-1	-1	+1	+1	-1	-1
+1	+1	+1	-1	-1	+1	+1	+1	+1	-1	-1
+1	+1	+1	-1	+1	-1	-1	-1	-1	+1	+1
+1	+1	+1	+1	-1	-1	-1	-1	-1	-1	-1
+1	+1	+1	+1	+1	+1	+1	+1	+1	+1	+1

Using the knowledge about the AMB system structure and physics, it is possible to reduce the number of experiments and improve the reliability of the results at the

same time. The obtained measurements are demonstrated in Tables B.2 and B.3.

Table B.2. Results obtained by an iteration experiment of the order of 55.

Inputs	Outputs				
	Ax	Ay	Bx	By	z
Constant	0.146	-0.0333	0.567	-0.0965	-2.37
Ax+	4.08	0.689	2.58	2.2	-1.31
Ax-	-5.53	0.915	-2.18	-1.97	-0.98
Ay+	0.246	3.24	-0.593	0.89	-0.0588
Ay-	-0.829	-2.96	1.03	-1.66	-1.3
Bx+	1.97	-1.73	3.49	2.83	-1.33
Bx-	-3.05	2.43	-6.69	0.386	-0.124
By+	1.92	2.77	-0.791	8.83	0.021
By-	-2.19	-2.34	-1.35	-4.68	-1.05
z+	0.00329	0.00657	-0.141	0.118	3.8
z-	0.103	-0.155	-0.137	-0.532	-1.7

Table B.3. Results obtained by an iteration experiment of the order of 175.

Inputs	Outputs				
	Ax	Ay	Bx	By	z
Constant	2.09	-0.92	3.56	-0.81	-8.61
Ax+	10.9	1.75	5.0	3.95	-1.22
Ax-	-12.1	0.714	-4.33	-2.68	-0.609
Ay+	0.876	6.7	-1.61	2.88	-1.24
Ay-	-1.55	-7.68	2.7	-3.36	-2.56
Bx+	5.66	-4.1	9.43	4.31	-2.69
Bx-	-4.72	3.92	-10.78	0.0922	-0.133
By+	4.23	5.74	-1.26	15.6	0.449
By-	-4.96	-4.05	-2.28	-9.18	-1.55
z+	-0.135	-0.396	-0.0529	-0.173	4.59
z-	0.4	-0.224	-0.1527	-0.881	-3.29

First, the measurements presented above are obtained and statistically updated. Next, the following algorithm is used to find a unique correspondence between the inputs and outputs. The special algorithm is necessary as one output has two main input contributors that act in opposite directions.

Listing B.1: Pseudo code for assigning the inputs to the outputs.

```
Phi // a matrix obtained after analysis
while( (not all inputs are assigned)
       or (maximum number of iterations is reached))
{
  // find absolute maximum elements in each row
  row_max = max_rows(Phi);
  // find absolute maximum elements in each column
  col_max = max_cols(Phi);

  for i in (row_max){
    for j in col_max(){
      // Absolute position in the matrix is compared
      // not the values
      if row_max(i)=col_max(j){
        element = Phi(row_max(i));
        assign input i to output j
        remove row i
        if element>0
          put all positive values in column i to 0
        else
          put all negative values in column i to 0
      }
    }
  }
}
```

Appendix C

Identification

Some additional results that are not included in Chapter 4 are presented here. The general outline for the identification procedure is given in Listing C.1.

The second rotor is identified with the same procedure as the first one. The results of the rotor parametric identification are combined in Table C.1.

Table C.1. Results of the parametric identification for the second rotor.

Parameter	Initial value	Identified value	Standard deviation
Current stiffness A-end, [A m ⁻¹]	21.863	18.532	0.27317
Position stiffness A-end, [N m ⁻¹]	110310	92512	52.463
Current stiffness B-end, [A m ⁻¹]	21.863	20.321	0.45452
Position stiffness B-end, [N m ⁻¹]	110310	102115	3006.2
Flexible mode frequency, [rad s ⁻¹]	15293	15211	519.61
Flexible mode damping ratio	2000e-6	3720.5e-6	13.145e-6
Polar moment of inertia, [kg m ²]	723.58e-6	863.88e-6	31.049e-6

The main interest is in identifying the rotor with an impeller as this case is closer to the operation conditions. The numerical results are presented in Table C.2. The difference between the initial model and the fitted model can be seen in Fig. C.1. The

Listing C.1: Pseudo code for the identification procedure.

```

// Initialize actuator model
ActuatorModel = init();
// Obtain measurement data for the actuator.
// Output to input current relations.
ActuatorData = load();
// Identify bandwidth of the actuator
Wbw = pem(ActuatorModel, ActuatorData);

// Initialize the AMB-rotor model with the identified
// bandwidth of an actuator and zero speed value (speed=0)
speed = 0;
AMBModel = init(Wbw, speed);
// Obtain measurement data for the AMB-rotor system at standstill
AMBDataAtZeroSpeed = load();
// Identify current and position stiffness
// for A and B radial bearings (kiA, kxA, kiB, kxB)
[kiA, kxA, kiB, kxB] = pem(AMBModel, AMBDataAtZeroSpeed);

// Initialize the AMB-rotor model with the identified
// bandwidth of an actuator, stiffness
// and zero speed value (speed=0)
AMBModel = init(Wbw, speed, kiA, kxA, kiB, kxB);
// Based on the FEM data get lower and upper boundaries for
// the frequency of the first flexible mode (fl, fu)
fl = load();
fu = load();
// Identify the damping ratio (sigm1) and the
// frequency (f1) of the first flexible mode
// in the desired frequency region
[sigm1, f1] = pem(AMBModel, AMBDataAtZeroSpeed(fl, fu));

// Initialize the AMB-rotor model with the identified
// bandwidth of an actuator, stiffness,
// parameters of the first flexible mode and nominal
// speed value (speed!=0)
speed = 45000;
AMBModel = init(Wbw, speed, kiA, kxA, kiB, kxB, sigm1, f1);
// Obtain measurement data for the AMB-rotor system
// at nominal speed
AMBDataAtNominalSpeed = load();
// Identify the polar moment of inertia (Ip) at nominal speed
Ip = pem(AMBModel, AMBDataAtNominalSpeed);

// Initialize the AMB-rotor model with the
// identified bandwidth of an actuator, stiffness,
// parameters of the first flexible mode, polar
// moment of inertia and nominal speed value (speed!=0)
AMBModel = init(Wbw, speed, kiA, kxA, kiB, kxB, sigm1, f1, Ip);
// Identify the gyroscopi effect of the first
// flexible mode (Ifl) at nominal speed
Ifl = pem(AMBModel, AMBDataAtNominalSpeed);

// Initialize the AMB-rotor model with the identified values
AMBModel = init(Wbw, speed, kiA, kxA, kiB, kxB, sigm1, f1, Ip, Ifl);

// Return the identified model
return AMBModel;

```

accuracy value is calculated according to the following equation

$$\eta = 1 - \frac{\|Y - \hat{Y}\|_2}{\|Y - \bar{Y}\|_2}, \quad (\text{C.1})$$

where Y is the measured signal, \bar{Y} is the mean value, and \hat{Y} is the data from the estimated model. The value in percent is obtained by multiplying η by 100. In

Table C.2. Results of the parametric identification for the second rotor with an impeller.

Parameter	Initial value	Identified value	Standard deviation
Current stiffness A-end, [A m ⁻¹]	21.863	15.503	0.8075
Position stiffness A-end, [N m ⁻¹]	110310	81003	5751.9
Current stiffness B-end, [A m ⁻¹]	21.863	19.645	0.99466
Position stiffness B-end, [N m ⁻¹]	110310	102788	5751.9
Flexible mode frequency, [rad s ⁻¹]	8067.6	7792.9	550.71
Flexible mode damping ratio	2000e-6	14793e-6	150.06e-6
Polar moment of inertia, [kg m ²]	849.49e-6	1346.9e-6	66.126e-6
Modal inertia of a flexible mode	0.10938	0.24161	0.0017447
Parameters tuned for the operating point			
Flexible mode damping ratio	14793e-6	5221.4e-6	10.257e-6
Flexible mode frequency, [rad s ⁻¹]	7792.9	7915.1	267.33

Fig. C.1 it is seen how the fitted value is compromised between different directions. Thus, the final model in the y plane in the y plane direction has a slightly smaller fit value but the x plane in the x direction has a significant improvement. Almost the same behavior is demonstrated in the case of the x plane in the y direction and the y plane in the x direction.

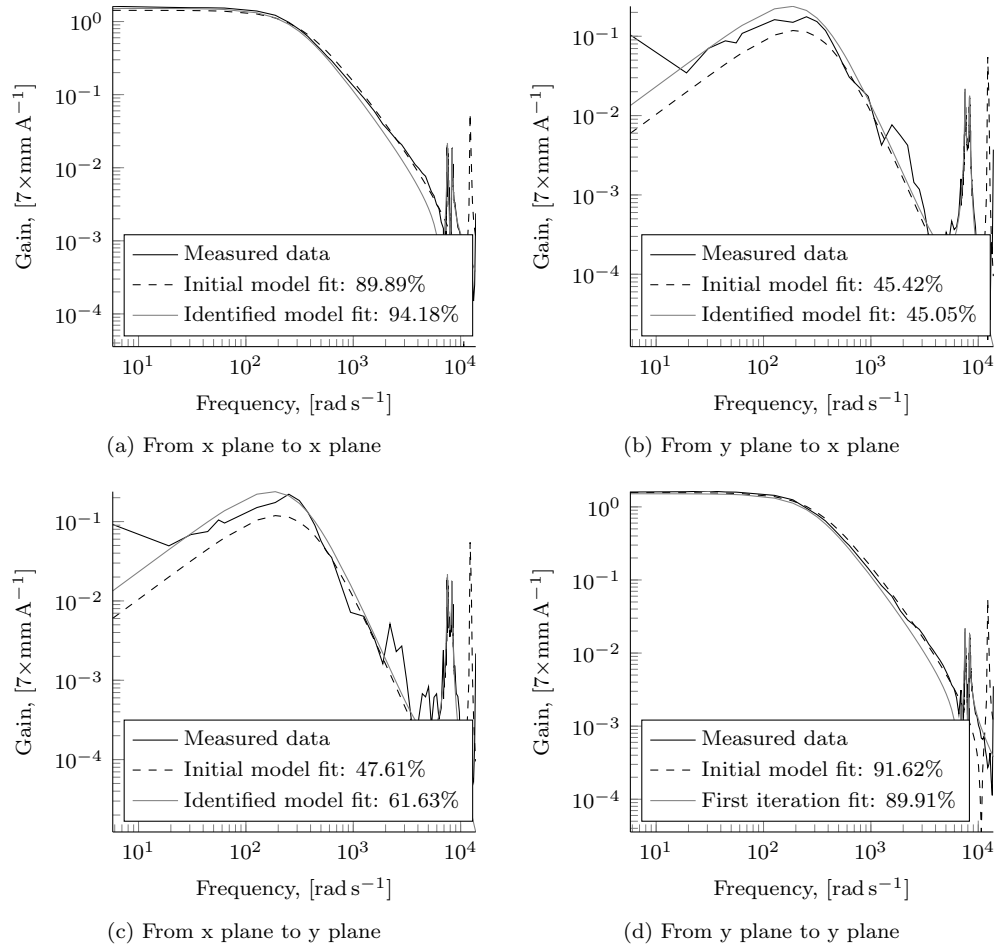


Figure C.1. Identification of the model parameters for the second rotor with an impeller at 22000 rpm, A-end. The initial model is based on the analytical expressions. A set of parameters is fitted to the measured data with the algorithm described above. The case for the rotating system is presented when there is a gyroscopic coupling between the planes of one end.

Appendix D

Details of the prototype platform

D.1 Magnetic bearing dimensions

The magnetic bearings are defined by a set of geometrical and mechanical parameters. For radial bearings they are presented in Table D.1 and for axial bearings in Table D.2, respectively. Additional explanations about the geometrical dimensions are given in Fig. D.1 and Fig. D.2.

Table D.1. Parameters and dimensions of radial bearings.

Name	Symbol	Value
Stator diameter	$\varnothing_{s,o}$	101 mm
Core length	l_{core}	20.5 mm
Width of the stator teeth	d_{st}	8 mm
Slot to slot diameter	$\varnothing_{s,i}$	40 mm
Shaft diameter	\varnothing_r	39 mm
Lamination sheet thickness		0.1 mm
Mechanical air gap	g_a	250 μm
Magnetic air gap	g_0	500 μm
Turns per magnet	N	108
Resistance	R	0.3 Ω
Inductance	L	3.63 mH
DC link voltage	U_{DC}	60 V
Maximum current	i_{max}	6 A
Bias current	i_b	2.5 A

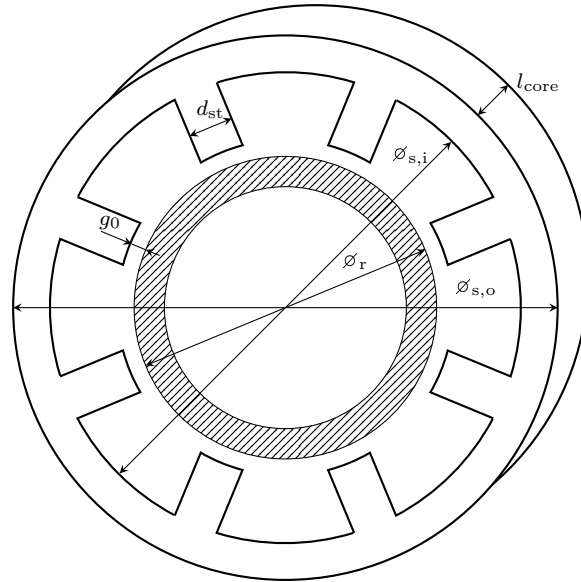


Figure D.1. Geometry of the radial magnetic bearing.

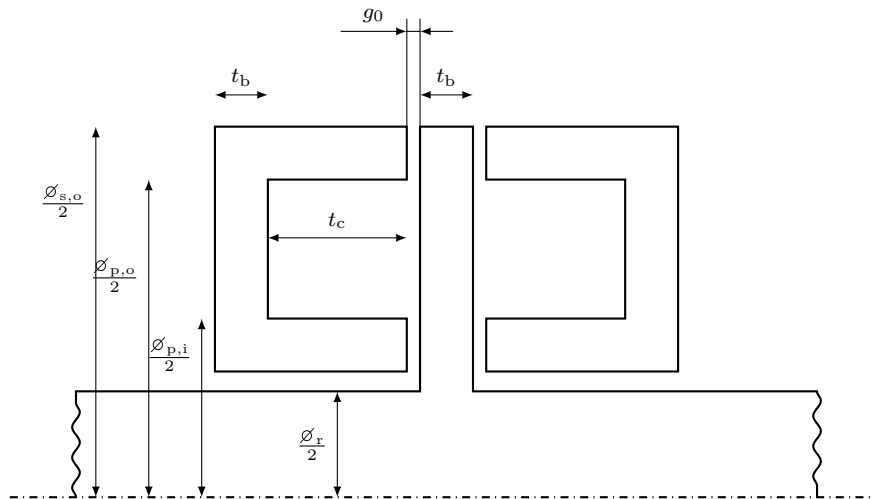


Figure D.2. Geometry of the axial magnetic bearing.

Table D.2. Parameters and dimensions of axial bearings.

Name	Symbol	Value
Outer diameter	$\varnothing_{s,o}$	96 mm
Outer pole diameter	$\varnothing_{p,o}$	88 mm
Inner diameter	$\varnothing_{s,i}$	59 mm
Inner pole diameter	$\varnothing_{p,i}$	67 mm
Axial disk thickness	t_b	4 mm
Coil depth	t_c	10.5 mm
Mechanical air gap	g_a	250 μm
Magnetic air gap	g_0	500 μm
Turns per magnet	N	54
Resistance	R	0.214 Ω
Inductance	L	497 μH
DC link voltage	U_{DC}	60 V
Maximum current	i_{max}	6 A
Bias current	i_b	2.5 A

D.2 Parameters of the rotor

The rotors in the system are described according to the scheme presented in Fig. 2.8. The distances from the center of mass to the specific locations with other parameters are listed in Table D.3. All the mentioned values are obtained at the initial stage of the modeling with the FEM.

Table D.3. Modeled parameters of the rotors.

	Rotor 1	Rotor 1 with impeller	Rotor 2	Rotor 2 with impeller
Radial bearing A location, d_A [mm]	87.281	97.663	87.872	98.825
Radial bearing B location, d_B [mm]	64.219	53.837	77.128	66.175
Radial sensor A location, $d_{s,A}$ [mm]	112.78	123.16	112.78	123.16
Radial sensor B location, $d_{s,B}$ [mm]	86.219	75.837	86.219	75.837
Total mass, kg	2.621	2.799	2.506	2.684
Transversal moment of inertia, [g m ²]	10.75	15.27	11.494	16.111
Polar moment of inertia, [mg m ²]	994.4	1120.3	723.57	849.49

D.3 Sensors and control electronics

For the estimation of the rotor position, seven similar single-ended eddy-current sensors are used. One sensor is mounted in the axial direction, and there are three sensors for each radial bearing.

Table D.4. Parameters of the single-ended CMSS 65.

Name	Value
Measuring range	0.2 mm to 2.3 mm
Sensitivity	7.87 mV μm^{-1}
Output range from driver	0 V to -18 V
Linearity	25.4 μm
Frequency bandwidth (-3 dB)	10 kHz

The current in the system is controlled by custom-made electronics. The switching signals for IGBTs are provided by a Xilinx Virtex-II Pro field programmable gate array (FPGA). The reference values for currents are obtained through a custom-built Spartan-II board that works as an interface between dSpace and Virtex-II. To implement feedback for the current control, ten LEM sensors described in Table D.5 are used. They provide signal for the dSpace ADC boards with parameters listed in Table D.6.

Table D.5. Parameters of the LEM current sensor.

Name	Value
Measuring range	0 A to 36 A
Accuracy at $i_{PN} = 25$ A	0.5 %
Output range	0 V to 3.75 V
Linearity	0.2 %
Response time	1 μs
Frequency bandwidth (-1 dB)	150 kHz

Table D.6. Parameters of DS2001 ADC boards connected to the dSpace.

Name	Value
Number of ADC channels per board	5
Resolution	16 bit
Conversion time	5 μs
Input range	-5 V to 5 V or -10 V to 10 V
Organisation of inputs	parallel

Appendix E

Control system models

The scaled model of the rigid rotor system is described by the following state-space equations

$$\mathbf{A} = \begin{bmatrix} -6377 & 0 & 0 & 0 & 0 & 0 & 0 & 0 & 0 & 0 & 0 & 0 \\ 0 & -6377 & 0 & 0 & 0 & 0 & 0 & 0 & 0 & 0 & 0 & 0 \\ 0 & 0 & -6377 & 0 & 0 & 0 & 0 & 0 & 0 & 0 & 0 & 0 \\ 0 & 0 & 0 & -6377 & 0 & 0 & 0 & 0 & 0 & 0 & 0 & 0 \\ 0 & 0 & 0 & 0 & 0 & 0 & 0 & 0 & 121 & 0 & 0 & 0 \\ 0 & 0 & 0 & 0 & 0 & 0 & 0 & 0 & 0 & 121 & 0 & 0 \\ 0 & 0 & 0 & 0 & 0 & 0 & 0 & 0 & 0 & 0 & 121 & 0 \\ 0 & 0 & 0 & 0 & 0 & 0 & 0 & 0 & 0 & 0 & 0 & 121 \\ 333 & 0 & 422 & 0 & 568 & 0 & 0 & -3.72 & 0 & 0 & 0 & 0 \\ 0 & 333 & 0 & 422 & 0 & 568 & 3.72 & 0 & 0 & 0 & 0 & 0 \\ 0 & 5499 & 0 & -4666 & 0 & 620 & 639 & 0 & 0 & 0 & 0 & -197 \\ -5499 & 0 & 4666 & 0 & -620 & 0 & 0 & 639 & 0 & 0 & 197 & 0 \end{bmatrix}, \quad (\text{E.1})$$

$$\mathbf{B} = \begin{bmatrix} 6377 & 0 & 0 & 0 \\ 0 & 6377 & 0 & 0 \\ 0 & 0 & 6377 & 0 \\ 0 & 0 & 0 & 6377 \\ 0 & 0 & 0 & 0 \\ 0 & 0 & 0 & 0 \\ 0 & 0 & 0 & 0 \\ 0 & 0 & 0 & 0 \\ 0 & 0 & 0 & 0 \\ 0 & 0 & 0 & 0 \\ 0 & 0 & 0 & 0 \\ 0 & 0 & 0 & 0 \end{bmatrix}, \quad (\text{E.2})$$

$$\mathbf{C} = \begin{bmatrix} 0 & 0 & 0 & 0 & 1 & 0 & 0 & -0.121 & 0 & 0 & 0 & 0 \\ 0 & 0 & 0 & 0 & 0 & 1 & 0.121 & 0 & 0 & 0 & 0 & 0 \\ 0 & 0 & 0 & 0 & 1 & 0 & 0 & 0.0887 & 0 & 0 & 0 & 0 \\ 0 & 0 & 0 & 0 & 0 & 1 & -0.0887 & 0 & 0 & 0 & 0 & 0 \end{bmatrix} \quad \mathbf{D} = \mathbf{0}_{4 \times 4}. \quad (\text{E.3})$$

The model also includes a first-order description of an actuator for each input. The actual model used for the controller synthesis is supplemented with a first-order time delay approximation. That delay is added to each input and the presented model can be easily extended to the one including the delay.

The transfer functions for the selected number of controllers used are presented in Fig. E.1. The Glover–McFarlane controller is a two-degrees-of-freedom controller, and for comparison, only its feedback part is presented. The LPV controller is demonstrated for the mid-point that corresponds to 22 500 rpm.

The systems presented in physical values and described in the linear state-space form tend to have a high condition number. The condition number for the linear system \mathbf{G} is defined as

$$\gamma_{\text{cn}}(\mathbf{G}) = \bar{\sigma}(\mathbf{G})/\underline{\sigma}(\mathbf{G}), \quad (\text{E.4})$$

which is the relation between the maximum singular value $\bar{\sigma}$ and the minimum singular value $\underline{\sigma}$. The high condition number leads to numerical problems. The solution of LMIs may be sensitive to these. Other numerical problems appear during the implementation of the hardware used. For efficient use in controllers, a single precision or a fixed point description is used. Thus, an overflow or an integration error may occur.

To avoid the above-mentioned problem, the systems are usually scaled. The inputs and outputs are scaled by the maximum number for inputs or outputs, respectively, and the states are scaled by the maximum value of the state. The maximum value for inputs is the maximum control current (i_c), while for the outputs it is the maximum displacement of the rotor, which is assumed to be equal to the magnetic air gap g_0 . The first four states of the system (E.1) describe the dynamics of the actuator and are also limited by the maximum i_c . The next four states in matrix \mathbf{A} are displacements and are limited by g_0 . The last four elements describe the rotor speeds along the respective axis. The maximum value for the speed is obtained as follows

$$V_{\text{max}} = \sqrt{\frac{2f_{\text{max}}g_0}{m}}, \quad (\text{E.5})$$

where f_{max} is the maximum force provided by a pair of electromagnets.

The scaling matrices have the following form

$$\mathbf{T}_u = \frac{1}{i_{c,\text{max}}} \mathbf{I}_{4 \times 4}, \quad \mathbf{T}_y = \frac{1}{g_0} \mathbf{I}_{4 \times 4}, \quad (\text{E.6})$$

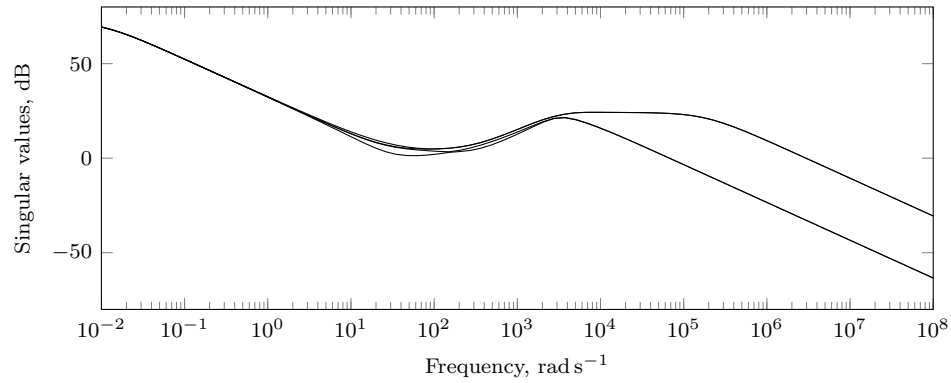
$$\mathbf{T} = \begin{bmatrix} \frac{1}{i_{c,\text{max}}} \mathbf{I}_{4 \times 4} & & \\ & \frac{1}{g_0} \mathbf{I}_{4 \times 4} & \\ & & \frac{1}{V_{\text{max}}} \mathbf{I}_{4 \times 4} \end{bmatrix}, \quad (\text{E.7})$$

where \mathbf{T}_u is the input scaling matrix, \mathbf{T}_y is the output scaling matrix, and \mathbf{T} is the state scaling matrix. Finally, the scaled system is obtained as follows

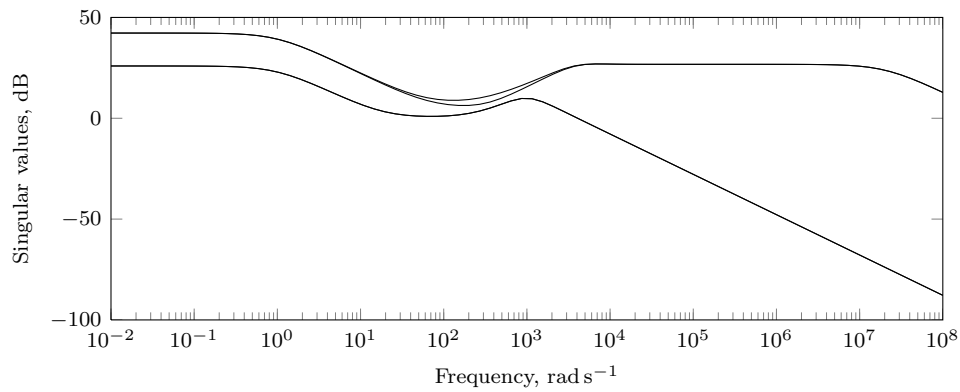
$$\mathbf{A}_{\text{scaled}} = \mathbf{TAT}^{-1}, \quad \mathbf{B}_{\text{scaled}} = \mathbf{TB}\mathbf{T}_u^{-1}, \quad (\text{E.8})$$

$$\mathbf{C}_{\text{scaled}} = \mathbf{T}_y\mathbf{CT}^{-1}, \quad \mathbf{D}_{\text{scaled}} = \mathbf{T}_y\mathbf{D}\mathbf{T}_u^{-1}. \quad (\text{E.9})$$

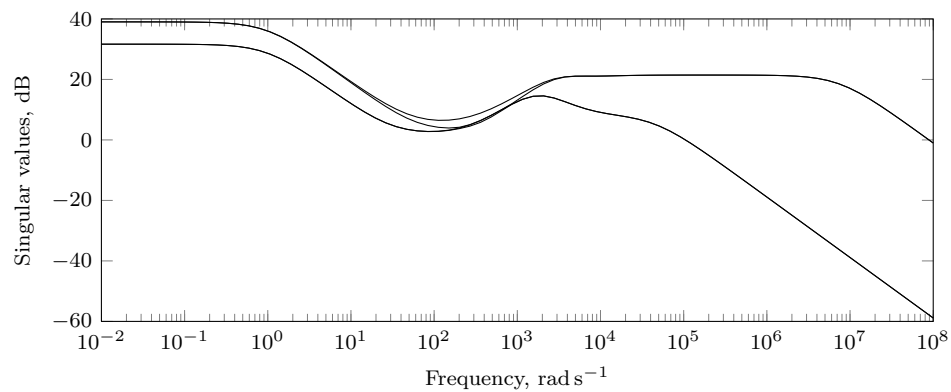
With such scaling the condition number was reduced from 2.55×10^5 to 101.



(a) Glover-McFarlane controller



(b) Robust controller



(c) LPV controller

Figure E.1. Singular values of transfer functions for different controllers. For all cases, only the feedback part is presented. For the LPV controller, its value at 22500 rpm is demonstrated. All controller functions are synthesized for the scaled system.

